2019

On the Interactions of Augmin with Microtubules and the Mechanics of the Cross-Linker PRC1

Alejandro Dottore

ON THE INTERACTIONS OF AUGMIN WITH MICROTUBULES AND THE MECHANICS OF THE CROSS-LINKER PRC1

A Thesis Presented to the Faculty of

The Rockefeller University

in Partial Fulfillment of the Requirements for

the degree of Doctor of Philosophy

by

Alejandro Dottore

June 2019

ON THE INTERACTIONS OF AUGMIN WITH MICROTUBULES AND THE MECHANICS OF THE CROSS-LINKER PRC1

Alejandro Dottore, Ph.D.

The Rockefeller University 2019

Cell division in eukaryotes requires the assembly and maintenance of a structure, the bipolar spindle, self-organized from microtubules and their associated proteins. A multitude of components have been identified to be involved in this organization, and solving the combinatorial of the conditions that lead to the specific set of configurations present in vivo remains an open question. This thesis presents reconstitutions from purified components used to study aspects of microtubule self-organization: first, the microtubule-nucleation-related augmin octameric complex was assessed at a single-molecule interaction level with microtubules; second, the cross-linker PRC1's frictional response resisting motion between two microtubule filaments was analyzed to determine the dependence of the frictional force on the binding conditions of the cross-linker. For the augmin complexes studied sub-second interaction times were observed, yielding diffusive tracks on the lattice of microtubules. Microtubule bundles driven to slide showed GFP-PRC1 accumulation with a near-contant frictional force recorded. From the data, a theoretical model was produced linking the accumulation of GFP-PRC1 to the time evolution of the force trace. The observations on the reconstituted augmin complex establish constrains (diffusive and short lived) on an entity proposed to anchor newly-nucleated microtubules to

pre-existing microtubules at a given branching angle. The observations on PRC1 mechanics lead to the hypothesis of a changing mechanical behavior of the cross-linker to its exchange kinetics, potentially modulated by external factors.

Acknowledgments

This thesis took about one thousand days to be completed. It would not have been possible to reach this state without the support, and patience, of my mentor Tarun Kapoor, the Dean's Office of the Rockefeller University, and the director of the Tri-Institutional PhD Program in Chemical Biology, Derek Tan. During my time engaged in research, members of the Kapoor lab were instrumental in my progress, most notably: Scott Forth, an outstanding physicist with a very elastic toolkit capable of finding fitting solutions to the most outlandish problems, Radhika Subramanian, a temperate and kind soul gifted with the deepest reflections, Kuo-Chiang Hsia, a hard-working and spiritually unwavering beacon of peace, and Yuta Shimamoto, the wisest and most thoughtful individual I encountered in my studies. I am very thankful for the comments and suggestions of Victoria Andino Pavlovsky during the writing process, as they were fundamental to the finalization of this document.

I also want to thank my committee, Seth Darst, Anant Menon, and Sandy Simon for providing their time and expertise. And finally, and most importantly, I would like to thank my friends, north and south, my sister, my dad, and my mom for their love and encouragement.

Table of Contents

Acknowledgements iii

Table of Contents iv

List of Figures vii

Chapter 1. Introduction 1

1.1 Cell division eukaryotes: the mitotic apparatus 1

1.2 Microtubules and associated proteins 5

1.3 The metaphase spindle 10

1.4 The anaphase spindle 16

2. Materials and methods 20

2.1 GFP-PRC1 purification 20

2.2 Microtubule polymerization and labeling 21

2.3 Microscope glass treatment 23

2.4 Rigor kinesin purification 24

2.5 Bead coating 25

2.6 TIRF microscopy 26

2.7 Single spot tracking and intensity data acquisition and analysis 27

2.8 Optical trapping and force measurements 30

2.9 Microtubule bundle manipulation assays 33

2.10 Bundle manipulation data analyses 36

2.11 Stochastic simulations 38

3. Single-molecule TIRF characterization of augmin 39

3.1 Background information 39

3.2 Biochemical reconstitution of GFP-tagged augmin holo-complex and sub-complexes 43
3.3 Single spot intensity analyses of augmin holo-complex and sub-complexes 48
3.4 The augmin holo-complex and sub-complexes diffuse when bound to the microtubule lattice, and all but a dimeric sub-complex have a bimodal interaction time distribution 51
3.5 Conclusion 57
4. GFP-PRC1 cross-linking mechanics 59
4.1 Background information 59
4.2 Characterization of the GFP-PRC1 construct used 64
4.3 GFP-PRC1 gets enriched to microtubule bundles with a preference to an antiparallel alignment of microtubules 68
4.4 GFP-PRC1 binds to bundles with a given microtubule alignment but not the inverse, and it exchanges at a rate of hundreds of seconds 72
4.5 Driven sliding of bundles at constant velocity shows GFP-PRC1 accumulation 79
4.6 The frictional force recorded did not scale with the bundle length, but scaled with the GFP-PRC1 signal intensity 86
4.7 Stochastic simulations based on a combination of established models reproduce the lack of scaling between force and length observed experimentally 90

4.8 Raising salt and GFP-PRC1 concentrations leads to a shorter characteristic exchange time and a lower frictional force slope during driven sliding 100
4.9 Conclusion 105
5. Future directions 107
5.1 Expanding the reconstitution to a functional augmin complex 107
5.2 Understanding the distribution of interaction times 108
5.3 Contribution of other variables on bundle mechanics 110
5.4 Inclusion of additional components towards the reconstitution of the spindle midzone 111
5.5 Establishing the properties of PRC1 that determine bundle mechanics 112
5.6 Model expectations on dividing cells 113
References 114

List of Figures

1.1 Visualizing cell division in Eukarya 3

1.2 Microtubule polymerization dynamics, nucleation, and network self-organization by MAPs 8

1.3 Metaphase spindle's microtubule nucleation, dynamics, and mechanics 14

1.4 Spindle changes during anaphase A and B 18

3.1 The augmin complex and its putative function 42

3.2 Biochemistry of augmin sub-complexes and the holo-complex 46

3.3 GFP-tagged augmin complexes stuck to a glass surface and observed through TIRF microscopy 49

3.4.1 Single-molecule microscopy of microtubule-bound dimeric and tetrameric augmin sub-complexes 53

3.4.2 Single-molecule microscopy of microtubule-bound augmin octamer and holo-complex 55

4.1 PRC1 is a diffusible cross-linker of microtubules 62

4.2 GFP-PRC1 forms a dimer that diffuses on microtubules 66

4.3 Visualizing microtubule bundles cross-linked by GFP-PRC1 70

4.4 Manipulation of microtubules with optical tweezers, to change bundle orientation 76

4.5 GFP-PRC1's evolution in bundles driven to slide at a constant velocity 83

4.6 The recorded frictional force did not scale with bundle length during driven sliding, but scaled with the number of GFP-PRC1 molecules in the bundle and exhibiting viscosity 88

4.7 Stochastic simulations of bundles during driven sliding 98

4.8 Raising salt and GFP-PRC1 concentrations lead to a faster recovery on re-assembly, a lower GFP signal accumulation and a lower frictional force slope during driven sliding 103

1. Introduction

1.1 Cell division in eukaryotes: the mitotic apparatus

When it became evident that most living organisms where made of cells, and cells came from the division of other cells, it began the effort to elucidate the mechanisms of cell division. The first observations and first modeling of the process began in the “first golden age of cytology”, starting with the discovery of the nucleus in 1833 (Gourret, 1995; McIntosh and Hays, 2016). How the nucleus divided into two became more clear with observations in the 1870s, which introduced new concepts such as ‘asters’, ‘spindles’, and ‘chromosomes’ (Figure 1.1 A and B). The models proposed back then were typically based on the theoretical developments of physics from that time, with thermodynamics (diffusion and surface tension), and electromagnetism being common mechanistic bases. None of the models from the late XIX and early XX centuries survived to date, as the “second golden age of cytology”, which came with the use of transmission electron microscopy in biology, placed the focus on microtubules and their biology to produce models, leading to our current understanding of cell division. Only some nomenclature survives from before 1950.

Cell division of non-germ-line cells takes place in phases (Strasburger, 1884): prophase, when chromatin condenses to chromosomes (in plants there is a preprophase when the nucleus migrates to the site where the cell is to divide, and a band forms in that plane); metaphase, when the chromosomes congress to an equatorial plane of the spindle referred as metaphase plate; anaphase, when sister chromatids are segregated to separate positions and the cell elongates;

and telophase, when the nucleus reforms and chromatin de-condenses. Cellular abscission can occur following telophase, with a cleavage furrow ingressing where the metaphase plate was located.

Some features of mitosis are conserved among eukaryotes, such as the presence of microtubules made of conserved tubulin proteins. A multitude of model organisms have been used to solve fundamental questions about mitosis (Yanagida, 2014), including budding and fission yeast, fly embryos, frog oocytes, and mammalian cells. Yeast, diatoms, and dinoflagellates carry mitosis without dismantling the nuclear envelope (closed mitosis). In yeast the poles of the spindle are embedded on the nuclear membrane, as spindle pole bodies (Figure 1.1 B and C). Moreover, the easiness of genetic studies in yeast has allowed the identification of the regulators of the cell cycle, and progression in mitosis, which were later found to be conserved across Eukarya (Nurse, 1990). Another model organism that has been used is *Xenopus laevis*; particularly, the cell-free oocyte extract has allowed the depletion and addition of factors in a media that can assemble acentrosomal meiotic spindles arrested in metaphase II (Figure 1.1 E). A variety of human cell lines are also available for the study of cell division (Figure 1.1 F).

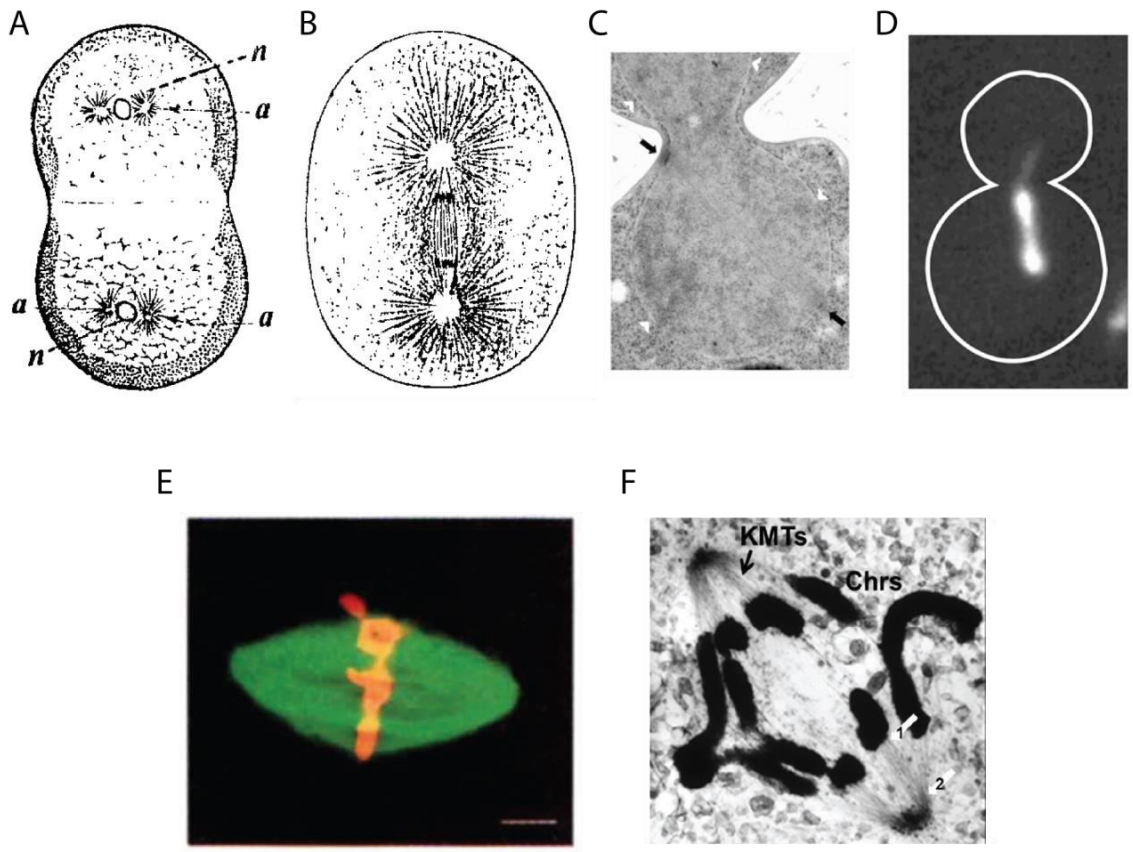

Figure 1.1 Visualizing cell division in Eukarya. **(A)** Drawings of eggs of the medusa *Geryonis* dividing for a second time. The structures around the nucleus (n) were named 'asters' (a) by Fol. (Illustration from Fol, 1873). **(B)** Drawings reproduced from observations of the first division of an *Unio* egg. The two dark bodies between asters were eventually named 'chromosomes'. The structure between the asters is called the 'spindle'. (Illustration from Strasburger, 1875). **(C)** Electron microscopy image of a *Saccharomyces cerevisiae* yeast dividing. White arrowheads mark the nuclear envelope, and black arrows mark the spindle pole bodies. **(D)** Fluorescence imaging of a yeast mitotic spindle of a cell expressing GFP-tagged α-tubulin. The white outline illustrates the cell surface. (C and D were adapted from Winey and Bloom, 2012). **(E)** A spindle assembles

around sperm DNA in *Xenoupus laevis* egg extracts. Fluorescein-labeled tubulin is shown in *green*, and DNA was stained with propidium iodide (in red). (Adapted from Heald et al, 1996). **(F)** Thick section of a mammalian (HeLa) cell in anaphase imaged by electron microscopy. Chromosomes (Chrs), and kinetochore microtubule fibers (KMT), are indicated. The white arrows indicate sites where microtubule-kinetochore (1), and microtubule-pole attachments would occur. (Adapted from McIntosh et al, 1975).

1.2 Microtubules and associated proteins

Microtubules were first identified as cytoplasmic structures (Slautterback, 1963), and were found to be abundant in mitotic spindles (Figure 1.2 A). The α,β-tubulin heterodimer was identified and purified by colchicine binding (Borisy and Taylor, 1967a and 1967b), as the constituent of microtubules. Tubulins are GTPases, and can be classified into types: α, β, γ, δ, ε, and η; with δ, ε, and η being associated to centrioles, and α, β, and γ having multiple subtypes (Ludueña, 2013). For α,β-tubulin heterodimer in solution, α-tubulin does not exchange GTP, but β-tubulin does (Arai et al, 1975). The subtype diversity together with post-translational modifications (acetylation, phosphorylation, polyamination, polyglutamylation, polyglycylation, detyrosination, and C-terminal deglutamylation), on tubulin are proposed to give rise to a 'tubulin code' (Janke, 2014).

Microtubules are filaments with an external diameter of 25 nm, with proteins arranged cylindrically with a hollow interior. α,β-tubulin heterodimers constitute the subunit that is repeated in a polymer fiber, with all the heterodimers aligning their α-β axis roughly to the microtubule's main axis. The sequence of heterodimers that extends itself in a line in the α-β axis within the polymer is called a protofilament. The majority of microtubules in dividing cells are made of 13 protofilaments arranged in a cylinder, though microtubules with 9-16 protofilaments can be polymerized *in vitro* (Chaaban and Brouhard, 2017). Incorporation and loss of α,β-tubulin heterodimers, loaded with GTP, on existing microtubules occur through a process called dynamic instability (Mitchison and

Kirschner, 1984). Polymers are observed to grow and shrink at near-constant rates, rarely switching between growth and shrinkage phases. Growing and shrinking tips have distinct structures, having a blunt or tapered end when the polymer is growing (Figure 1.2 B), and a barbed end when it is shrinking (Figure 1.2 C; Mandelkov et al, 1991).

Growth occurs faster in one of the microtubule ends, the 'plus end', which corresponds to the end that exposes a β-tubulin to the solution, in the tip of the protofilaments (Mitchison, 1993). Incorporation into the polymer lattice requires β-tubulin to be loaded with GTP, but no hydrolysis is necessary for incorporation, as β-tubulin loaded with the slowly hydrolizable GTP analogue, GMPCPP, has similar growth rates as GTP-loaded β-tubulin (Hyman et al, 1992). Once in the lattice, the GTP in β-tubulin undergoes hydrolysis such that only a section of the polymer proximal to a growing end has GTP loaded β-tubulin, constituting a 'GTP cap'. This GTP cap is proposed to act as a hub to regulate microtubule dynamics (Brouhard, and Sept, 2012), and its size has been estimated *in vivo* (Seetapun et al, 2012).

Microtubules polymerized in vitro from purified α,β-tubulin produce filaments with a mixture of 13, 14, and 15 protofilaments, but microtubules polymerized in the presence of isolated centrosomes produce only microtubules with 13 protofilaments (Evans et al, 1985). The centrosome, like the kinetochore, is called a microtubule organizing center (MTOC), as it promotes the nucleation of microtubules of a set diameter. The factor present in MTOCs that allows this is the γ-tubulin ring complex (γ-TuRC). The γ-TuRC has a lock washer structure

that provides a template on which α,β-tubulin heterodimers can get incorporated into a new filament (Figure 1.2 D). γ-TuRC is also present on the lattice of existing microtubules, interacting via the augmin complex (Goshima et al, 2008).

Current models propose that the complexity of micrometer-sized microtubule-based super-structures, such as the bipolar spindle, emerge from the interplay of tubulin subtypes, post-translational modifications, and the activity of microtubule associated proteins (MAPs). Minimal systems consisting of purified tubulins and MAPs have produced unique spatial distributions of microtubules showing dynamic behaviors over time. For example, the active sorting of microtubules by kinesin-14 can lead to the assembly of asters with focused minus ends (Figure 1.2 E). The use of kinesin-1 molecules aggregated via avidin-biotin interactions can produce beating patterns over time, product of the sliding of parallel bundles of microtubules (Figure 1.2 F). And vortices of moving microtubules appear when cytoplasmic dynein is stuck to a surface, and the trajectories of microtubules start colliding with each other (Figure 1.2 G). These minimal systems provide a highly controllable environment, which allow testing for conditions necessary to observe a given behavior, also establishing what components are sufficient for its reconstitution.

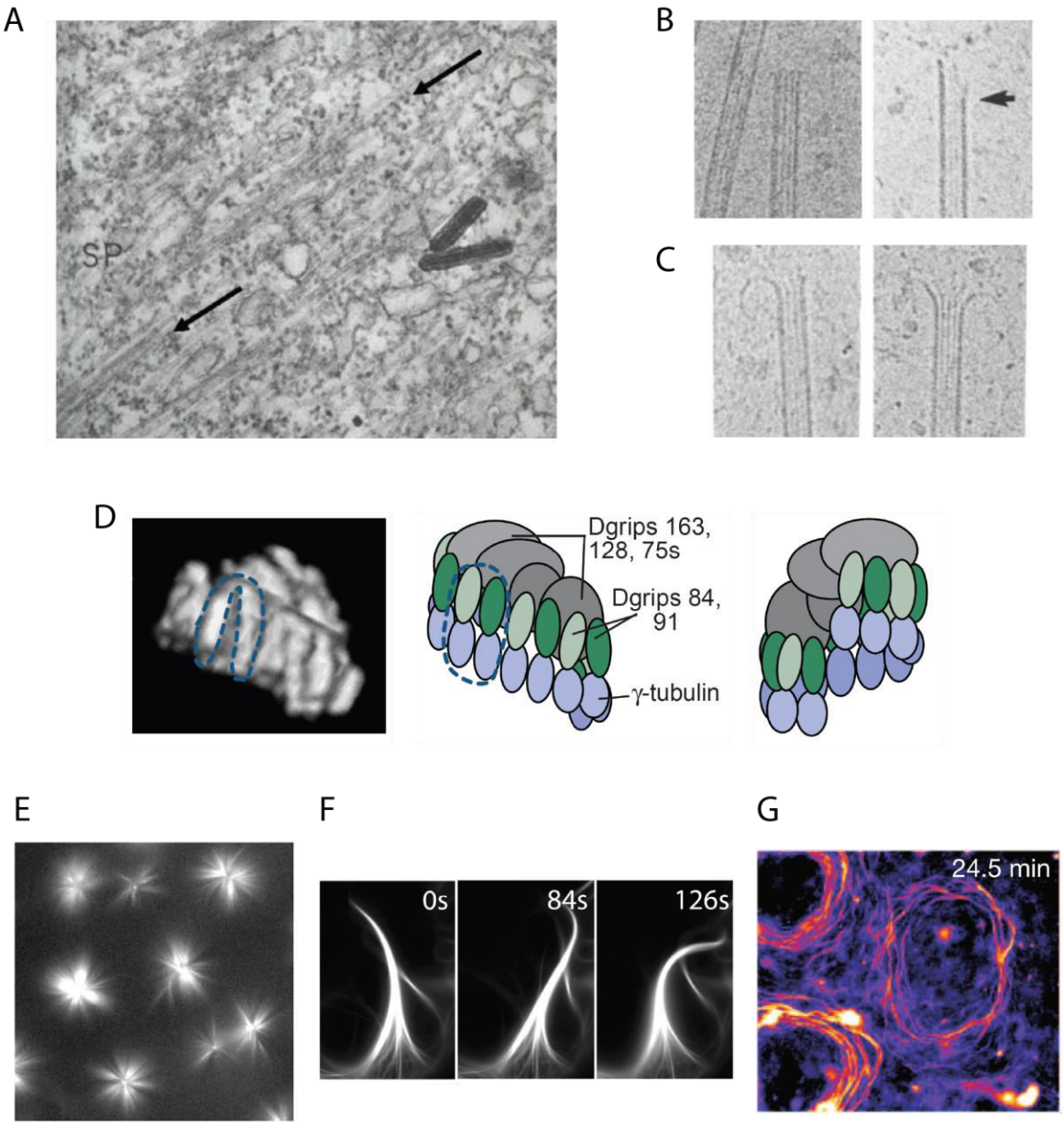

Figure 1.2 Microtubule polymerization dynamics, nucleation, and network self-organization by MAPs. **(A)** Section of a mitotic spindle of a sea urchin, imaged by an electron microscope. Arrows mark microtubules. The closest spindle pole is farther to the top-right of the image (not shown). The dark rods are a contaminant of the sample. (Adapted from Harris, 1965). **(B)** Detail of microtubules polymerized *in vitro* with purified tubulin from pig brains. Growing

filaments were flash-frozen and imaged with electron microscopy. The arrow on the right panel highlights a tapered end. **(C)** Detail of microtubules exposed to depolymerizing conditions (rapid dilution and calcium salt addition), showing coiled ends. (B and C were adapted from Mandelkov et al, 1991). **(D)** Structure of an isolated γ-tubulin ring complex (γ-TuRC). The left panel shows a reconstruction from electron-microscopic tomography of γ-TuRC, with the blue dash line highlighting the γ-tubulin small complex (γ-TuRC). The panels in the center and the right show a model of the γ-TuRC structure viewed from opposing sides, with γ-TuRC proteins indicated. (Adapted from Moritz et al, 2000). **(E)** Microtubule asters that emerge when polymerizing tubulin is incubated with kinesin-14 *in vitro* (adapted from Hentrich and Surrey, 2010). **(F)** Str (adapted from Sanchez et al, 2011). **(G)** A system composed of microtubules, molecular motors, and polyethylene glycol (as a solvent-depleting agent) assembles actively beating structures. Fluorescent imaging of bundles shows motion over time (seconds). (Adapted from Sumino et al, 2012).

1.3 The metaphase spindle

Advances in the last decades on the characterization of multiple MAPs and their interaction with microtubules now allow attempting a full description of spindle formation and function. In the metaphase spindle, the morphology and dynamics of the structure could be explained as emerging through the dynamic activities of hundreds of proteins (Reber and Hyman, 2015). Although the full modeling of the spindle will require further experimentation, a large number of proteins that have been characterized and are involved in metaphase contribute to the spindle organization in three distinct ways: controlling microtubule nucleation, regulation of filament dynamics, and mechanical stability of the spindle.

Nucleation of microtubules in the spindle (Figure 1.3 A), occur in the centrosome, which acts as a MTOC where γ-TuRC can template new filaments. In animal oocytes the metaphase spindle can assemble without the need of centrosomes. In that case it was found that a diffusible RanGTP signal near the chromosomes promoted the nucleation of microtubules (Carazo-Salas et al, 1999). An effector of this signal was identified to be TPX2 (Gruss et al, 2001), and while it is proposed to be a nucleator of microtubules, the evidence supporting that claim is lacking. Alternatively, TPX2 is also described as an activator of the kinase Aurora A, suggesting a more complex activity of the protein (Gruss and Vernos, 2004). In addition to centrosomal and cromosomal pathways to microtubule nucleation, pre-existing microtubules are thought to initiate nucleation through the augmin complex, recruiting γ-TuRC (Goshima et

al, 2008). One last process that can increase the number of microtubules in the spindle involves the severing enzyme katanin, which can cut microtubules consuming ATP (McNally and Vale, 1993). This describes four distinct pathways to regulate microtubule nucleation and filament number in the metaphase spindle.

Microtubule dynamics in the spindle differ from what is observed *in vitro* in the fact that *in vivo* the plus end experiences dynamic instability, but the minus end is relatively stabilized. Most proteins observed to regulate dynamic do so in the plus end and only a handful are described to interact with minus ends and affect dynamics (Figure 1.2 B). Two depolymerizes contribute to the regulation of dynamics of plus ends in different ways: kinesin-13, which uses lattice diffusion to reach the ends of microtubules (Hunter et al, 2003), and the processive kinesin-8 whose depolymerization rate scales with microtubule length (Varga et al, 2006). As minus end dynamics are thought to be suppressed, only the plus ends are proposed to have GTP caps. EB1 is a plus end tracking protein (+TIP) that preferentially binds the microtubule lattice with GTP-loaded β-tubulin (Maurer et al, 2012). It can recruit other +TIPs, such as CLASPs, SLAIN, and GTSE1 interacting via motifs of serine-rich regions (SKIP; Honnappa et al, 2009). XMAP215 catalyzes microtubule growth by diffusionally targeting to the microtubule tip and interacting with an α,β-tubulin heterodimer through multiple TOG domains (Brouhard et al, 2008). EB1 and XMAP215 can act synergistically to reconstitute *in vitro* the growth rate of microtubules seen *in vivo* (Zanic et al, 2013). One of proteins found to contribute to the stabilization of minus end

dynamics is Patronin, which is proposed to cap the microtubule tips protecting it from the action of depolymerases (Goodwin and Vale, 2010). These proteins, and similar proteins not mentioned, contribute to set the average length of the filaments in the spindle.

The forces exerted by MAPs on the spindle are balanced in a given steady state, and the disruption of the balance lead to changes in length and shape of the spindle (Dumont and Mitchison, 2009). The motor protein kinesin-5 is essential for spindle assembly and its depletion leads to monopolar spindles (Kapoor et al, 2000). It is proposed that the plus end directed kinesin-5 slides apart microtubules in the spindle midzone, separating the centrosomes. It also contributes to spindle pole morphology by binding parallel-aligned microtubules (Uteng et al, 2008). The minus end directed motor dynein is proposed to counter kinesin-5, but its multiple locations, including kinetochores (Pfarr et al, 1990), cell cortex (Dujardin et al, 2002), and centrosomes (Tanenbaum and Medema, 2010), among others, reveal that dynein has multiple functions in spindle assembly and maintenance beyond countering kinesin-5. The minus end directed kinesin-14 has also been proposed to antagonize kinesin-5, but it has also been proposed that can assist kinesin-5 by creating more overlaps between fibers and elongating the spindle (Simeonov et al, 2009). The non-motor cross-linker PRC1 also contributes the force balance by slowing down motion via protein friction (Forth et al, 2014), and PRC1's ortholog Ase1 can also produce expansive forces (Lansky et al, 2015). Moreover, kinesin-14 exhibits adaptive braking in the presence of Ase1 (Braun et al, 2011), but PRC1 only partially slows down

kinesin-5 (Subramanian et al, 2010). PRC1 can also interact with kinesin-4 to produce accumulation of both proteins in the end of microtubules (Subramanian et al, 2013), and to halt microtubule dynamics by recruiting kinesin-4 to the spindle midzone (Bieling et al, 2010a).

The contribution of MAPs to the assembly and maintenance of the metaphase spindle is not restricted to a single activity. Still, globally the contribution of MAPs can be divided in: regulation of nucleation to determine the microtubule number; regulation of dynamics to determine the average filament length; and regulation of mechanics to determine physical distribution of microtubules over time.

Figure 1.3 Metaphase spindle's microtubule nucleation, dynamics, and mechanics. **(A)** Mechanisms to nucleate, stabilize, and amplify microtubules in the metaphase spindle. Proteins contributing are highlighted: the augmin complex, the γ-tubulin ring complex (γ-TuRC), katanin, and TPX2 (identified as an effector of chromatin signaling via RanGTP). **(B)** Regulation of microtubule dynamics in metaphase. Various proteins are involved, including: plus-end tracking proteins (+TIPs), the minus-end stabilizer patronin, the polymerase XMAP215, and the depolymerases kinesin-13 and kinesin-8. **(C)** The spindle maintains a steady state structure by balancing forces. Antagonizing forces emerge from plus-end directed kinesins (such as kinesin-5), and minus-end directed kinesin-14 and dynein. Kinesin-14 also contributes to the mechanics of the spindle as a cross-linker of parallel microtubules. Kinesin-4, together with the cross-linker PRC1, can decorate anti-parallel alligned microtubule bundles, and tag the ends of microtubules. All three panels were taken from Reber and Hyman, 2015.

A

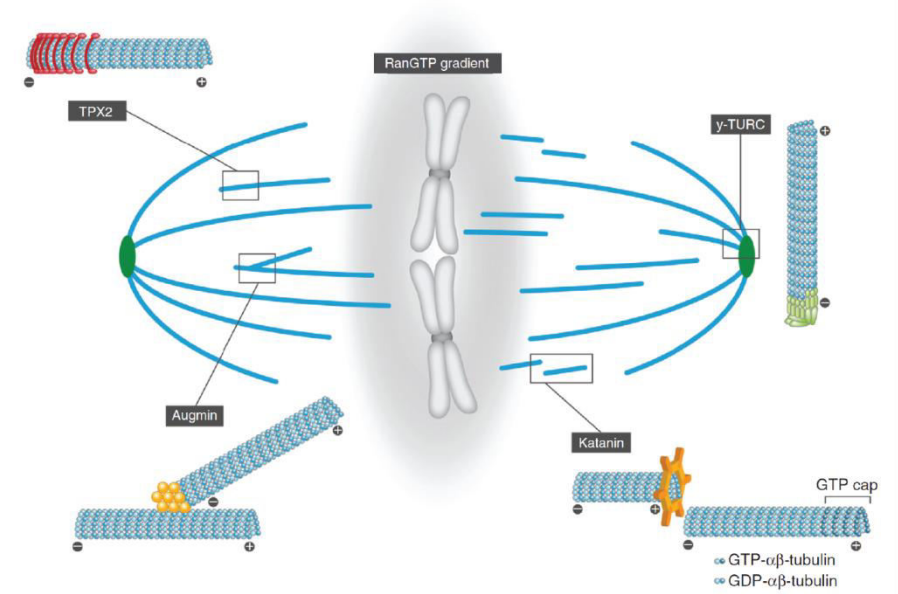
RanGTP gradient
TPX2
γ-TURC
Augmin
Katanin
GTP cap
GTP-αβ-tubulin
GDP-αβ-tubulin

B

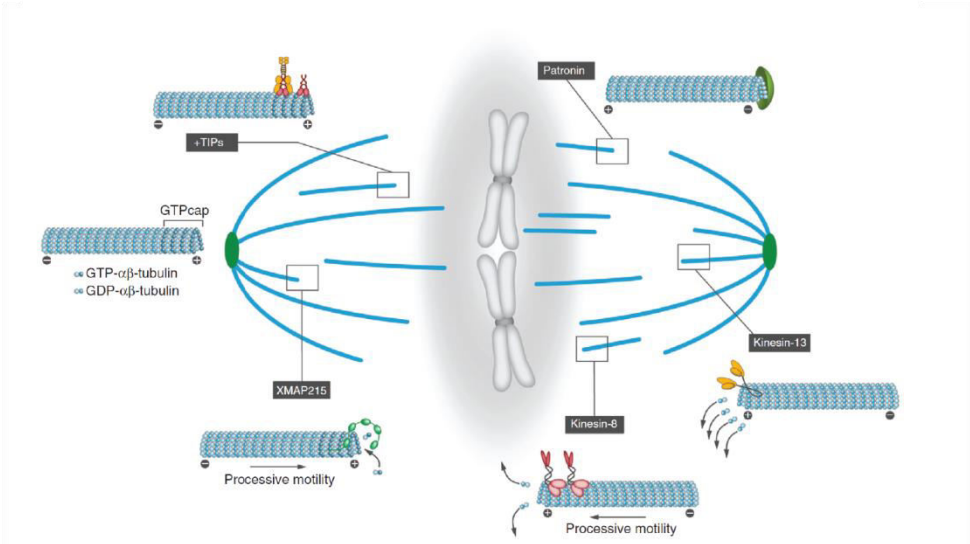
Patronin
+TIPs
GTPcap
GTP-αβ-tubulin
GDP-αβ-tubulin
Kinesin-13
XMAP215
Kinesin-8
Processive motility
Processive motility

C

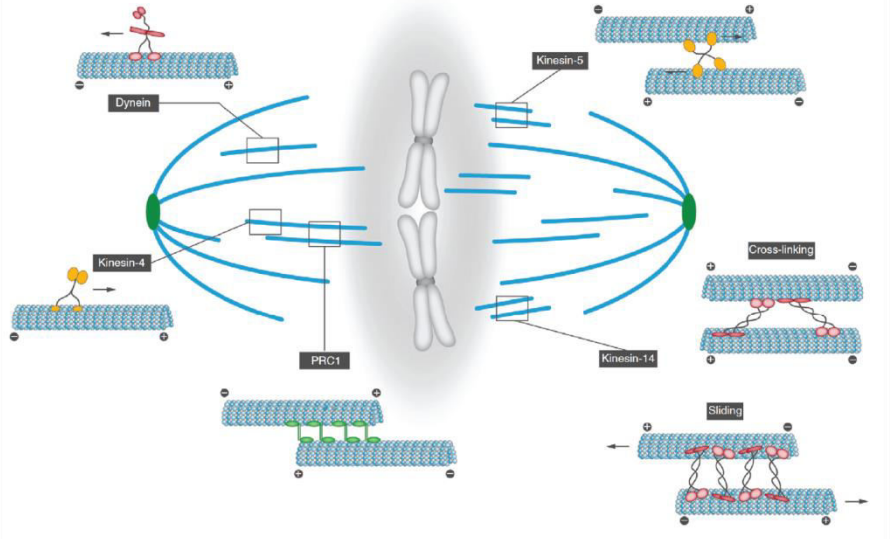
Kinesin-5
Dynein
Kinesin-4
Cross-linking
PRC1
Kinesin-14
Sliding

1.4 The anaphase spindle

The separation of sister chromatids takes place during anaphase, leading to the culmination of mitosis. The movement of chromosomes by shortening kinetochore microtubules occurs in anaphase A (Asbury, 2017). This leads to a chromosome-to-pole motion, which can be associated to the disassembly of kinetochore-attached microtubule fibers (Figure 1.4 A), by assessing cells on live cell fluorescence imaging (Cimini et al, 2004). The disassembly of the fibers can take place only on the plus ends (Maddox et al, 2000), on both ends (Ganem et al, 2005), or on the minus end while still growing the plus end (LaFountain et al, 2001). While molecular motors could contribute to the poleward motion, the depolymerization of microtubules is thought to provide the work to move chromosomes strongly attached to microtubule tips through the kinetochore (Miller et al, 2016). Models for tip-coupling (Asbury et al, 2011), consider a conformational wave (Figure 1.4 B), which can be ring based, or fibril based, or a biased diffusion mechanism that is fibril based (Figure 1.4 C). A hybrid between fibril based conformational wave and biased diffusion has been proposed (Figure 1.4 D). By the end of anaphase A the chromosomes will be located near the spindle poles.

In anaphase B the spindle elongates by sliding apart overlapping antiparallel interpolar microtubules, separating the two opposite spindle poles, and pulling along segregated chromosomes (Figure 1.4 E; Scholey et al, 2016). Several biochemical modules can collaborate in this process: (i) midzone pushing (Figure 1.4 F), by interpolar microtubule motors, or (ii) braking (Figure

1.4 G), by cross-linkers to slow down the speed of elongation from cortical pulling (Khodjakov et al, 2004); (iii) interpolar microtubule growth, providing net polymerzation in the plus end can also provide pushing forces (Figure 1.4 H *top*; Saxton and McIntosh, 1985), which can also be coupled with motor activity in a 'slide-and-cluster' model (Figure 1.4 H *bottom*; Burbank et al, 2007); (iv) cortical pulling (Figure 1.4 I) by disassembling astral filaments (Grishchuk et al, 2005) or dynein motors that pull the filaments outwards (Fink et al, 2006); and (v) interpolar microtubule minus end depolymerization that produces poleward flux (Figure 1.4 J; Brust-Mascher et al, 2004). The differential combination of these modules in different cell types produces diversity in the anaphase B mechanism. Combinations of antagonist modules can create a force balance that maintains the dynamic pre-anaphase B spindle at constant length.

Figure 1.4 Spindle changes during anaphase A and B. **(A)** Schematic of a metaphase spindle, transitioning to anaphase, sowing only the chromosomal motion taking place on anaphase A. Kinetochore-microtubule end-coupling models consider: **(B)** a conformational wave, which can be ring-based or fibril-based; **(C)** biased diffusion; and **(D)** a hybrid model where the fibrils establish interactions with curved protofilaments and the microtubule lattice. **(E)** Idealized anaphase B spindle, transitioning from early to late anaphase B, when the pole-to-pole distance is extended. The major biochemical modules that make the structure are: **(F)** pushing, or **(G)** braking by cross-linkers (such as Ase1 and Eg5); **(H)** Cortical pulling by dynein and/or by depolymerizing proteins; **(I)** interpolar microtubule net polymerization, consequence of changes on plus-end dynamics; and **(J)** interpolar microtubule minus-end depolymerization seen as poleward flux. Panels A to D were adapted from Asbury, 2017. Panels E to J were adapted from Scholey et al, 2016.

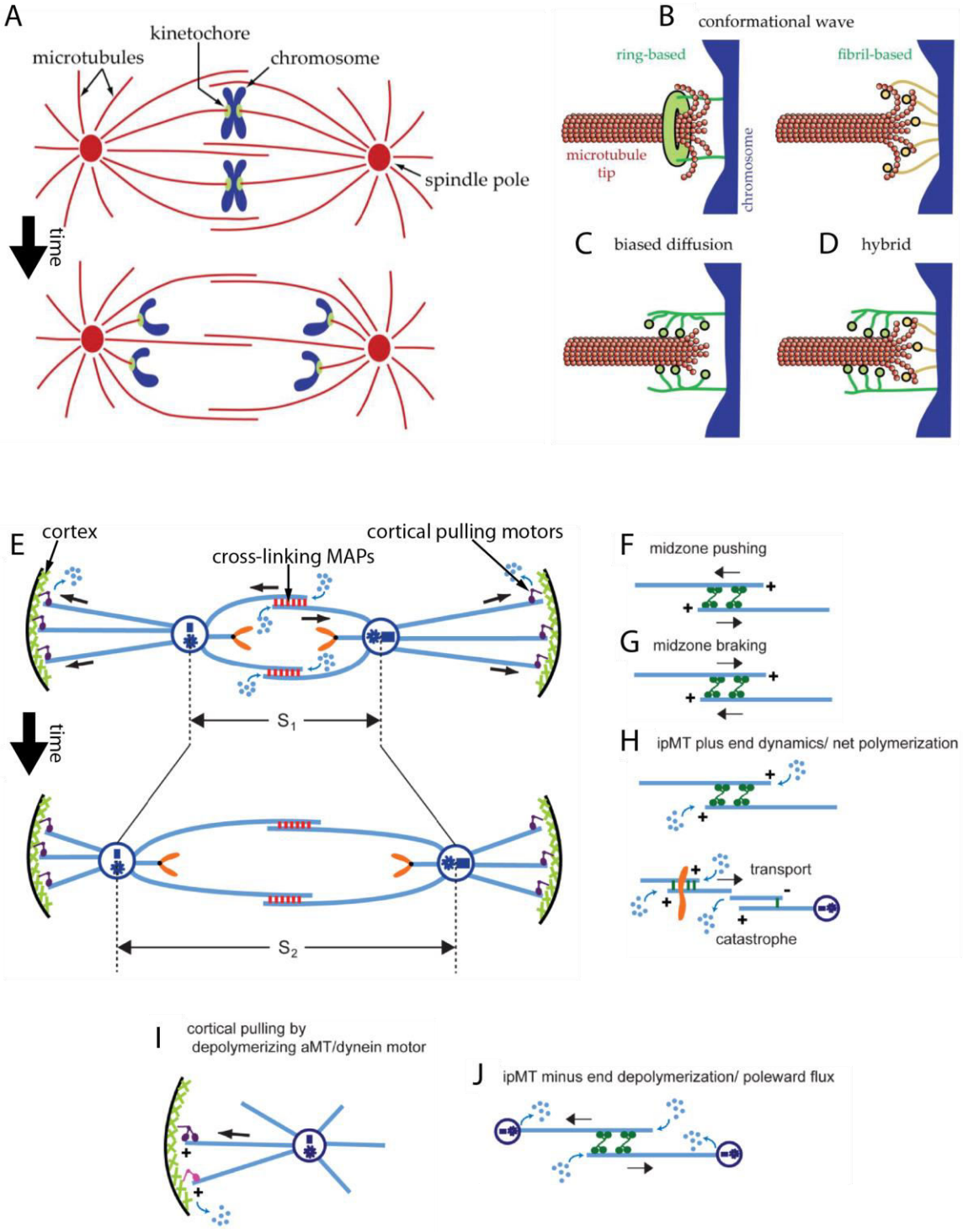
A
kinetochore
microtubules
chromosome
spindle pole
time
B
conformational wave
ring-based
fibril-based
microtubule tip
chromosome
C
biased diffusion
D
hybrid
E
cortex
cross-linking MAPs
cortical pulling motors
time
S1
S2
F
midzone pushing
G
midzone braking
H
ipMT plus end dynamics/ net polymerization
transport
catastrophe
I
cortical pulling by depolymerizing aMT/dynein motor
J
ipMT minus end depolymerization/ poleward flux

2. Materials and methods

2.1 GFP-PRC1 purification

Amino acids included in the GFP-labeled construct of PRC1 (GFP-PRC1) were amplified from a human-PRC1-isoform-1 clone (Pubmed accession NP_003972) and inserted into the bacterial expression vector pET-DUET containing a Tobacco Etch Virus (TEV) protease cleavable N-terminal hexahistidine tag. This adds a glycine and three alanines to the N-terminus of the construct after the TEV proteolysis sequence. After the TEV cleavage site a GFP was inserted, then leaving a three alanine linker between GFP and PRC1. The protein was expressed in BL21(DE3) Rosetta (Novagen) *Escherichia coli*. Protein expression was induced by 0.5 mM Isopropyl β-D-1-thiogalactopyranoside (IPTG) for 3-4 hours, at 18ºC. The following steps were done on ice or at 4 °C. Cells were lysed by brief sonication in lysis P buffer (50 mM potassium phosphate buffer [pH 8], 10 mM imidazole, 300 mM KCl, 1% Igepal, 1 mM tris(2-carboxyethyl)phosphine [TCEP], 2 mM benzene-carboximidamide [Benzamidine] hydrochloride, 1 mM phenylmethanesulfonyl fluoride [PMSF], 1 mg/mL lysozyme, and HALT protease inhibitor cocktail [Pierce]). The lysate was clarified by centrifugation at 40,000 rpm for 45 min at 4ºC in a Ti-70 rotor. The supernatant was incubated with Ni-NTA (Qiagen) for 1 hour. The Ni-NTA resin was washed with wash buffer (50 mM potassium phosphate buffer [pH 8], 10 mM imidazole, 500 mM KCl, 0.1% Tween-20, and 0.5 mM TCEP) and protein was eluted with elution P buffer (50 mM potassium phosphate buffer, 150 mM KCl, 250 mM imidazole [pH 7 with HCl], and 0.5 mM TCEP). Eluted fractions containing protein (measured by Bradford) were pooled, adding 2 mM EDTA and 10 mM 2-

sulfanylethan-1-ol (BME). Then, the protein was incubated with TEV protease (1:30 w/w) overnight. After protease treatment, the sample was dialyzed against gel filtration buffer (80 mM 1,4-piperazinediethanesulfonic acid [PIPES] buffer [pH 6.8 with KOH], 1 mM $MgCl_2$, 1 mM ethylene glycol-bis(2-aminoethylether)-*N*,*N*,*N′*,*N′*-tetraacetic acid [EGTA], 150 mM KCl, and 10 mM BME) for 2 hours. The protein was then concentrated and purified by size exclusion chromatography with a Superose 6 column (GE Healthcare) in gel filtration buffer. The peak fractions were concentrated to ~1 mg/mL in gel filtration buffer including 30% w/v sucrose before aliquoting and flash freezing in liquid nitrogen.

2.2 Microtubule polymerization and labeling

Laboratory stocks of tubulin were purified from bovine brain by two cycles of polymerization and depolymerization, followed by chromatography on phosphocellulose (Williams and Lee, 1982). Purified tubulin was labeled either with biotin or X-rhodamine dye, based on published methods (Hyman et al., 1991). Briefly, tubulin was polymerized in a pH 6.8 buffer with 30% m/v glycerol and 1 mM guanosine triphosphate (GTP), at 37ºC. Then, microtubules were transferred to a pH 8.6 buffer and mixed with either succinimidyl-6-(biotinamido)-6-hexanamido hexanoate (NHS-LC-LC-Biotin; Thermo Fisher, catalog number 21343), or 1-[[(2’,3’,6’,7’,12’,13’,16’,17’-octahydro-3-oxospiro[isobenzofuran-1(3H),9’-[1H,5H,9H,11H,15H]xantheno[2,3,4-ij:5,6,7-i’j’]diquinolizin]-5-yl)carbon-yl]oxy]-2,5-pyrrolidinedione (5-carboxy-X-rhodamine N-succinimidyl ester or X-rhodamine-NHS; Thermo Fisher Invitrogen, catalog reference C6125), in either a

10X or 25X molar ratio to tubulin, respectively. The labeling reaction was carried for 40 minutes. After quenching the reaction, microtubules were depolymerized on an ice water bath. Then an additional cycle of polymerization and depolymerization was done. Finally, labeling efficiency was quantified and aliquots were flash frozen in liquid nitrogen. Quantification of X-rhodamine labeling was done measuring absorption at 280 and 585 nm, and for bioinylated tubulin changes in absorption at 550 nm were measured using 4-Hydroxyazobenzene-2-carboxylic acid/avidin (HABA/avidin; Sigma-Aldrich catalog reference H2153). For a 25X molar excess of X-rhodamine-NHS a 0.9:1::X-rhodamine:tubulin ratio was observed, and for a 10X molar excess of NHS-LC-LC-biotin, 1.3:1::biotin:tubulin.

For microscopy and optical trapping assays, microtubules were polymerized in BRB80 buffer (80 mM PIPES [to pH 6.8 with KOH], 1 mM $MgCl_2$, 1 mM EGTA), with 1 mM dithiothreitol (DTT), at 37ºC. Microtubules without a polarity mark were polymerized at 3-3.5 μM tubulin and 0.15-0.2 mM guanosine-5'-[(*α*,*β*)-methyleno]triphosphate (GMPCPP). For brightly labeled microtubules a molar ratio of 3:50 of X-rhodamine to tubulin was used, by including X-rhodamine labeled tubulin in the polymerization mix, and the polymerization was carried for 90-120 minutes. For dimly labeled microtubules the ratio was set to 1:50, and the reaction lasted 30 minutes. Polarity marked microtubules were polymerized sequentially. First, a mix containing 11 μM tubulin and 0.5 mM GMPCPP, at a molar ratio of 3:50 of X-rhodamine to tubulin, was incubated for 20 minutes at 37ºC. Then, 2 μL of the mix were transferred into a 30 μL solution containing 60

nM X-rhodamine labeled tubulin, 2 μM 1-Ethylpyrrole-2,5-dione (N-ethylmaldeimide; NEM) treated tubulin, and 4.5 μM total tubulin (molar ratios 1:15:75, respectively). The solution was incubated for 60 minutes at 37ºC. To get any microtubules copolymerized with biotin labeled tubulin, a molar ratio of 1:10 of biotin to total tubulin was included in the polymerization mix.

2.3 Microscope glass treatment

Microscope slides and coverslips were functionalized in a manner similar to published protocols (Bieling et al, 2010b). Petrographic slides were purchased from Fisher Scientific (catalog reference NC9312106) and coverslips from Thermo Scientific Gold Seal Cover Slips (catalog number 3305, thickness #1, 18 mm x 18 mm). The glass was transferred to 0.1 M KOH and sonicated for 5 minutes. After sequential immersion in ethanol and acetone, the glass was treated with an aminosilanizing solution (Vectabond; Vector Laboratories catalog reference SP-1800). The glass was then dried and its surface covered with a solution containing 0.1 M $NaHCO_3$ and polyethylene glycol succinimidyl valerate (PEG-SVA). Coverslips were treated with a mix of 25% m/v methoxy-PEG-SVA (MW 5,000; Laysan Bio) and 0.3% m/v biotin-PEG-SVA (MW 5,000; Laysan Bio). Slides were treated with a 25% m/v methoxy-PEG-SVA alone. After 3 hours of incubation, the glass was rinsed with water, dried, and stored in a desiccator at room temperature.

2.4 Rigor kinesin purification

The plasmid containing the rigor kinesin construct was gifted by Dr. Sarah Rice. The construct contains the first 560 amino acids of the human kinesin heavy chain protein (K560), with several cysteines mutated to serines and alanines, and glycine 234 mutated to alanine, as described before (Rice et al., 1999). Following the C-terminus of this cys-light K560 G234A construct, there is a hexahistidine tag and then nine lysines before the stop codon. The protein was expressed in BL21(DE3) Rosetta (Novagen) *Escherichia coli*. Protein expression was induced by 0.2 mM IPTG for 16 hours, at 19ºC. The following steps were done on ice or at 4 °C. Cells were lysed by brief sonication in lysis K buffer (50 mM sodium phosphate buffer [pH 8], 20 mM Imidazole, 250 mM NaCl, 1 mM $MgCl_2$, 0.5 mM adenosine triphosphate (ATP), 1 mM TCEP, 2 mM Benzamidine hydrochloride, 1 mM PMSF, and HALT protease inhibitor cocktail [Pierce]). The lysate was clarified by centrifugation at 40,000 rpm for 40 min at 4ºC in a Ti-45 rotor. The supernatant was incubated with Ni-NTA (Qiagen) for 1 hour. The resin was washed with lysis K buffer, and protein was eluted with elution K buffer (25 mM PIPES, 500 mM imidazole [pH 7 with HCl], 150 mM NaCl, 1 mM $MgCl_2$, 0.2 mM ATP, 1 mM TCEP). Eluted fractions containing protein (measured by Bradford) were pooled and mixed with an equal volume of dilution buffer (25 mM PIPES [pH 6.8 with NaOH], 50 mM NaC, 3 mM $MgCl_2$, 2 mM EGTA, 0.2 mM ATP, 1 mM DTT). The solution was injected to an anion exchange column (MonoQ 5/50 GL; GE Healthcare), the column washed until base line with MonoQ Low Salt buffer (25 mM PIPES [pH 6.8 with NaOH], 100 mM NaCl, 2 mM $MgCl_2$, 1 mM EGTA, 1 mM DTT, 0.1 mM ATP). Protein elution was carried with

10 column volumes of a NaCl gradient from 100 mM to 1 M. Peak fractions pooled, concentrated to 0.1-1 mg/mL, and flash frozen in liquid nitrogen.

Fractions were tested for microtubule binding by non-specifically coating the surface of microscope flow chambers, washing, flowing a suspension of X-rhodamine labeled microtubules, and looking in the microscope for microtubules stuck to the coverslip surface. For high protein concentrations (above 1 mg/mL), a high number of microtubules was seen on the surface. The fractions used for bead coating typically presented surface decoration down to a concentration of 0.1 mg/mL, below which the microtubule coverage of the surface dropped sharply.

2.5 Bead coating

Beads were purchased from Polysciences Inc (catalog number 08226; carboxylate microspheres 1.00 μm, 4.55 x 10^{10} particles/mL). The beads were always kept below 4 ºC until flowed to the microscope flow chamber. The suspension of beads was exchanged to a 100 mM HEPES buffer (pH 8 with KOH), and then diluted 50-fold in BD buffer (BRB80 plus 1 mM DTT). The diluted beads were incubated with rigor kinesin at a molar ratio of 1:10^6 for 15 minutes.

After washing with BD buffer, the coated beads were resuspended in BDTC buffer (BD buffer, plus 0.5 mg/mL alpha-casein and 20 μM taxol). The coating was timed such that the coated beads would be ready at the time of the final flow to the microscope flow chamber, at a final concentration of ~0.5 x 10^8 beads/mL. The molar ratio of kinesin to beads was reduced if too many clumps of

several beads were seen relative to non-clumped beads (more than one clump every ten non-clumped beads), and increased if less than half of trapped beads could remain attached to microtubules on force spikes of ~20 pN.

2.6 TIRF microscopy

Image acquisition was done on a Nikon Eclipse Ti-U inverted microscope, equipped with dual-mode TIRF, epi-illumination, and transillumination optics. TIRF excitation light was produced by 488 nm laser (Spectra-Physics) for GFP and a 561 nm laser (Cobolt Jive) for X-rhodamine, and passed through excitation filters (Chroma part number ET572/35x for the 561 nm light and Semrock part number FF01-482/563-25 for both wavelengths). The mechanical shutters (Ludl part number 90M039) were isolated from the microscope's optical table to reduce the vibration noise associated with shutter action. A dual-band dichroic mirror (Semrock part number Di01-R488/561) was used to reflect the both excitation wavelengths, while transmitting the fluorescence emission wavelengths and the trapping laser's light. Microscope flow chambers were mounted on a piezoelectric stage with closed-loop control on the three axes (Mad City Labs; Nano LP-200). A high numerical aperture 100X objective (Nikon; CFI Apo TIRF 100X Oil) was used both for fluorescence imaging and to focus the trapping laser near the image's focal plane. Emitted light passed through an IR-cut filter (Newport; FSR-KG3) to reduce background light from the trapping laser, and through an emission filter, before reaching the camera. Depending on which channel was being imaged the wheel was moved to present either a GFP emission filter

(Semrock part number FF02-520/28-25), a Texas Red emission filter (Chroma part reference ET630/75m), or no filter. The filters were mounted on a servo-controlled filter wheel (Ludl part number 96A351). Acquisition was done by an Andor iXon DU-897 EM-CCD camera, using either Andor iQ or NIS-Elements software.

2.7 Single spot tracking and intensity data acquisition and analysis

Imaging of single spot GFP-labeled proteins bound to microtubules was done on microscope flow chambers built from PEG-treated glass slides and coverslips. Two 5 mm thick and 20-30 mm long strips of double sided tape (Scotch) were stuck on the surface of the slide, set in parallel and with a separation of 5 mm. The coverslip was pressed on the taped surface, with the treated glass facing the interior of the chamber, leaving a volume of 6-8 µL. The chamber was filled with BDC buffer (BRB80, 1 mM DTT, 0.5 mg/mL alpha-casein) and then incubated with 0.2 mg/mL Neutravidin (Thermo Scientific, catalog number 31000). After washing with BDTC buffer, biotin labeled and X-rhodamine labeled (either dimly or polarity marked) microtubules were flowed to the chamber and incubated for 5 minutes. The microtubule concentration of the suspension flowed in was diluted to get a surface decoration of 20-40 microtubules per field of view (80 µm by 80 µm square). Excess microtubules were washed away, and a final solution with GFP-labeled protein was included, and images were acquired. For the Augmin holo-complex and sub-complexes a protein concentration of 0.1 nM was used, in a buffer solution containing BRB80,

20 μM taxol, 0.5 mg/mL alpha-casein, 10% sucrose, 2 mM DTT, 200 μg/mL glucose oxidase, 35 μg/mL catalase and 4.5 μg/mL glucose. Image acquisition was carried with an exposure time of 100 ms, preamp gain of 5.1x, and EM gain of 200, at a rate of 4.4 frames per second, and including an ND2 filter in the light path before sample excitation. For GFP-PRC1 the protein concentration was 10 pM (as dimer), in BDTC buffer, supplemented with 1 mM DTT, 200 μg/mL glucose oxidase, 35 μg/mL catalase and 4.5 μg/mL glucose. Acquisition was done with an exposure time of 100 ms, preamp gain of 5.1x, EM gain of 200, at a rate of 1 frame per second, and including an ND8 filter in the light path before sample excitation. In both cases 100-300 frames were acquired, along with a single image of the X-rhodamine labeled microtubules (exposure time of 100 ms, preamp gain of 5.1x, EM gain of 200).

Kymographs were made using the Image J plugin made by J. Rietdorf and A. Seitz, from EMBL (https://www.embl.de//eamnet/html/body_kymograph.html). Kymographs are time versus space plots, assembled from a time lapse acquisition, over a user-defined segment on the acquired images. The intensity values on the distance/space of the segment are plotted in sequence over the frames of the time lapse. Spot detection and track assembly was done using the Speckle Tracker J plugin for Image J (Smith et al, 2010). The sequence of positions for each track was imported to a custom written routine in Excel. The displacements of each track were projected to a vector with an orientation determined from the microtubule associated to that track. From a sample set made of ~700 tracks collected from three or more flow chambers, the empirical

cumulative distribution function (CDF) was obtained. For time (t) in seconds, the paired data (t, 1-CDF) was fitted to the exponential sum $1 - \mathrm{CDF(t)} = \mathrm{A_1 e^{-t/\tau_1}} + \mathrm{A_2 e^{-t/\tau_2}}$, using a 'least-squares' approach in MATLAB. The second part of the sum was excluded in the case of the mono-exponential fit on Hice1•GFP-hDgt6-NTD data. The parameters A and τ are the relative amplitude and the mean dwell time, respectively, and they are expressed as the mean value for the estimator ± the 95% confidence intervals extracted from the fit. The mean square displacement (MSD) of each set was calculated and the paired data (t, MSD) was fitted to the line $\mathrm{MSD(t) = C + 2Dt}$, where D is diffusivity, and C is a constant.

GFP spot intensity data was acquired on microscope flow chambers built with non-functionalyzed glass. The coverslips and slides were briefly sonicated in 0.1 M KOH, then washed and dried, and used for the chamber assembly. Purified and GFP-labeled proteins were flowed to the chamber at a concentration between 5-50 pM. For the experiments related to the Augmin holo-complex and sub-complexes (nomenclature is specified on Chapter 3), the GFP-labeled proteins tested were Hice1•GFP-hDgt6-NTD, the tetramer tagged as GFP-Cep27, the tetramer tagged as GFP-hDgt6-NTD, the octamer, the holo-complex, and GFP. For experiments related to GFP-PRC1, the proteins assess were GFP-PRC1, GFP-Eg5-FL, and GFP-Eg5-513 (the last two proteins obtained as described in Kapitein et al, 2008). Following a brief incubation, the chamber was washed with the same buffer as the one used on the imaging of microtubule bound single spots and sealed with VaLaP (mix of an equal weight of Vaseline, lanolin and paraffin) before image acquisition. After the GFP fluorescence

image's focal plane was found, the excitation laser was turned off, the piezoelectric stage was moved 100~200 μm away in a direction parallel to the focal plane, and finally a time lapse of 100-300 frames was acquired using the same conditions of the microtubule bound single spots' acquisition.

Spot detection was done using Speckle Tracker J. The first three frames of the acquired time lapse were averaged and the resulting imaged was cropped, excluding 20 pixels from the edges. Detected spots were above five standard deviations of the mean intensity value of the image, with a maximum diameter of 6 pixels, and at least 12 pixels away center-to-center from other detected spots. The positions reported by Speckle Tracker J were exported to a custom written routine in Excel that sums the intensity on a six pixel diameter circle around the position, subtracting the background from a disc with internal diameter of six pixels and external diameter of twelve surrounding the spot. Intensity histograms were constructed from spot data of three or more independent microscope flow chambers.

2.8 Optical trapping and force measurements

Manipulations and force measurements were done with a single beam laser trap, set to allow imaging simultaneously. Light produced by a diode pumped 1064 nm laser (Crystalaser, catalog reference CL1064) was coupled to an optical fiber. The fiber-coupled beam was collimated (Thorlabs, catalog reference F260FC-C), and passed through a series of lenses and mirrors to expand and steer the beam. The laser's intensity was attenuated using neutral

density filters set before being merged into the inverted microscope's light path using a dichroic mirror (Chroma, catalog reference z900dscp). The beam was focused by the objective 1~2 μm above the focal plane of the image captured by the EM-CCD camera. The bead position was monitored with a photodiode quadrant array that functions as a position-sensitive detector (Pacific Silicon Sensor, catalog reference QP50-6SD2). After the beam passed the microscope chamber, the light was collected by an oil-immersion condenser (Nikon, catalog reference MEL41410), and was reflected by a shortpass dichroic mirror (Thorlabs, catalog reference DMSP805L). The mirror reflected the IR beam to one side of the microscope and allowed most of the visible light from the transillumination lamp to go through. The reflected beam passed through a longpass filter to reduce visible light (Throlabs, catalog reference FEL0900), and was focused on the position detector.

Two voltage differences, between left-right pairs and between top-bottom pairs, and the sum of the four quadrants' voltages were recorded using a custom written routine in LabVIEW, via an analog-digital converter (National Instruments, catalog reference PCI-6251). The routine also recorded a TTL signal produced by the EM-CCD camera, with the high voltage signal on when the camera was acquiring an image and the low voltage when the camera was idle. Additionally, the routine monitored the positions of the piezoelectric stage and provided the input position signals to the closed-loop control. When the routine interacted with the quadrant photodiode, the camera's TTL, and the piezoelectric stage, it operated at 100 Hz.

To determine the trap sensitivity non-functionalyzed microscope chambers were loaded with beads diluted in a high ionic strength solution. After washing the chamber, beads stuck on the glass surface were observed in the microscope using transillumination. Data acquisition was done on a custom written routine in LabVIEW, recording: the piezoelectric stage position (X, Y, Z), the sum of voltages of the four quadrants on the quad detector (Vsum), and the voltage difference between two orthogonal halves of the quadrant photodiode (ΔVx, ΔVy). Data analysis yielded the trap's sensitivity in the X and Y axes. To determine the X sensitivity, for each Y and Z values the paired data (X, ΔVx/Vsum) was fitted to the line ΔVx/Vsum =A+BX. For each Z value the slopes of all Y values are averaged if they are above 90% of the maximum slope obtained for the set of Y values. For all the Z values in the data, the highest value of the averaged slopes is kept as the sensitivity on the X axis. The sensitivity on the Y axis was determined with a similar analysis, swapping X for Y. For laser transmittances between 10% and 70%, the recorded sensitivities (both in X and Y) were ~1 V/(V.μm).

To determine the trap stiffness PEG-coated microscope chambers were loaded with uncoated beads diluted in BDTC buffer. Beads floating near the coverslip surface were trapped and kept 1~2 μm above the surface. During 10-30 seconds, the voltage differences and the voltage sum were recorded at 20 KHz. Data was collected at three laser transmittances between 10% and 70% for each bead trapped. The analysis of the data was done in Excel. From the voltages the position over time (in the X and Y axes) was determined using the trap

sensitivities. Then, the variance of the position on each axis was used to calculate the trap stiffness following the equation: $k_i = k_b T/\langle x_i^2 \rangle$, where i is either X or Y, k_i is the trap stiffness, k_b is Boltzmann constant, and T is the temperature. The paired data (Vsum, k_i) produced from combining the data from all transmittances used in the acquisition was fitted to a line. The slope was used as the stiffness value to apply regardless of the transmittance used in the experiments, and had a value of 0.02-0.03 pN/(nm.Vsum).

2.9 Microtubule bundle manipulation assays

Microscope flow chambers were prepared as described for the single spot tracking experiments, up to the point when the excess of biotin-labeled microtubules was washed away. After that wash, 0.2 nM GFP-PRC1 (as dimer) was flowed and incubated for 5 minutes. Then a mix of brightly X-rhodamine labeled microtubules and 0.2 nM GFP-PRC1 was flowed in. After a 15 minute incubation, the solution in the chamber was exchanged to either buffer BDTC80 (BDTC buffer supplemented with 80 mM KCl), with 0.05 nM GFP-PRC1, or buffer BDTC100 (BDTC buffer supplemented with 100 mM KCl), with 0.5 nM GFP-PRC1. Finally, the exchange solution was supplemented with 1 pM rigor-kinesin-coated beads, 200 µg/mL glucose oxidase, 35 µg/mL catalase and 4.5 µg/mL glucose, the supplemented solution flowed into the chamber, and the chamber sealed with VaLaP, before proceeding to the microscope.

Bundles were identified by finding a bright microtubule with an elongated GFP signal colocalizing only in a section of its length. After a bundle was found, a

nearby floating bead (observed by transillumination) was captured and brought close to the bright microtubule, in a section with no GFP-PRC1 decoration, and 2~4 μm away from the edge of the GFP signal. Successful attachment between the bead and the bright microtubule could be confirmed by moving the piezoelectric stage slightly and detecting bead displacement in the quadrant photodiode that would persist after stage movement stopped. If the bead attachment held for more than 10 seconds, the bundle would be then manipulated. Otherwise, another bead would be brought to retry attachment. Images for GFP (exposure time of 100 ms, preamp gain of 5.1x, EM gain of 200), X-rhodamine (exposure time of 100 ms, preamp gain of 5.1x, EM gain of 200), and transillumination (exposure time of 50 ms, preamp gain of 5.1x, EM gain of 4) were acquired before bringing a bead, and again once durable bead attachment to the bright microtubule was obtained.

For the bundle flipping experiments, once a bead was attached to the bright microtubule, the piezoelectric stage was manually moved to strip the bundle. During the motion, the X-rhodamine channel was streamed, collecting images at 2~3 frames per second. The motion was oriented to move the bead towards the bundle's GFP signal and 30~45º away from the bundle's main axis. When the bundle was almost fully peeled, motion was slowed down and controlled to produce a pivoting motion and an inversion in the orientation of the bead-attached microtubule. The microtubules were then aligned with an orientation inverse of the original, and images were acquired for GFP, X-rhodamine, and transillumination. Inmediately after the images were acquired the

trap laser was turned off, and a time lapse was acquired for the GFP and X-rhodamine channels, collecting images every five seconds for a 300~600 second interval. After the time lapse, a new set of GFP, X-rhodamine and transillumination images were collected. At this point the bead was trapped again, and the stage position was manually moved to reverse the bundle orientation as done on the first inversion, while streaming on the X-rhodamine channel. Upon re-aligning the bundle to its original orientation, images on GFP, X-rhodamine, and transillumination were collected. The trap laser was then turned off, and a new time lapse on GFP and X-rhodamine was acquired, collecting one frame of each channel every five seconds for 300~600 seconds.

For the bundle pulling experiments, once the bright microtubule of the bundle was attached to the bead, the angle of orientation of the bundle relative to the stage axes was estimated from the bundle image acquired on the GFP channel. Then, a custom routine written in LabVIEW was executed (similar to the one mentioned in the optical trapping subsection), which allowed moving the piezoelectric stage in the direction of the angle measured, while recording the stage position, the quadrant photodiode's voltages and the camera's TTL signal state. Stage movement was executed sequentially. First there was a 10-second interval with no motion. Then, motion was started at constant velocity of either 50 or 200 nm/s, for a period of 60-180 seconds. The duration of the motion was set such that the distance travelled by the stage would exceed the estimated length of the GFP signal of the bundle. Lastly, the stage was kept without motion for 10 seconds. Around five seconds after initializing the LabVIEW routine, a time lapse

was started manually, acquiring GFP channel images at 1 frame per second, during an interval long as the stage movement interval plus 10 additional frames/seconds. After the manipulation ended, images were collected of the bundle for GFP, X-rhodamine and transillumination.

2.10 Bundle manipulation data analyses

Images were analyzed with ImageJ. The quadrant photodiode and piezoelectric stage data were analyzed using custom written routines in LabVIEW.

For the bundle flipping experiments the bundle's GFP signal intensity was determined by adding all the pixel values of a hand drawn region of interest (ROI). The ROI was drawn to include at least three pixels outside the area occupied by the bundle's GFP signal. The same ROI was used to determine the sum of all pixel values of a background area with no GFP signal that was then subtracted to the bundle's intensity. The bundle's length estimation depended on whether a localized, and high intensity, GFP signal was bound to the bundle or not. With a high GFP signal, a line scan on the major axis of the bundle was extracted for the GFP signal. On the edges of the bundle, the positions of the major drops in the GFP signal line scan are used to define the bundle length. With low GFP decoration, the X-rhodamine channel images were also analyzed. One edge of the bundle was defined at the end of the bright microtubule farthest from the bead attachment before bundle manipulation, while the other edge was determined from the position of the end of the surface bound microtubule after the bundle was disassembled by manipulation.

For the bundle pulling experiments, the GFP signal intensity and the initial bundle length were determined as it was done for the bundle flipping experiments. The GFP time lapse, the stage position data, and the force data were set to the same time reference using the camera's TTL signal. Each frame of the time lapse was linked to the mean time of the interval of the high voltage state TTL signal associated to the frame. The estimator of rate of change of voltage differences in the photodiode quadrant was used: $\Delta\Delta V(t_i)^2 = (\Delta V_X(t_{i+1}) - \Delta V_X(t_i))^2 + (\Delta V_Y(t_{i+1}) - \Delta V_Y(t_i))^2$, where t_i is the i^{th} time in the data set collected and t_{i+1} is the following one, and ΔV_X and ΔV_Y are the voltage differences in the quadrant detector, in the X and Y axes respectively, for a given time. The rupture time of the bundle was defined as the average time of an interval of time that satisfied $\Delta\Delta V(t_i)^2 > 6\langle\Delta\Delta V(t_i)^2\rangle$, and was also no more than three frames away from the GFP signal intensity associated with bundle rupture. The length of the bundle was estimated by $L = v_{STAGE}(t_R - t)$, where v_{STAGE} is the piezoelectric stage's velocity during motion (either 50 or 200 nm/s), t_R is the rupture time of the bundle, and t is time. The sliding regime was defined by examination of the GFP signal length (defined as done for the bundle flipping experiments), and comparison with the length estimated from constant velocity change from the rupture time. If both lengths were closer to each other by two pixels distance (308 nm) the data was considered to be in the sliding regime. The voltage measurements in the photodiode were translated to force in the X and Y axes, using the sensitivity and stiffness of the trap. The force was then projected to the axis of stage motion. Force data were discretized for data pairing with

bundle length and GFP intensity by averaging the projected force during the time intervals where the camera's TTL signal was on its high voltage state.

2.11 Stochastic simulations

Simulations were written and run in Python 2.7 with the NumPy and SciPy packages installed. When generating pseudo-random numbers, a single-precision 32-bit floating point was used, defined between zero and one. The definition interval contains zero, but excludes one, so probability densities were modeled with the lower end of their interval defined as a close bracket, and the higher end as an open bracket. The time length of the interval (ΔT) between steps of the simulation was set after simulating data with ΔT of different orders of magnitude, and a constant step number of 100000. The simulations in this case did not choose randomly which direction of stepping was checked first, but the probability on the positive direction ($PPLUS$) was always compared to a random number first. The mean displacement over time interval of the cross-linkers was computed, and after fitting a line to the paired data the ΔT that produce a slope of zero was chosen as the ΔT to be used in simulations of sliding bundles.

3. Single-molecule TIRF characterization of augmin

3.1 Background information

Proper assembly and maintenance of a bipolar spindle in a dividing cell depends on the regulated nucleation of microtubules. Current models describing this regulation include microtubule organizing centers that recruit γ-tubulin and associated proteins (Lüders and Stearn, 2007). In dividing somatic cells of vertebrates, centrosomes function as organizing centers, but it has been established that they are not required for the assembly of mitotic and meiotic spindles (Wadsworth and Khodjakov, 2004; Dumont and Desai, 2012), indicating the existence of nucleation pathways that do not depend on centrosomes. Two pathways have been proposed to be involved in the centrosome-independent nucleation of microtubules. The first one involves the GTPase Ran and the Aurora B kinase complex (Karsenti and Vernos, 2001; Kelly and Funabiki, 2009). The second one involves augmin, a protein complex that regulates the recruitment of tubulin to the bipolar spindle (Goshima et al., 2008; Lawo et al., 2009).

In humans, the augmin complex is constituted by eight proteins: Hice1, hDgt6, UCHL5IP, Cep27, C14orf94, Ccdc5, hDgt5, hDgt3 (Figure 3.1 A; Lawo et al., 2009). Proteins of the complex were first identified in *Drosophila* in an RNAi screen for defects on gamma-tubulin (shortened to “Dgt”; Goshima et al., 2007). The proteins showing Dgt phenotypes, and reduced levels of gamma-tubulin in the spindle body relative to the spindle pole levels, were also found to co-immunoprecipitate in *Drosophila* (Goshima et al., 2008). Later, the list of proteins in the complex was extended to eight both for *Drosophila* (Uehara et al., 2009)

and humans (Uehara et al., 2009; Lawo et al., 2009). Of the proteins of the complex, Hice1 has been shown to bind to microtubules in vitro (Wu et al., 2008), and hDgt6 co-immunoprecipitates with NEDD1, a component of the gamma-tubulin ring complex, thus placing augmin as the link between pre-existing microtubule filaments and the site of nucleation for new filaments (Figure 3.1 B). Additionally, yeast two-hybrid assays established that hDgt6 and Hice1 interact directly (Uehara et al., 2009). Moreover, a construct including only the first 149 amino acids of Hice1 retains microtubule binding capabilities of the full length protein, and a C-terminal truncation of hDgt6 (hDgt6[1-438]) does not immunoprecipitate NEDD1, and only partially rescues the recruitment of tubulin to the spindle in cells depleted of endogenous hDgt6 (Uehara et al., 2009).

There is evidence linking augmin to the regulation of centrosome-independent microtubule nucleation in the bipolar spindle. Images of dividing cells show lower microtubule signal intensity in the spindle body, relative to the spindle poles, when proteins of the augmin complex are knocked-down (Goshima et al., 2008; Uehara et al., 2009). Additionally, in *Xenopus* egg extracts the depletion of augmin impairs microtubule nucleation in acentrosomal spindles assembled around DNA-coated beads (Petry et al., 2011). Similarly, in *Drosophila's* embryonic spindles (Hayward et al., 2014) microtubule generation around chromatin requires augmin. Moreover, surface immobilized microtubules exposed to *Xenopus* egg extracts, supplemented with RanQ69L and TPX2, nucleate new microtubules and form a branching pattern, but this pattern is abolished if augmin is immunodepleted from the extract (Petry et al., 2013).

Finally, electron tomography studies of human metaphase spindles show that microtubules' putative minus ends that are far from the centriole disappear when augmin is knocked down (Kamasaki et al., 2013). Also, the authors observe ~30 nm long high electron density rods connecting centriole-distant minus ends to the lattice of nearby microtubules.

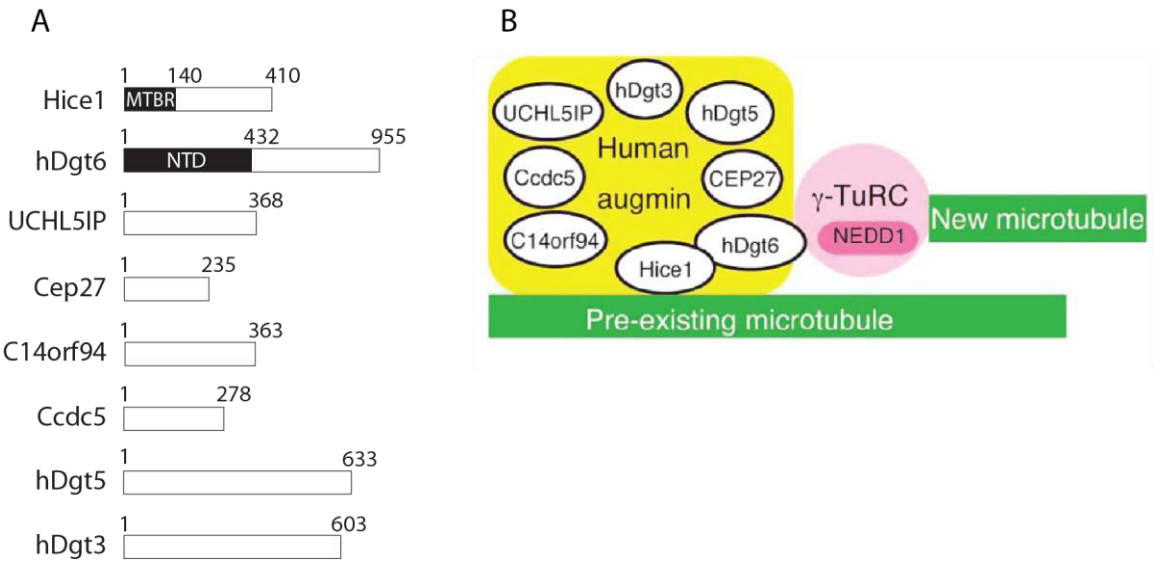

Figure 3.1 The augmin complex and its putative function. (A) Eight proteins make up the holo-complex of augmin in humans. The highlighted regions are the microtubule binding region (MTBR) of Hice1, which is the only protein in the complex described as a microtubule associated protein (Wu et al., 2008), and the N-terminus domain of hDgt6 (hDgt6-NTD), which was found to interact with NEDD1, a component of the gamma-tubulin ring complex (γ-TuRC; Uehara et al., 2009). **(B)** In current models, augmin regulates centrosome independent microtubule nucleation by providing a link between the minus end of a new microtubule nucleated by the γ-TuRC, and the lattice of a pre-existing microtubule (adapted from Uehara et al., 2009).

3.2 Biochemical reconstitution of GFP-tagged augmin holo-complex and sub-complexes

The biochemical purification and characterization of the augmin holo-complex and sub-complexes was led by Kuo-Chiang Hsia, and in this section I will present published data that is relevant for the single-molecule microscopy studies I did, adapting from Hsia et al, 2014. Attempts to co-express all eight subunits of augmin in bacteria using polycistronic systems (Tan et al., 2005) were unsuccessful, so initial efforts focused on using this system to purify individual subunits and to generate sub-complexes. Full-length recombinant Hice1 could not be purified from a monodisperse peak in size exclusion chromatography, but a truncated construct consisting of the N-terminus microtubule binding region, Hice1-MTBR, could (Figure 3.2 A). Full-length Hice1 could be co-expressed with the hDgt6 N-terminal domain (hDgt6-NTD), and the dimer sub-complex was purified as a monodispersed peak (Figure 3.2 B). On examining which other augmin subunits would be co-purified with the dimer sub-complex, two stable tetrameric sub-complexes could be obtained. One of them (hereafter referred as the tetramer) was comprised of Hice1, hDgt6-NTD, UCHL5IP, and Cep27 (Figure 3.2 C). Using size exclusion chromatography coupled with in-line laser light scattering (SEC/LS; Folta-Stogniew and Williams, 1999) the molecular weights of the dimer and the tetramer were estimated, respectively, to be 91/95 and 149/162 (observed KDa/calculated KDa).

Complexes including all eight subunits of augmin could be expressed and purified from insect cells using the MultiBac system for poylcistronic gene

expression (Trowitzsch et al., 2010). An octameric complex including a hexahistidine tag on hDgt3, a GFP tag on Cep27, and a truncated version of hDgt6 could be purified using this strategy (hereafter referred as the octamer). The identity of all the bands obtained from the peak fraction of size exclusion separated by SDS-PAGE (Figure 3.2 D) was confirmed by mass spectrometry (data not shown; subunits detected: Hice1, hDgt6-NTD, UCHL5IP, GFP-Cep27, C14orf94, Ccdc5, hDgt5, and His-hDgt3). A complex containing all full-length subunits of human augmin, hereafter holo-complex, could be purified by replacing hDgt6-NTD with a GFP-tagged construct of full length hDgt6. The peak fraction of size exclusion chromatography yielded a band pattern after SDS-PAGE similar to that of the octamer, with one band displaced in a manner consistent with the subunit replacement (Figure 3.2 E). The holo-complex was purified with a low yield (~20 µg from 1 L of insect cell culture), and could only be used for characterization by single-molecule fluorescence microscopy.

The augmin sub-complexes that could be purified with high yields and Hice1-MTBR were assayed for microtubule co-sedimentation, with a gradient of tubulin concentration to determine binding affinity. The microtubule binding affinity of Hice1-MTBR was estimated to be 9.3 ± 1.4 µM (Figure 3.2 F). Assaying on a narrower range of tubulin concentrations, the affinities for the sub-complexes were 1.1 ± 0.2 µM for the octamer, 0.6 ± 0.1 µM for the tetramer, and 1.0 ± 0.1 µM for Hice1•hDgt6-NTD (Figure 3.2 G).

The octamer and holo-complex used in fluorescence microscopy assays were the ones described in this section. For Hice1-MTBR, Hice1•hDgt6-NTD,

and the tetramer, GFP-tagged versions were generated. For Hice1-MTBR, a GFP was included at the N-terminus of the peptide. For Hice1•hDgt6-NTD, the subunit hDgt6-NTD was replaced with GFP-hDgt6-NTD (GFP at the N-terminus). For the tetramer, two GFP-tagged variants were generated: a tetramer (GFP-Cep27; GFP at the N-terminus), replacing Cep27, and a tetramer (GFP-hDgt6-NTD; GFP at the N-terminus), replacing hDgt6-NTD.

Figure 3.2 Biochemistry of augmin sub-complexes and the holo-complex. **(A)** SDS-PAGE of sequential aliquots of the peak fraction of Hice1-MTBR's size exclusion chromatography. **(B)** SDS-PAGE of sequential aliquots of the peak fraction for Hice1•hDgt6-NTD. **(C)** SDS-PAGE of sequential aliquots of the peak fraction for the tetramer (Hice1, hDgt6-NTD, UCHL5IP, and Cep27). **(D)** SDS-PAGE of sequential aliquots of the peak fraction for the octamer (Hice1, hDgt6-NTD, UCHL5IP, GFP-Cep27, C14orf94, Ccdc5, hDgt5, and His-hDgt3). **(E)** SDS-PAGE for selected aliquots from size exclusion chromatography of the holo-complex (Hice1, GFP-hDgt6, UCHL5IP, GFP-Cep27, C14orf94, Ccdc5, hDgt5, and His-hDgt3). The rectangles in **(D)** and **(E)**, on the left, are an amplification of the lane with highest total band intensity. In **(A−E)**, the column 'Mr' shows molecular weights of the markers on the right in KDa. **(F)** Fraction of Hice1-MTBR bound to sedimented microtubules, at different tubulin concentrations. **(G)** Fraction of protein bound to sedimented microtubules, at different tubulin concentrations, for the octamer (black), the tetramer (blue), and Hice1•hDgt6-NTD (red). The curves in **(F)** and **(G)** are hyperbolic fits to each data set, with Kd values: 9.3 ± 1.4 μM for Hice1-MTBR, 1.1 ± 0.2 μM for the octamer, 0.6 ± 0.1 μM for the tetramer, and 1.0 ± 0.1 μM for Hice1•hDgt6-NTD. Adapted from Hsia et al, 2014.

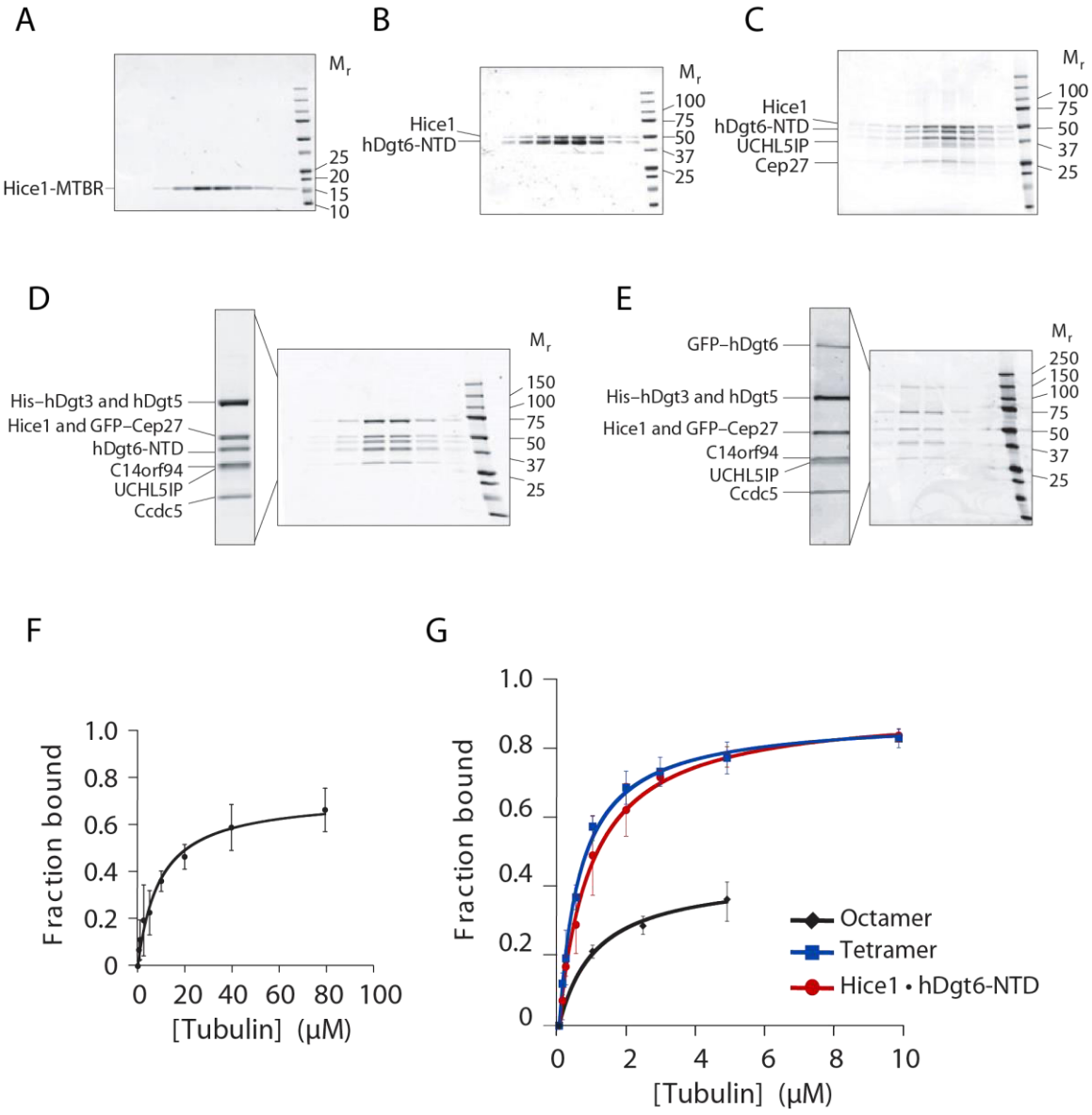
A
B
C
D
E
F
G
Hice1-MTBR
Hice1
hDgt6-NTD
UCHL5IP
Cep27
His–hDgt3 and hDgt5
Hice1 and GFP–Cep27
C14orf94
Ccdc5
GFP–hDgt6
Fraction bound
[Tubulin] (μM)
Octamer
Tetramer
Hice1 • hDgt6-NTD

3.3 Single spot intensity analyses of augmin holo-complex and sub-complexes

To study the purified complexes at a single-molecule level I used total internal reflection fluorescence (TIRF) microscopy. As an initial characterization, GFP-tagged proteins were diluted and flowed into microscope chambers made of non-functionalized glass, producing a sparse decoration of the coverslip surface after washing (Figure 3.3 A). GFP (as a monomeric construct) was used as a reference to estimate the fluorescence of a single fluorophore molecule. The images collected were analyzed to detect spots and quantify their intensity.

The quantification yielded a distribution of GFP spot intensities for each protein assayed. Expressing the mean ± standard deviation of the distribution in arbitrary units, the intensities resulted: GFP, 4800 ± 1700, with 577 spots analyzed (Figure 3.3 B); Hice1•GFP-hDgt6-NTD, 5400 ± 1800, with 593 spots analyzed (Figure 3.3 C); the tetramer tagged as GFP-Cep27, 4800 ± 1800, with 600 spots analyzed (Figure 3.3 D); the tetramer tagged as GFP-hDgt6-NTD, 5400 ± 2500, with 631 particles analyzed (Figure 3.3 E); the octamer, 4500 ± 2000, with 626 particles analyzed (Figure 3.3 F); and the holo-complex, 8300 ± 7000, with 662 particles analyzed (Figure 3.3 G).

Figure 3.3 GFP-tagged augmin complexes stuck to a glass surface and observed through TIRF microscopy. (A) Schematic of the assay. Diluted GFP-tagged augmin complexes, sparsely decorating the glass surface of microscope chambers, can be observed as single spots when exposed to TIRF illumination. **(B-G)** Selected fields (horizontal bar: 10 μm), were analyzed to detect fluorescence spots, quantify its intensity, and produce a distribution of spot intensities for **(B)** GFP, **(C)** Hice1•GFP-hDgt6-NTD, **(D)** the tetramer tagged as GFP-Cep27, **(E)** the tetramer tagged as GFP-hDgt6-NTD, **(F)** the octamer (GFP-Cep27), and **(G)** the holo-complex (GFP-Cep27 and GFP-hDgt6). The Bin Probability represents the portion of the spot intensity data that falls within the intensity values defined for a given bin of the histogram.

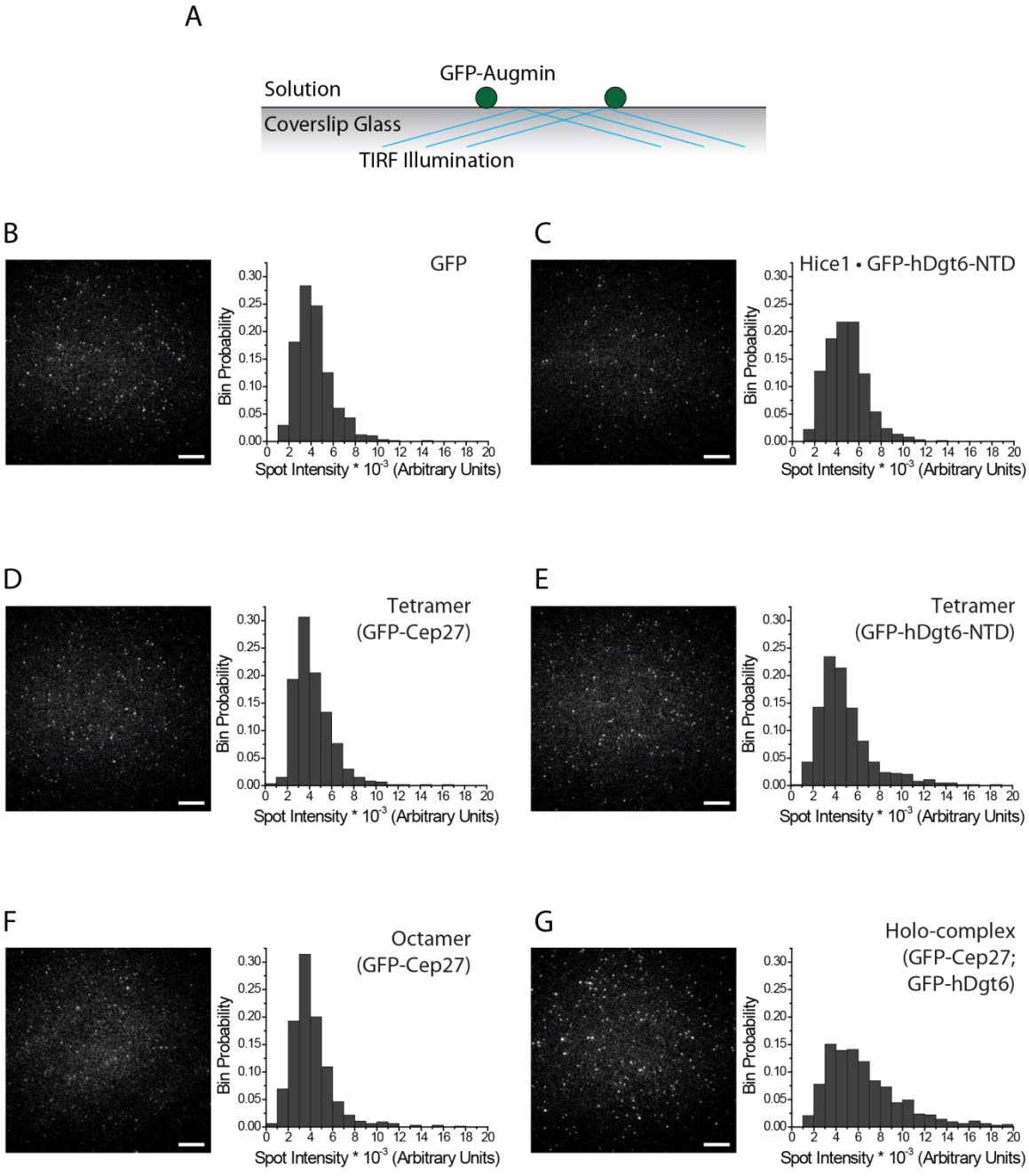
A
GFP-Augmin
Solution
Coverslip Glass
TIRF Illumination
B
GFP
C
Hice1 • GFP-hDgt6-NTD
D
Tetramer
(GFP-Cep27)
E
Tetramer
(GFP-hDgt6-NTD)
F
Octamer
(GFP-Cep27)
G
Holo-complex
(GFP-Cep27;
GFP-hDgt6)
Bin Probability
Spot Intensity * 10-3 (Arbitrary Units)

3.4 The augmin holo-complex and sub-complexes diffuse when bound to the microtubule lattice, and all but a dimeric sub-complex have a bimodal interaction time distribution

To study the interaction between microtubules and augmin I used a TIRF microscopy assay that incorporates GMP-CPP nucleated, taxol stabilized, biotinilated, and X-rhodamine labeled microtubules. Microtubules were immobilized, via avidin-biotin linkage, to a glass surface functionalized with biotin-polyethylene glycol (PEG), which also reduced non-specific surface protein binding (experimental details in Materials and Methods 2.3, and Bieling et al, 2010b). A solution with the same composition as the one from spot intensity quantification assays was used, supplemented with 1 nM of GFP-augmin (Figure 3.4.1 A).

Particles could be detected interacting with the entire length of the microtubule lattice, with GFP-spot diffusive incursions lasting a few frames of acquisition. Tracking of these spots allowed the quantification of dwell times and mean square displacements (MSD). The data pooled for each GFP-tagged augmin, sub-complex or holo-complex, analyzed allowed the determination of interaction lifetimes and diffusion coefficients (Figure 3.4.1 B−D, and Figure 3.4.2 A and B). A cumulative distribution function (CDF), was derived from the dwell times, and the CDF data was fit to the exponential sum, $1 - CDF(t) = A_1 e^{-t/\tau_1} + A_2 e^{-t/\tau_2}$, with the exception of the fit on the data from Hice1•GFP-hDgt6-NTD, for which A_2 and τ_2 were fixed to zero. The parameters extracted from the fits were: Hice1•GFP-hDgt6-NTD, τ_1 = 0.52 ± 0.02 seconds; tetramer (GFP-Cep27), τ_1 =

0.59 ± 0.05 seconds, τ_2 = 4.2 ± 0.2 seconds, A_2 = 0.099 ± 0.007; tetramer (GFP-hDgt6-NTD), τ_1 = 0.49 ± 0.03 seconds, τ_2 = 4.7 ± 0.3 seconds, A_2 = 0.041 ± 0.004; octamer, τ_1 = 0.77 ± 0.05 seconds, τ_2 = 13 ± 1 seconds, A_2 = 0.019 ± 0.002; holo-complex τ_1 = 0.30 ± 0.04 seconds, τ_2 = 3.2 ± 0.8 seconds, A_2 = 0.17 ± 0.01. This indicates that all of the complexes assayed have a majority of the population with dwell times below 1 second.

The MSD data paired with the time interval of displacements was fit to a line, MSD (t) = A + 2 * D * t, with D being the diffusion coefficient of the sample analyzed. The diffusion coefficients extracted from the displacement data were: Hice1•GFP-hDgt6-NTD, 0.16 ± 0.02 $\mu m^2/s$; tetramer (GFP-Cep27), 0.29 ± 0.01 $\mu m^2/s$; tetramer (GFP-hDgt6-NTD), 0.27 ± 0.01 $\mu m^2/s$; octamer 0.08 ± 0.01 $\mu m^2/s$; holo-complex, 0.16 ± 0.01 $\mu m^2/s$.

Figure 3.4.1 Single-molecule microscopy of microtubule-bound dimeric and tetrameric augmin sub-complexes. (A) Schematic of the assay. Functionalyzed glass (PEG coated) allows specific binding of X-rhodamine-labeled microtubules to the glass surface. GFP-tagged augmin complexes added to the solution can exchange between the solution and the microtubules and diffuse when bound to the polymer lattice. **(B-D)** (*left*) Selected microtubule images (horizontal bar 2 μm), maximum intensity projection of an associated GFP channel time lapse, and kymography (see section 2.7 for the definition of *kymograph*), on the main axis of the microtubule, of the GFP time lapse (horizontal bar: 2 μm; vertical bar: 10 seconds). A white rectangle marks areas of the kymograph, selected to show frame-by-frame (separated by a gray stripe) changes on intensity of the GFP signal, as shown magnified to the right of the kymograph (horizontal bar: 2 μm). (*center*) Cumulative distribution function (CDF), presented as 1 – CDF, of the dwell times of the tracks analyzed, with a fit to the function described in the main text as a red curve. (*right*) Mean square displacement of the tracks analyzed versus the time interval of displacement; a linear fit is presented in red, Y = A + 2*D*X, where D is the diffusion coefficient. Microtubule-bound data is presented for **(B)**, Hice1•GFP-hDgt6-NTD, **(C)**, tetramer tagged as GFP-Cep27, and **(D)** the tetramer tagged as GFP-hDgt6-NTD.

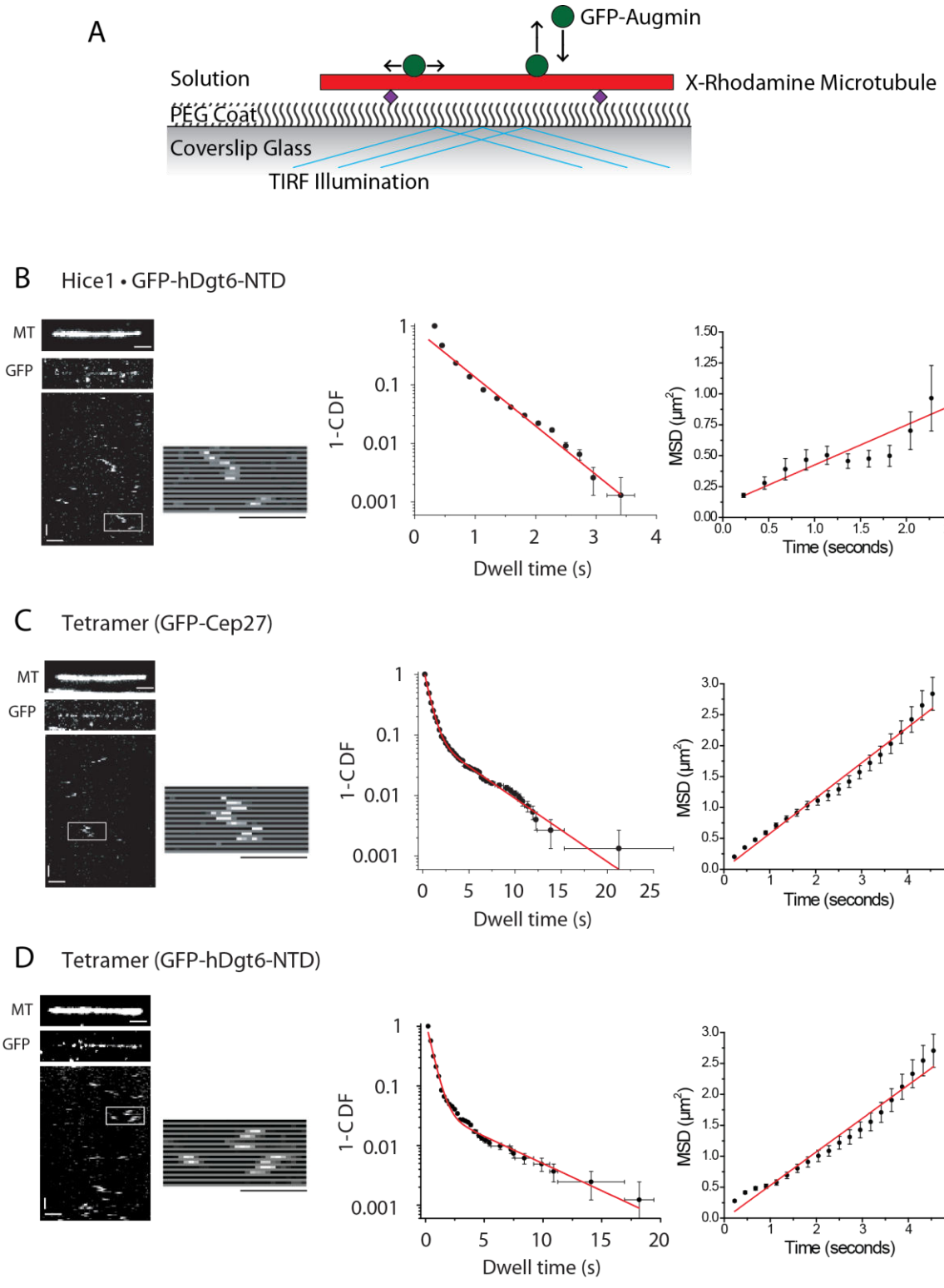
A
GFP-Augmin
Solution
X-Rhodamine Microtubule
PEG Coat
Coverslip Glass
TIRF Illumination
B
Hice1 • GFP-hDgt6-NTD
MT
GFP
1-C DF
Dwell time (s)
MSD (μm²)
Time (seconds)
C
Tetramer (GFP-Cep27)
MT
GFP
1-C DF
Dwell time (s)
MSD (μm²)
Time (seconds)
D
Tetramer (GFP-hDgt6-NTD)
MT
GFP
1-C DF
Dwell time (s)
MSD (μm²)
Time (seconds)

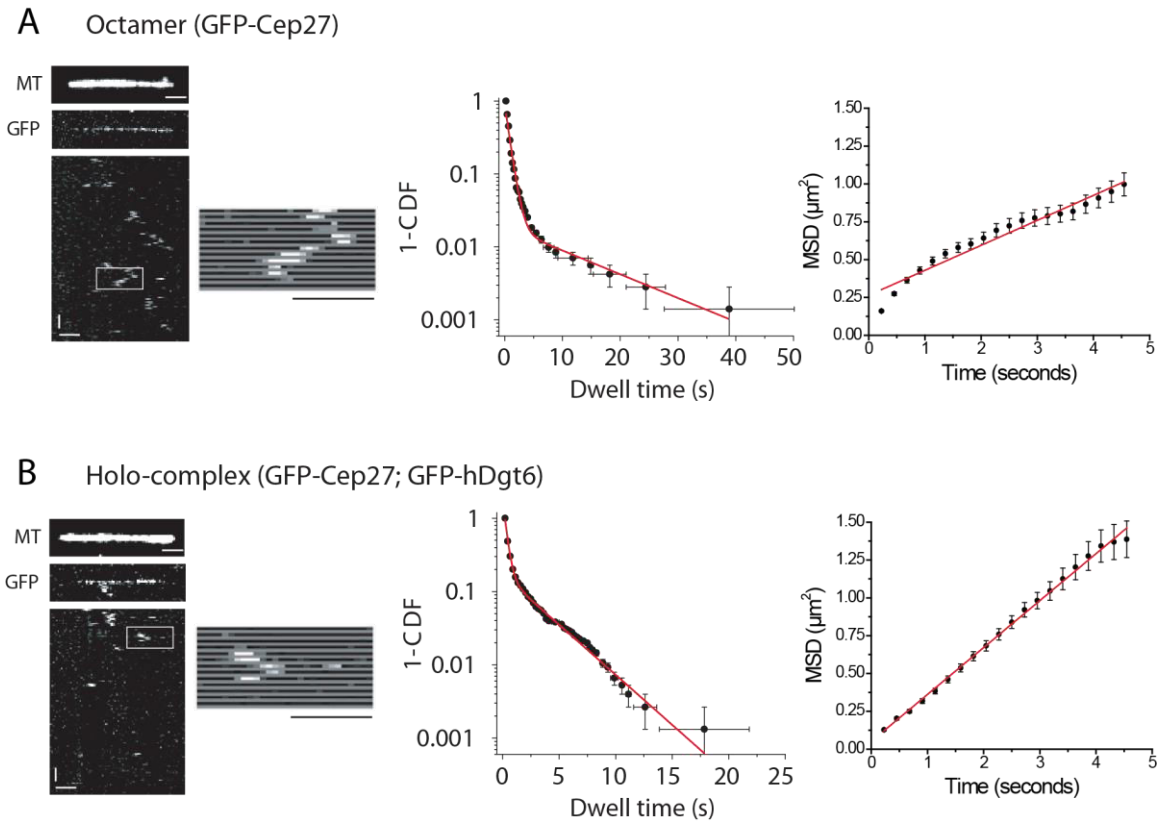

Figure 3.4.2 Single-molecule microscopy of microtubule-bound augmin octamer and holo-complex. (*left*) Selected microtubule images (horizontal bar 2 μm), maximum intensity projection of an associated GFP channel time lapse, and kymography, on the main axis of the microtubule, of the GFP time lapse (horizontal bar: 2 μm; vertical bar: 10 seconds). A white rectangle marks areas of the kymograph, selected to show frame-by-frame (separated by a gray stripe) changes on intensity of the GFP signal, as shown magnified to the right of the kymograph (horizontal bar: 2 μm). (*center*) Cumulative distribution function (CDF), presented as 1 – CDF, of the dwell times of the tracks analyzed, with a fit to the function described in the main text as a red curve. (*right*) Mean square displacement of the tracks analyzed versus the time interval of displacement; a

linear fit is presented in red, Y = A + 2*D*X, where D is the diffusion coefficient. Microtubule-bound data is presented for **(A)**, the octamer (GFP-Cep27), and **(B)**, the holo-complex (GFP-Cep27 and GFP-hDgt6).

3.5 Conclusion

The data presented in this Chapter provides a single-molecule microscopy characterization of recombinantly expressed, and purified, human augmin. In addition to the complex including all full length subunits –the holo-complex−, four other GFP-tagged sub-complexes were studied. These sub-complexes, and others not included in this Chapter, were also used in assays to gain insights on augmin's architecture and function (Hsia et al, 2014). However, the limited yield on the purification of the holo-complex only allowed for single-molecule microscopy assays to be performed. Thus, the data presented here is the first characterization of reconstituted human augmin to establish that the eight components of the complex are sufficient to form a stable complex that can interact with microtubules.

Under the conditions assayed, the samples analyzed produce spots with a distribution similar to that of monomeric GFP, used as a reference. The holo-complex presented a fraction of the spot population (less than 5% of the total population assayed) with intensity values an order of magnitude over the sample's mean intensity, and with spot sizes exceeding the threshold diameter used for the quantification (6 pixels, ~900 nm). Those spots were excluded from the intensity distribution shown in Figure 3.3 G. Apart from this outlier fraction of the holo-complex, the data from the sub-complexes analyzed suggests that augmin behaves as defined biochemically (that is, with each of the sub-complex bearing one GFP per molecule, and with the holo-complex bearing two GFPs per molecule), without aggregating into higher order structures.

The interaction of augmin with microtubules was observed to be short lived and diffusive. The diffusion coefficients extracted (0.08-0.29 $\mu m^2/s$) place augmin between the group of MCAK (0.38 $\mu m^2/s$; Helenius et al, 2006) and XMAP215 (0.3 $\mu m^2/s$; Brouhard et al, 2008), and the less diffusive group of kinesins like Kinesin-1 (0.036 $\mu m^2/s$; Lu et al, 2009) and Kinesin-5 (0.0008 $\mu m^2/s$; Kwok et al, 2006). Those kinesins have proposed functions as mechanical linkers between a microtubule, serving as a track, and a cargo. On the other hand, the high diffusivity of MCAK and XMAP215 was suggested to assist microtubule-end targeting via lattice diffusion. Consequently, models of augmin consistent with the diffusion observed should consider augmin not as a static linker, or anchor, between the lattice of a microtubule and a newly polymerized microtubule, but as a modestly diffusive linker.

Only one of the five augmin complexes assayed (Hice1•GFP-hDgt6-NTD) showed a mono-exponential dwell time distribution when interacting with microtubules. A simple interaction model between a receptor and a ligand produces the expected mono-exponential behavior. The observed, and unexpected, behavior of some of the augmin complexes has also been observed for the microtubule associated proteins Cin8 (Roostalu et al, 2011), and PRC1 (Bieling et al, 2010a), presented dwell time distributions with tails heavier than those expected from a mono-exponential. This suggests that the interaction between augmin and microtubules might be more complex than a two-state (bound/unbound) mechanism.

4. GFP-PRC1 cross-linking mechanics

4.1 Background information

During cell division, segregation of chromosomes takes place in anaphase A (Asbury, 2017), followed by an increase in the distance between spindle poles in anaphase B (Scholey et al, 2016). Kinetochore microtubules recede from the spindle body with chromosome movement, leaving non-kinetochore microtubules to experience forces from cortical force generators and/or motor proteins in the central spindle. Furthermore, the recruitment of proteins to the spindle midzone in anaphase is proposed to regulate cytokinesis (Gonzalez, 2003). Among the recruited proteins are MKLP1, INCENP (Zhu et al, 2005), CLASP1 (Liu et al, 2009), and PRC1 (Zhu et al, 2006). PRC1 (protein regulator of cytokinesis 1) is a non-motor microtubule associated protein, and it is a conserved protein in eukaryotes, having the orthologs Ase1 in *Schizosaccharomyces pombe* and MAP65 in *Arabidopsis thaliana*. It localizes in the nucleus in interphase, and during cell division it is dispersed throughout the spindle until anaphase onset, when it concentrates to a band of ~2 μm in the midzone until the end of cytokinesis.

PRC1 forms a homodimer (Subramanian et al, 2010). Its primary structure, from the N-terminus to the C-terminus, has the domains: dimerization, rod, spectrin, and a disordered base-rich domain which includes a nuclear localization signal (Figure 4.1 A). A construct excluding the disordered domain was crystalized (Figure 4.1 B; Subramanian et al, 2013), showing the dimerization and rod domains in a dimer in an extended configuration that separate the two spectrin domains of a homodimer by ~32 nm. Cryo-electron

tomography of microtubule mixed with PRC1 (lacking the disordered domain), produce filament bundles, with the filaments separated by a constant distance of ~30 nm, and presenting electron density in the inter-filament space. Both the spectrin and the disordered domains contribute to microtubule binding of PRC1. A construct made of the spectrin domain alone does not dimerize, and it has an affinity of 3.3 ± 1.8 μM for microtubules. Moreover, a construct with the spectrin and the base-rich disordered domains (also a monomeric), has an affinity of 0.6 ± 0.3 μM.

Experiments driving a single monomeric PRC1 molecule (using a construct with the spectrin and disordered domains), on the main axis of a microtubule, using an optical trap, show that PRC1 can generate a frictional force opposing motion (Forth et al, 2014). This frictional force scales with the velocity of motion (Figure 4.1 C), in a manner that can be explained by a model where friction arises from the diffusional interaction between PRC1 and microtubules. The motor protein Kineisn-5's microtubule-microtubule relative sliding speed is slowed down in the presence of GFP-PRC1 (Subramanian et al, 2010). The average sliding speed is reduced with increasing GFP-PRC1 concentration. Notably, the sliding velocity remains constant as the overlap length between microtubules decreases, and no strong change in GFP-PRC1's decoration density is observed (Figure 4.1 D). On the other hand, PRC1's ortholog, Ase1, shows an increase in decoration density and a slowdown in the sliding velocity as the overlap length decreases, when motility is driven by Kinesin-14 (Figure 4.1 E; Braun et al, 2011). Moreover, microtubule pairs cross-linked by Ase-GFP1 can

produce a force opposing overlap reduction by an optical trap, which scales with the inverse of the overlap length (Figure 4.1 F; Lansky et al, 2015), while conserving the fluorescence intensity of Ase1-GFP. Furthermore, in Bieling et al, 2010a, the authors show that the diffusivity of PRC1 decreases with increasing decoration density (Figure 4.1 G), suggesting the possibility of modulating PRC1's frictional force by changing the decoration density in the overlap of two cross-linked microtubules.

Figure 4.1 PRC1 is a diffusible cross-linker of microtubules. **(A)** Domain organization of PRC1. A nuclear localization signal (NLS) extends in the amino acid interval 470-488. **(B)** Structural model of the PRC1 dimer. (Adapted from Subramanian et al, 2013). **(C)** Force-velocity curve for a GFP-PRC1 monomer construct driven on a microtubule with optical tweezers. (Adapted from Forth et al, 2014). **(D)** Kymographs showing Kinesin-5 (Eg5) sliding GFP-PRC1 (bottom panel) decorated microtubules (X-rhodamine labeled; top panel). The scale bars are 1.5 μm horizontally and 100 seconds vertically. (Adapted from Subramanian et al, 2010). **(E)** Kymographs showing Kinesin-14 (Ncd) sliding Ase1-GFP (central panel) decorated microtubules (rhodamine labeled; left panel). The right panel is a composite image of both channels. (Adapted from Braun et al, 2011). **(F)** Force recorded at several overlap lengths, set with optical tweezers, on bundles decorated with Ase1-GFP. The inset shows the force dependence on GFP intensity at a set overlap length of ~1 μm. (Adapted from Lansky et al, 2015). **(G)** Mean square displacement of Alexa-488-PRC1 bound to microtubule bundles, over time. Black scatter includes traces with no added unlabeled PRC1, blue scatter has additional unlabeled PRC1, and red scatter includes Alexa-488-PRC1 trajectories that were deemed stuck to the surface. Fitting MSD = 2*D*t + offset on the sparse (black scatter) and dense decoration (blue scatter) yielded the diffusivities (D): D_{sparse} = 10900 ± 700 nm^2/s and D_{dense} = 2900 ± 200 nm^2/s. (Adapted from Bieling et al, 2010a).

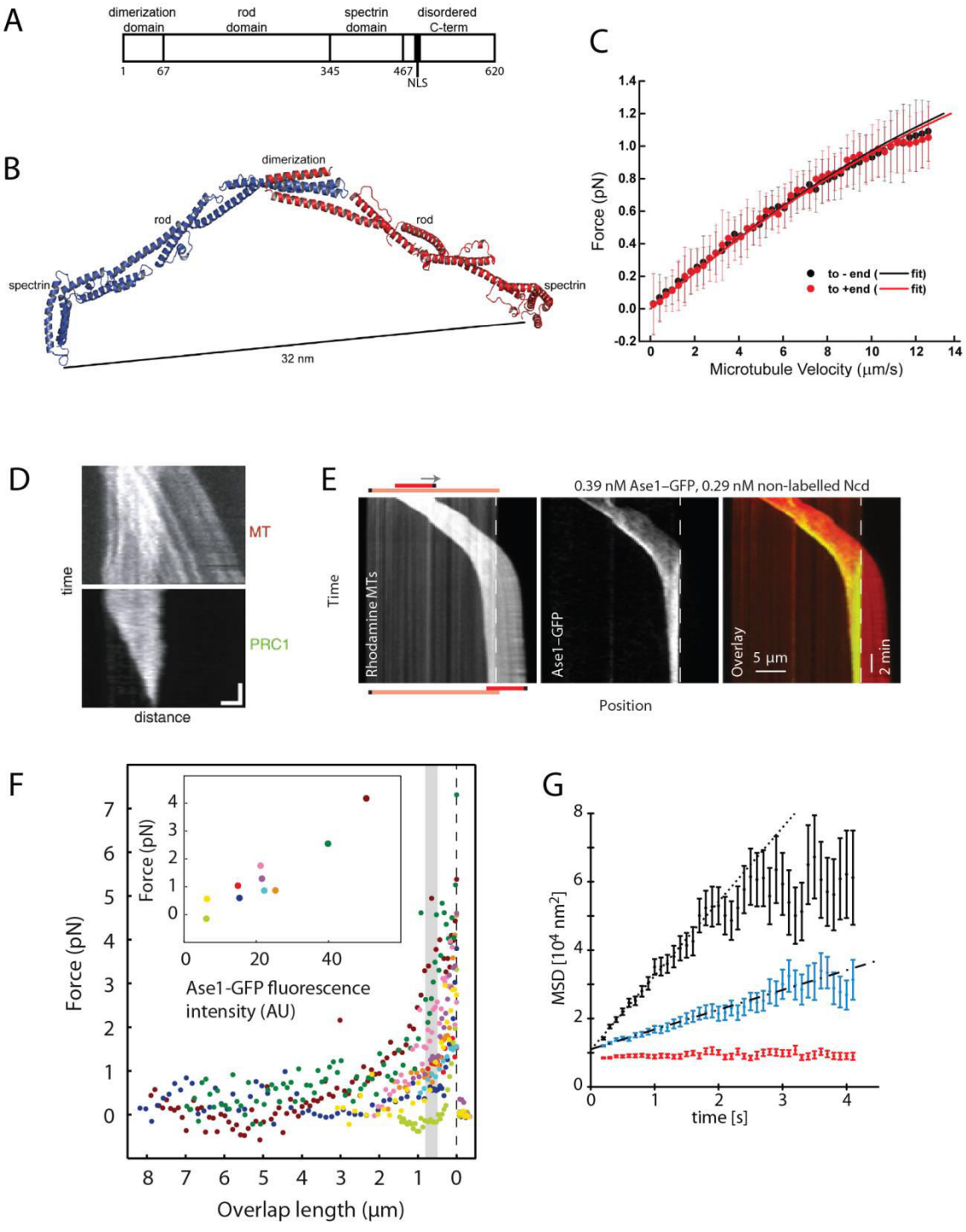
A
dimerization domain
rod domain
spectrin domain
disordered C-term
1
67
345
467
NLS
620
B
dimerization
rod
rod
spectrin
spectrin
32 nm
C
Force (pN)
Microtubule Velocity (µm/s)
to - end (fit)
to +end (fit)
D
time
MT
PRC1
distance
E
0.39 nM Ase1–GFP, 0.29 nM non-labelled Ncd
Time
Rhodamine MTs
Ase1–GFP
Overlay
5 µm
2 min
Position
F
Force (pN)
Ase1-GFP fluorescence intensity (AU)
Overlap length (µm)
G
MSD [10^4 nm^2]
time [s]

4.2 Characterization of the GFP-PRC1 construct used

The construct of GFP-PRC1 used in these studies was obtained as described (Subramanian et al, 2010; details in Materials and Methods). The GFP was included at the N-terminus of PRC1, with a triple alanine spacer (Figure 4.1 A). The protein was expressed in bacteria and purified with affinity chromatography. Further purification was done with size exclusion chromatography, and then the peak fractions were pooled, yielding protein ~80% pure (Figure 4.2 B). The lower molecular weight band seen on Figure 4.2 B is not detectable in a truncated construct lacking the basic C-terminus domain of PRC1 (PRC1 [1-486]; Subramanian et al, 2010, on supplementary figure 1).

The purified protein was characterized by total internal reflection fluorescence (TIRF) microscopy, by recording the intensity of single GFP spots stuck on the microscope coverslip's surface, and by tracking microtubule bound GFP-PRC1. Intensity measurements were done on non-functionalized glass microscope chambers, sparsely decorated with GFP-PRC1 such that spots would be separated by ~1 μm or more (Figure 4.2 C). Fluorescence spots five standard deviations above the mean intensity of the image field were selected to extract the sum of the spot intensity over background. The intensities of the spots analyzed were pooled together, and histograms of the intensities were assembled. The process was repeated for GFP-Eg5-FL (GFP-tagged, full length construct of Kinesin-5, reported a tetramer; Kashina et al., 1996) and a truncation of Eg5, GFP-Eg5-513, reported a dimer (Valentine et al, 2006). Expressing the mean ± standard deviation of the distribution in arbitrary units, the intensities

resulted: GFP-Eg5-FL, 8090 ± 3060, with 148 spots analyzed (Figure 4.2 D, *top*); GFP-PRC1, 4020 ± 1300, with 110 spots analyzed (Figure 4.2 D, *center*); GFP-Eg5-513, 4130 ± 1220, with 106 spots analyzed (Figure 4.2 D, *bottom*).

Microtubule binding properties of GFP-PRC1 were assessed with a TIRF microscopy assay attaching microtubules, labeled with biotin and X-rhodamine, to the microscope chamber's glass coated with methoxy-PEG and biotin-PEG, via Avidin biochemistry. After flowing in GFP-PRC1 to the chamber in a low salt solution (BRB80 with no additional salt), a single snap on the X-rhodamine channel and a time-lapse on the GFP channel were acquired. GFP spots diffused on the surface where microtubules are observed (Figure 4.2 E). Spots were tracked using Speckle TrackerJ (Smith et al, 2011). Mean squared displacements for 38 tracks were computed, and plotted versus the displacement time interval (Figure 4.2 F). A line was fit to the plot, estimating the diffusivity of GFP-PRC1 to be 45000 ± 2000 nm^2/s.

Figure 4.2 GFP-PRC1 forms a dimer that diffuses on microtubules. **(A)** Schematic of the construct GFP-PRC1 purified. The GFP introduced at the N-terminus of PRC1 is highlighted in gray and the amino acids in the transition between domains (rod and dimerization, spectrin, and disordered) are marked. **(B)** SDS-PAGE of peak fractions of size exclusion chromatography. The gray bar on the top covers the fractions pooled that were used in further studies. **(C)** Image of GFP channel on the coverslip surface after exposition to a solution containing GFP-PRC1. Horizontal bar is 10 μm. **(D)** Intensity distribution for spots detected for surfaces coated with Eg5-FL-GFP (*top*), GFP-PRC1 (*center*), and Eg5-513-GFP (*bottom*). **(E)** Imaging of GFP-PRC1 bound to X-rhodamine labeled microtubules. (*Top*), composite image of a single microtubule sparsely decorated by GFP-PRC1. (*Bottom*), kymograph of the composite from the microtubule image and the GFP time lapse taken, made on the microtubule's main axis. Horizontal bar, 2 μm (applies to top and bottom); vertical bar, 10 seconds. **(F)** Mean Square Displacement versus Time Interval for microtubule-bound GFP-PRC1 tracks (38 tracks assembled). Vertical bars are standard error of the mean. Solid line is a linear fit to the data, MSD (t) = Intercept + 2*D*time, where D is the diffusivity of GFP-PRC1.

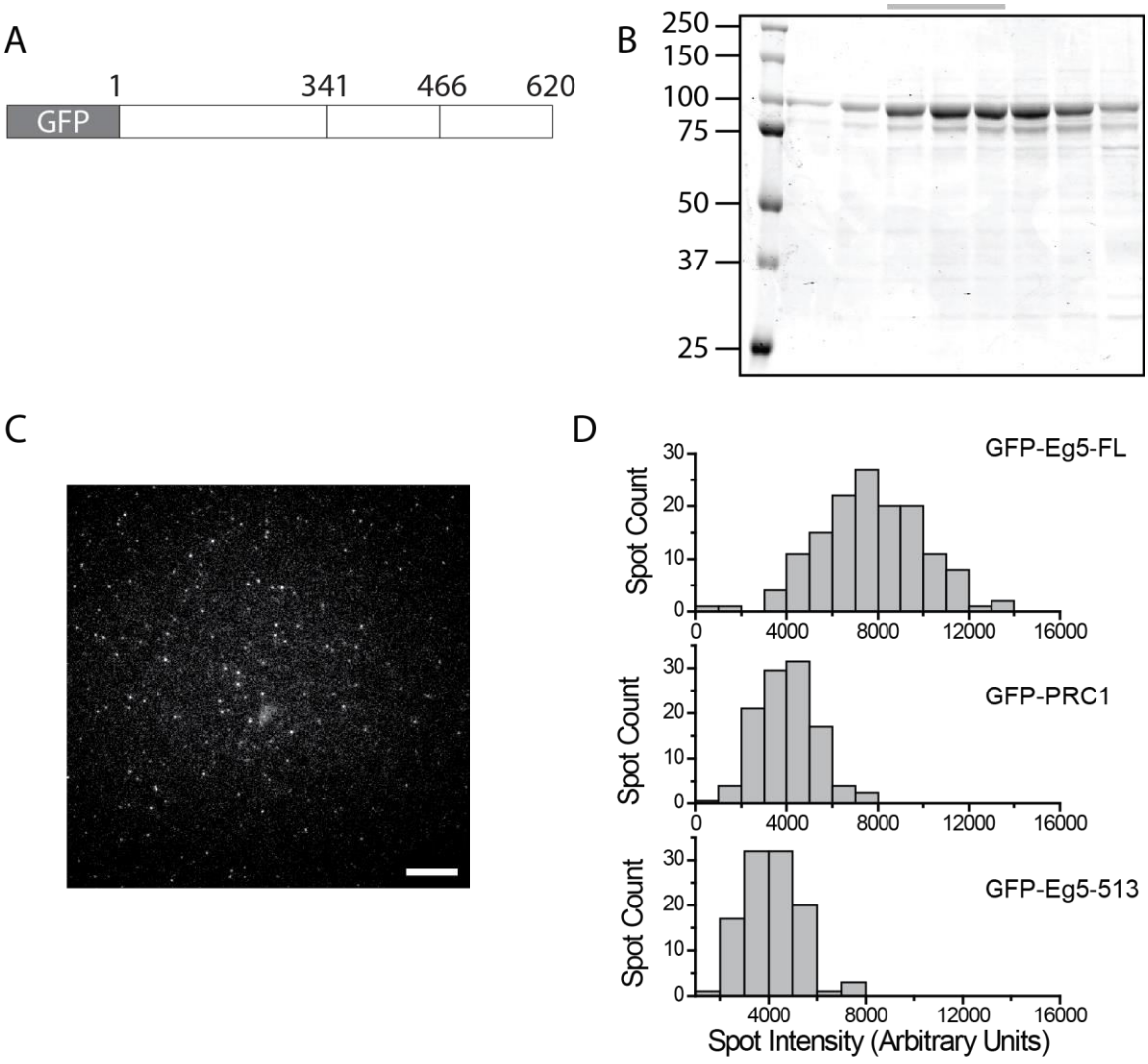
A
1
341
466
620
GFP
B
250
150
100
75
50
37
25
C
D
GFP-Eg5-FL
GFP-PRC1
GFP-Eg5-513
Spot Count
Spot Intensity (Arbitrary Units)
E
F
Mean Square Displacement (μm²)
Time Interval (s)

4.3 GFP-PRC1 gets enriched to microtubule bundles with a preference to an antiparallel alignment of microtubules

GFP-PRC1 was used to assemble bundles of microtubules following a sequential treatment of microscope chambers (Figure 4.3 A). First, biotin-PEG coated glass was exposed to Avidin, and then biotin-labeled microtubules (also labeled with X-rhodamine at a low concentration). Surface immobilized microtubules were then decorated at an above-single-molecule density of GFP-PRC1, exposing the filaments to 0.2 nM GFP-PRC1 in a solution containing BRB80 with no additional salt. Then, non-biotin microtubules (brightly labeled with a high concentration of X-rhodamine) were flowed with more GFP-PRC1 and incubated for 15 minutes. Finally, the solution was exchanged to a lower GFP-PRC1 concentration (0.05 nM), and a higher salt concentration (BRB80 with 80 mM additional potassium chloride).

After this treatment, the microscope chamber was imaged. Single microtubules, with dim X-rhodamine intensity, could be seen decorating the surface, with low levels of GFP signal bound to them (Figure 4.3 B). Occasionally, a brightly labeled microtubule would be found bound to the surface, with part of its extension co-localizing with a dense decoration of GFP signal, and sometimes a dim microtubule would extend from the region of co-localization in the opposite direction of the bright microtubule. The difference of brightness between the two types of microtubules is about 4-fold, and any other level of GFP decoration is barely distinguishable from the background, with the exception of the area where a microtubule bundle is defined to exist (Figure 4.3 C).

The assembly of bundles was repeated, but using un-tagged PRC1 and polarity marked microtubules, having brighter minus-ends and dimmer plus-ends. Biotin-labeled microtubules were polymerized with X-rhodamine-labeled tubulin and microtubules without biotin were polymerized with Alexa-488-labeled tubulin (Figure 4.3 D). Images taken on both the X-rhodamine and Alexa-488 channels were analyzed, isolating instances were Alexa-488 filaments were aligned and overlapped with X-rhodamine filaments. Of 56 filament pairs isolated, 40 were assigned as antiparallel (71 %; plus-ends on opposite sides of the bundle), and 16 as parallel (29 %; plus-ends on the same side of the bundle). Figure 4.3 E shows an example of anti-parallel and parallel bundles.

Figure 4.3 Visualizing microtubule bundles cross-linked by GFP-PRC1. **(A)** Schematic of a microtubule bundle visualized by TIRF microscopy. The purple rhomboid represents Avidin-biotin links between the dim microtubule and the PEG-coated surface. **(B)** Images of a selected bundle and single microtubule for the GFP channel, X-rhodamine channel, and the composite image. In the bottom there is a length ruler, in micrometers. **(C)** Line scans on the bundle and single microtubules images from panel B, for the X-rhodamine (red), and GFP (green) channels. **(D)** Schematic of a polarity marked microtubule bundle visualized by TIRF microscopy. The biotin-labeled microtubule, attached to the surface, has a minus-end segment labeled with a higher concentration of X-rhodamine (red), relative to the plus-end segment (pink). The microtubule without biotin has a minus end segment labeled with a higher concentration of Alexa-488 (green), relative to the plus-end segment (light green). In this experiment PRC1 is not labeled with a fluorescent tag. **(E)** Images of selected bundles with anti-parallel (*left*), and parallel configurations (*right*), for the X-rhodamine channel, the Alexa-488 channel, and the composite image. Horizontal bar in the bottom is 10 μm.

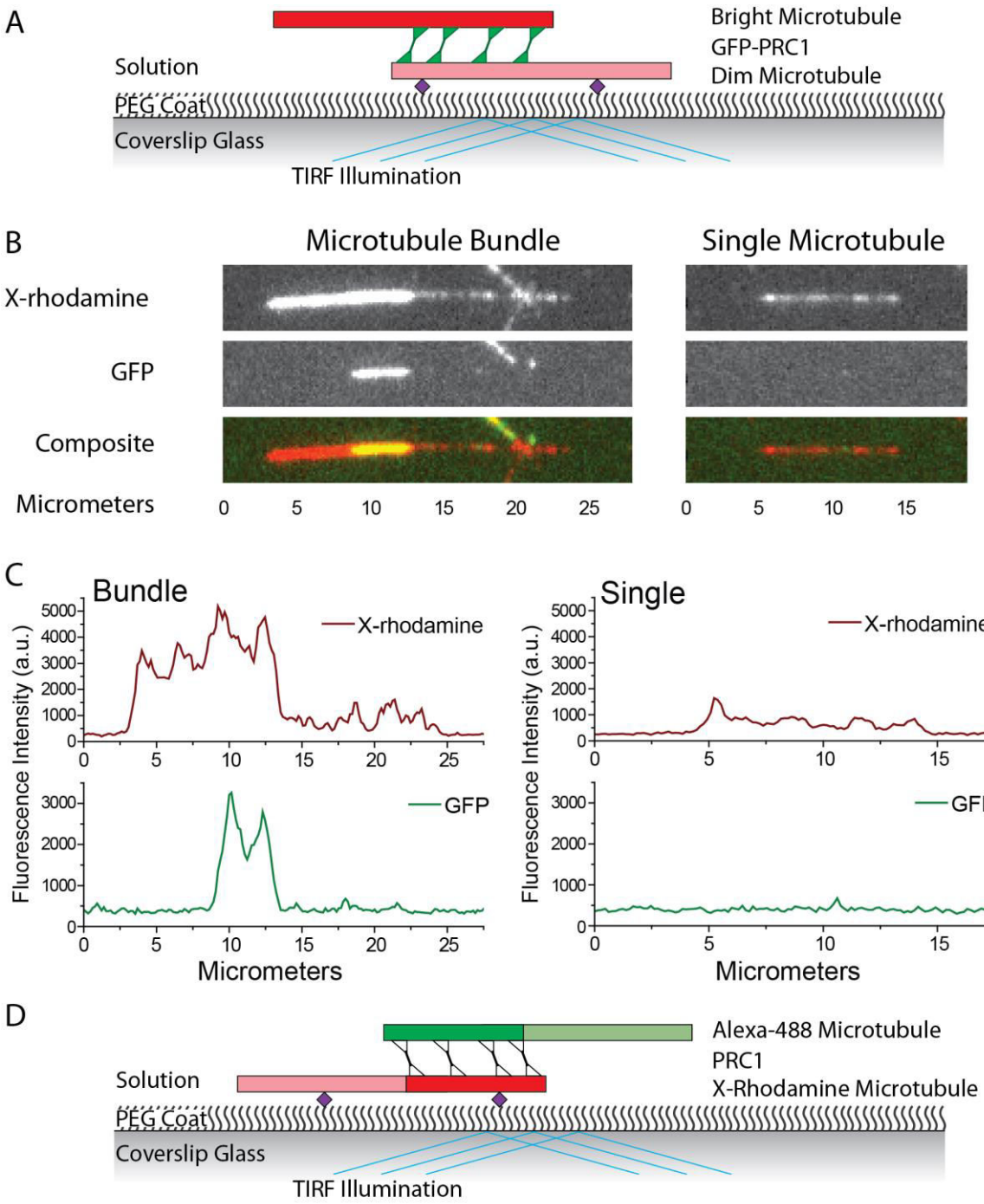
A
Bright Microtubule
GFP-PRC1
Dim Microtubule
Solution
PEG Coat
Coverslip Glass
TIRF Illumination
B
Microtubule Bundle
Single Microtubule
X-rhodamine
GFP
Composite
Micrometers
0 5 10 15 20 25
0 5 10 15
C
Bundle
Single
X-rhodamine
GFP
Fluorescence Intensity (a.u.)
Micrometers
D
Alexa-488 Microtubule
PRC1
X-Rhodamine Microtubule
Solution
PEG Coat
Coverslip Glass
TIRF Illumination
E
Anti-Parallel
Parallel
X-rhodamine
Alexa-488
Composite

4.4 GFP-PRC1 binds to bundles with a given microtubule alignment but not the inverse, and with an exchange rate of hundreds of seconds

Microtubule bundles were assembled as described in the previous section, with the difference that coated beads were included in the last solution flowed into the microscope chamber. The beads were coated following a published protocol (Shimamoto et al, 2015; detailed in Materials and Methods), making them sticky to microtubules and able to withstand forces of decades of piconewtons without detaching. Once a bundle was found, a single bead was trapped and brought to the bundle. Attachment between the bundle and the bead was set on the bright microtubule 1-2 μm away from the region with GFP signal and 1-2 μm away of the edge (Figure 4.4 A). Typically, the attachment led to a reduction in fluorescence intensity of the bright microtubule in the region where the bead was seen (Figure 4.4 B). Moving the stage position also produced changes in the bright microtubule's signal position and shape, tracking the motion of the bead.

Once a durable attachment was established, the stage was moved to strip apart the two microtubules of the bundle. While moving, the bright microtubule was slowly pivoted on the dim microtubule to invert the direction of the bright microtubule (Figure 4.4 C and F). When pivoting was not possible, the stage was moved rapidly to produce an inversion in the direction of the bright microtubule. After inverting the orientation of the bundle, a time-lapse on the red and green channels was acquired to follow the behavior of the microtubules and the GFP signal (Figure 4.4 D). The bead was released from the trap after a few frames of

acquisition to maximize the chances of attachment between the bright and dim microtubules. The region where the bundle was assembled initially showed a marked reduction in the GFP signal, suggesting that most of GFP-PRC1 had dissipated into the solution after stripping the bundle. Quantification of the inverted bundle's GFP signal during the time-lapse showed no evident increase in the intensity (Figure 4.4 E).

The bead was trapped again, and the stage moved to strip the bundle and invert the bright microtubule's direction (Figure 4.4 F). The bundle's original orientation was restored, and a time-lapse on the red and green channels was acquired again (Figure 4.4 G). During this second time-lapse an increase of GFP decoration was seen, with an apparent saturation of the signal's intensity at after a few minutes of restoring the bundle (Figure 4.4 H).

Ten bundles were manipulated as it is described in this section. After data acquisition, the GFP signal density of the bundle on every frame was measured. For each frame, the measured density was divided by the initial GFP signal density of the bundle, before manipulation, and then the resulting value was averaged across all the bundles. This process was done for the first and the second time-lapses separately, producing two data series of GFP signal density, divided by initial, over time (Figure 4.4 I). The series for the first time-lapse, after inverting the bundle's orientation to the opposite of the initial orientation, showed virtually no change in the GFP signal. On the other hand, after the second inversion of the bundle's orientation, restoring the original filaments' orientation, the GFP signal grew steadily, and showed a tendency to saturation to a density

level below the initially measured. The second time-lapse was fit to an exponential decay ($\mathrm{Y(t) = A - Be^{-t/C}}$), with a characteristic time (C), of 280 ± 10 seconds (A = 0.49 ± 0.01; B = 0.41 ± 0.01).

Considering a binding model for which GFP-PRC1 molecules crosslinking microtubules bind discrete sites in a microtubule bundle, and based on descriptions from Hill and Langmuir, a binding process can involve a homo-dimer of GFP-PRC1 (P) in a volume of diffusive media that can bind an available site (S) to produce an occupied site (N). In turn, a particle can unbind from an occupied site and produce an available site. The two sub-processes can be presented schematically as two steps:

Binding: $\mathrm{P + S \rightarrow N}$

Unbinding: $\mathrm{N \rightarrow P + S}$

Assuming non-cooperative binding, that is the rates of the steps are not dependent on whether or not other particles are already bound, then the sub-processes can be considered elementary steps with the following rate laws:

Binding: $\mathrm{r_b = k_b\, P\, S}$

Unbinding: $\mathrm{r_u = k_u\, N}$

In these laws r are rates, k are rate constants and *P* is the concentration of the particle in the diffusive media, *S* and *N* are counts of available sites and occupied sites, respectively. If S and N are restricted to a surface or to one dimension, then P is considered constant as there is a large reservoir of particles in the diffusive media.

Then, the rate of appearance/disappearance of occupied sites can be written as the rate of binding minus the rate of unbinding:

$$\dot{N} = k_b\ P\ S - k_u\ N$$

$\dot{N}$ is the partial derivative of the count of occupied sites over time. Consider the total number of sites, $S_T = S + N$; if all the sites are distributed in a line regularly separated by a distance Δx, then $S_T = L/\Delta x$, where L is the bundle length. Rearranging the equation and introducing an initial condition for the count of occupied sites produces the initial value problem (IVP):

$$\begin{cases} \dot{N} = k_b\ P\ L/\Delta x - (k_b\ P + k_u)\ N \\ N(t = 0) = 0 \end{cases} \qquad \text{(IVP 1)}$$

for which a solution exists and it is unique:

$$N(t) = N_{eq}\ [1 - e^{-(k_b P + k_u)t}] \qquad \text{(Equation 1)}$$

where,

$$N_{eq} = \frac{k_b\ P\ L}{(k_b\ P + k_u)\ \Delta x}$$

The fit done on the second time-lapse of Figure 4.4 I yielded a characteristic time, which can be related to the parameter: $C = (k_b P + k_u)^{-1}$. This parameter will be referred hereafter as the characteristic exchange time of the bundle.

Figure 4.4 Manipulation of microtubules with optical tweezers, to change bundle orientation. **(A)** Schematic of a bundle with a trapped bead attached to the microtubule brightly labeled with X-rhodamine. **(B)** Images of a selected trapped bundle for the X-rhodamine, GFP, and transillumination channels, and composite of all the channels (from top to bottom, respectively). The bar in the bottom is 10 μm. **(C)** Montage of the X-rhodamine channel time-lapse acquisition, with diagrams on the right depicting the expected positions of the bright microtubule (red), dim microtubule (pink), and the trapped bead (circle), when flipping the bundle's orientation. The yellow cross marks the estimated position of the trapped bead. The bar in the bottom is 10 μm. **(D)** Montage of the composite of the X-rhodamine (red) and the GFP (green) channels, during the time-lapse acquired after the bundle was inverted to oppose the original orientation. On the left of the montage is the time elapsed since the beginning of the time-lapse. The bar in the bottom is 10 μm. **(E)** Quantification of the GFP intensity during the time-lapse acquired after inverting the bundle orientation. **(F)** Montage of the X-rhodamine channel time-lapse acquisition, with diagrams on the right depicting the expected positions of the bright microtubule (red), dim microtubule (pink), and the trapped bead (circle), when restoring the bundle's orientation to the original orientation. The yellow cross marks the estimated position of the trapped bead. The bar in the bottom is 10 μm. **(G)** Montage of the composite of the X-rhodamine (red) and the GFP (green) channels, during the time-lapse acquired after the bundle was restored to the original orientation. On the left of the montage is the time elapsed since the beginning of the time-lapse. The bar in the

bottom is 10 μm. **(H)** Quantification of the GFP intensity during the time-lapse acquired after restoring the bundle to its original orientation. **(I)** Time series of GFP signal density divided by the initial density (before manipulation), averaged for ten manipulated bundles, for the first time-lapse acquired after the inversion of orientation (white-filled circles), and for the second time-lapse acquired after restoring the original orientation of the bundle (black circles). The grey bars are the standard error of the mean. The red curve is a fit to the function $\mathrm{Y(t)} = \mathrm{A} - \mathrm{Be}^{-\mathrm{t/C}}$, done on the second time-lapse series.

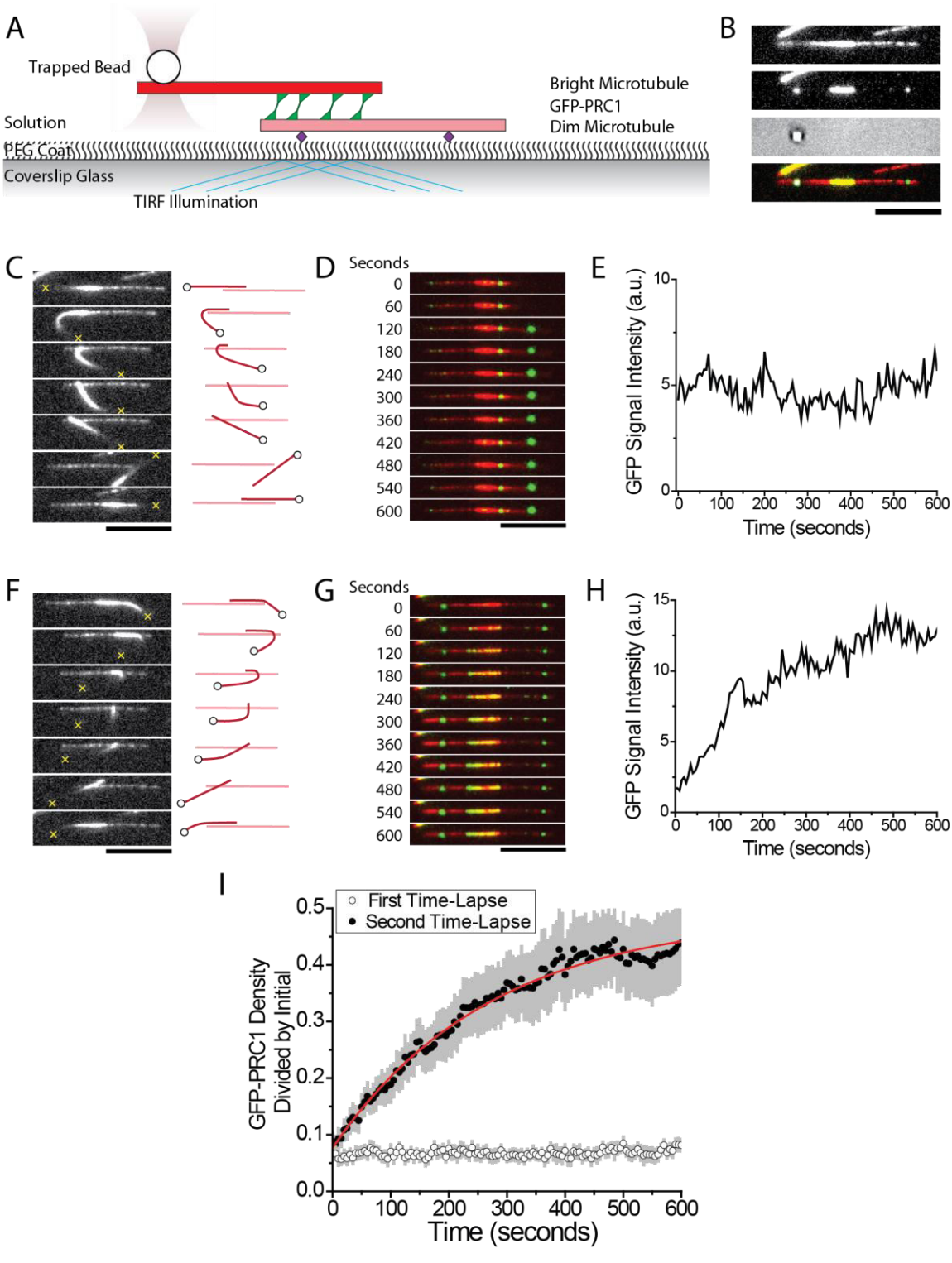
A
Trapped Bead
Solution
PEG Coat
Coverslip Glass
TIRF Illumination
Bright Microtubule
GFP-PRC1
Dim Microtubule
B
C
D
Seconds
0
60
120
180
240
300
360
420
480
540
600
E
GFP Signal Intensity (a.u.)
Time (seconds)
F
G
Seconds
H
GFP Signal Intensity (a.u.)
Time (seconds)
I
First Time-Lapse
Second Time-Lapse
GFP-PRC1 Density
Divided by Initial
Time (seconds)

4.5 Driven sliding of bundles at constant velocity shows GFP-PRC1 accumulation

Microtubule bundles were assembled and attached to trapped beads as described in the previous section. The stage was moved to drive the microtubules of the bundle to slide apart (Figure 4.5 A). Images on the X-rhodamine, GFP, and transillumination channels were collected for each trapped bundle (Figure 4.5 B). The GFP channel image was used to estimate the orientation angle of the bundle relative to the stage coordinates. Then, a custom-written software routine was used to move stage at a constant velocity in the direction of the main axis of the bundle. While moving the stage, a time-lapse on the GFP channel was acquired, recording the time intervals when the camera was acquiring. The routine also recorded the position of the stage as it moved, and the position of the bead estimated from the trapping beam focused on a photodiode quadrant detector downstream from the focal point.

A successful pulling event was defined when the GFP signal length decreased as the stage moved until the signal disappeared (Figure 4.5 C). Acquiring images on the GFP, X-rhodamine, and transillumination channels show that after the stage movement the dimly labeled microtubule remains with a negligible level of GFP signal above background (Figure 4.5 D). Using the recorded time intervals when the camera was acquiring, it was possible to synchronize the time of the microscope's acquisition to the time of the stage position data and bead position data. This synchronization revealed that the bead position changed quickly when the GFP signal decayed significantly, but full

dissipation of GFP signal had not been observed yet (Figure 4.5 E). The dissipation of the entire GFP signal occurred several seconds after the bead's yank. Additionally, after the yank, the GFP signal explored a larger area, in the axis of the bundle. The change in bead position was generally faster than the routine's acquisition rate (100 Hz), and it could be observed in all successful pulling events. The time-point of acquisition before the position change was defined as the rupture point of the bundle.

Quantification of GFP signal intensity over time lapse showed that the signal decreased as the signal length decreased, but it did so more steeply closer to the rupture point (Figure 4.5 F). The GFP signal was superimposed with a segment of the expected length assuming that before the rupture point the change of length equaled the stage velocity (Figure 4.5 G). The frames for which the GFP signal and segment length had the same trend were considered as being in a sliding regime, and were kept for further analyses.

The GFP signal intensity divided initial GFP signal intensity event (N/N_0) was plotted versus expected bundle length divided initial expected bundle length (L/L_0; Figure 4.5 H), for all frames in the sliding regime, of all pulling events collected, binning N/N_0 over L/L_0 intervals. In the resulting plot, the intensity decreased as length decreased, approaching a value above zero as the length decreased. The paired data ($\mathrm{X} = \mathrm{L}/\mathrm{L}_0$, $\mathrm{Y} = \mathrm{N}/\mathrm{N}_0$) was fit to two functions: the first one, $\mathrm{Y}\,(\mathrm{X}) = \mathrm{X} + \mathrm{A} - \mathrm{A} * \mathrm{e}^{(\mathrm{X}-1)/\mathrm{A}}$, which yielded A = 2.1 ± 0.6; and a second one including an offset, $\mathrm{Y}\,(\mathrm{X}) = \mathrm{X} + \mathrm{A} - \mathrm{A} * \mathrm{e}^{(\mathrm{X}-1)/\mathrm{A}} + \mathrm{B}$, which yielded A = 0.87 ± 0.13 and B = 0.13 ± 0.02. The curve of the second fit is shown in Figure 4.5 H.

The binding model presented on section 4.3 can be adapted to a bundle where binding sites are removed at a constant rate. During driven sliding at a constant velocity, the binding sites' count scales with the bundle length ($S_T = L/\Delta x$), and the bundle length evolves over time following:

$$L = L_0 - v_{STAGE}\, t$$

where L_0 is the initial bundle length, and v_{STAGE} is the stage velocity.

The initial value problem from section 4.3 (IVP 1), can be re-written to include a receding length and a set number of starting molecules:

$$\begin{cases} \dot{N} = k_b\, P\, (L_0 - v_{STAGE}\, t)/\Delta x - (k_b\, P + k_u)\, N \\ N(t = 0) = N_{eq} = \dfrac{k_b\, P\, L_0}{(k_b\, P + k_u)\, \Delta x} \end{cases} \qquad \text{(IVP 2)}$$

For this initial value problem a solution exists and it is unique:

$$N(t) = N_{eq} \left\{1 - \frac{v_{STAGE}}{L_0}\left[t - \frac{1 - e^{-(k_b P + k_u)t}}{k_b\, P + k_u}\right]\right\} \qquad \text{(Equation 2)}$$

If a constant in defined, $A = v_{STAGE}/[L_0(k_b P + k_u)]$, Equation 2 can be rewritten as:

$$\frac{N}{N_0} = \frac{L}{L_0} + A - A\, e^{\left(\frac{L}{L_0} - 1\right)/A} \qquad \text{(Equation 3)}$$

Equation 3 is the function used to fit the data shown in Figure 4.5 H. Without the inclusion of an offset parameter in the fit, the fit yielded A = 2.1 ± 0.6. Approximating $L_0 \sim 3\ \mu m$, it yields a characteristic exchange time $(k_b P + k_u)^{-1}$ = 130 ± 40 seconds. With the inclusion of an offset parameter, A = 0.87 ± 0.13, yielding $(k_b P + k_u)^{-1}$ = 52 ± 8 seconds.

An important assumption of Equations 2 and 3, and their associated initial value problem (IVP 2) is that there is a zero probability of removing an occupied site, so the equation makes physical sense only when $S_T < N$.

Figure 4.5 GFP-PRC1's evolution in bundles driven to slide at a constant velocity. (A) Schematic of the bundle pulling experiment, highlighting with arrows the motions that drive the two microtubules to slide relative to each other. **(B)** Images of trapped bundle before starting the stage motion, for the X-rhodamine, GFP and transillumination channels, and a composite image. Bar in the bottom is 5 μm. **(C)** Montage of selected frames of a GFP channel time-lapse as the piezoelectric stage moved. Images were collected at 1 frame per second. At the left of the montage the number of the frame for that image is included. Bar in the bottom is 5 μm. **(D)** Images of pulled bundle after stage motion stops, for the X-rhodamine, GFP and transillumination channels, and a composite image. Bar in the bottom is 5 μm. **(E)** A frame-by-frame montage (*left*, bar in bottom is 5 μm), around the time when a sudden change in the bead's position (*center*; in arbitrary units) was observed, and the time to the rupture point of the bundle (*right*), as defined in the main body text. **(F)** Quantification of the GFP signal intensity for all the frames of the time-lapse referred to the time to the rupture point. **(G)** Montage and kymography of a GFP channel time-lapse image with the expected length of bundle superimposed as a red segment, for the montage, and two red lines marking the edges, in the kymograph. Horizontal bars are 5 μm; vertical bar is 10 seconds. **(H)** GFP signal intensity divided initial GFP signal intensity of the event (N/N_0), versus expected bundle length divided initial expected bundle length (L/L_0), for all frames where sliding motion is observed (pooling all successful events), and binning N/N_0 over L/L_0 intervals. The red

curve is a fit is done on $X = L/L_0$, $Y = N/N_0$, to the function: $Y(X) = X + A - A * e^{(X-1)/A} + B$, where A and B were parameters to fit.

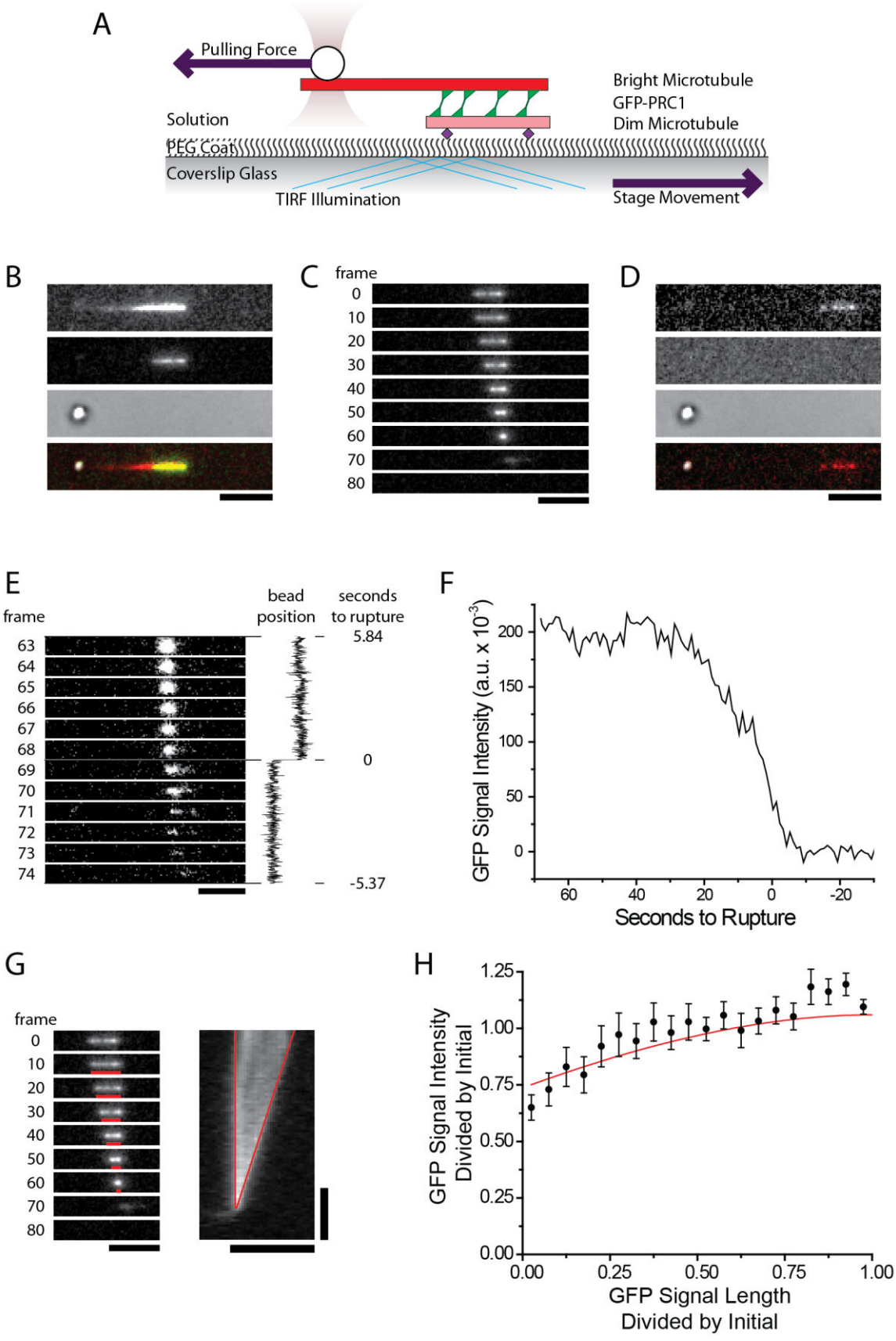
A
Pulling Force
Solution
PEG Coat
Coverslip Glass
TIRF Illumination
Bright Microtubule
GFP-PRC1
Dim Microtubule
Stage Movement
B
C
frame
0
10
20
30
40
50
60
70
80
D
E
frame
bead position
seconds to rupture
63
64
65
66
67
68
69
70
71
72
73
74
5.84
0
-5.37
F
GFP Signal Intensity (a.u. x 10-3)
200
150
100
50
0
60
40
20
0
-20
Seconds to Rupture
G
frame
0
10
20
30
40
50
60
70
80
H
GFP Signal Intensity Divided by Initial
1.25
1.00
0.75
0.50
0.25
0.00
0.00
0.25
0.50
0.75
1.00
GFP Signal Length Divided by Initial

4.6 The frictional force recorded did not scale with the bundle length, but scaled with the GFP-PRC1 signal intensity

The optical tweezers were calibrated to estimate the frictional force arising during the pulling from the bead position recorded by the photodiode quadrant detector. Force was recorded during the period of stage movement, and also ten seconds before and after moving. Figure 4.6 A shows three selected force traces, timed relative to their bundle rupture point. Before stage motion the force remained at a near-constant value. Upon moving the stage at 50 nm/s, the force rose, and in some events it rose at a constant rate (Figure 4.6 A, *bottom*). This initial rise never overlapped with the sliding regime, as defined by the analyses of the GFP signal in the previous section. After a period of sustained friction, the force dropped rapidly on bundle rupture, and following rupture the force remained at a near-constant level. This section after the rupture was used to define the zero force value.

For the sliding regime, the force was averaged during the acquisition of each GFP frame. The averaged force data for each frame were paired with the estimated bundle length and the GFP-PRC1 signal intensity of that frame. All the data from all the sliding regimes of successful pulling events were pooled. Further analyses on the pooled data, from data collected at a stage velocity of 50 nm/s, revealed that the frictional force had a very weak positive correlation with the bundle length (Figure 4.6 B), with ρ_P = 0.29 and ρ_S = 0.22. ρ_P is Pearson's coefficient and ρ_S is Spearman's coefficient; $\rho_P = [S_{XY}/(S_{XX}S_{YY})]^{1/2}$, where $S_{XY} = \sum_{i=1}^{N}[(X_i - \langle X_i \rangle)(Y_i - \langle Y_i \rangle)]$, $S_{XX} = \sum_{i=1}^{N}(X_i - \langle X_i \rangle)^2$, $S_{YY} = \sum_{i=1}^{N}(Y_i - \langle Y_i \rangle)^2$,

and X and Y are paired data vectors (consisting of N data points), with $\langle X_i \rangle$ and $\langle Y_i \rangle$ as mean values, respectively; ρ_S is computed in a similar fashion to ρ_S, but the vectors X and Y are replaced with the ranks of each vector, respectively. Force showed a higher level of positive correlation with the intensity of the GFP-PRC1 signal (Figure 4.6 C), with $\rho_P = 0.89$ and $\rho_S = 0.93$. An unweighted least-squares linear fit ($Y = A + BX$), on the data yielded a slope, $B = 0.12 \pm 0.01$ pN/a.u., and an intercept, $A = 2.1 \pm 0.4$ pN.

Bundle pulling experiments were repeated at a higher pulling speed (200 nm/s). Force traces recorded at a higher speed showed a similar pattern of initial rise as motion started, followed by sustained friction, and a sudden drop in force as the bundle ruptured (Figure 4.6 D). After analyzing the data as done for the slower pulling speed set, the pooled data showed a negative correlation between force and bundle length (Figure 4.6 E), with $\rho_P = -0.88$ and $\rho_S = -0.91$. Force showed a positive correlation with the GFP-PRC1 signal intensity, with $\rho_P = 0.93$ and $\rho_S = 0.95$, and an unweighted linear fit yielded a slope, $B = 0.32 \pm 0.03$ pN/a.u., and an intercept, $A = 4 \pm 1$ pN. For a speed ratio of 4, the ratio of slopes B(200 nm/s)/B(50 nm/s) was 2.7 ± 0.3.

Figure 4.6 The recorded frictional force did not scale with bundle length during driven sliding, but scaled with the number of GFP-PRC1 molecules in the bundle and exhibiting viscosity. (A) Selected traces (gray line) of recorded frictional force while moving stage at 50 nm/s, and also including the 10 second interval before starting motion. Black dots superimposed over the force traces show the averaged values when the time the camera was acquiring a GFP image, during the driven sliding regime. **(B)** Force versus bundle length for all the pooled 50 nm/s data. **(C)** Force versus GFP-PRC1 signal intensity (in arbitrary units) for all the pooled 50 nm/s data. **(D)** Selected traces (gray line) of recorded frictional force while moving stage at 200 nm/s, and also including the 10 second interval before starting motion. Black dots superimposed over the force traces show the averaged values when the time the camera was acquiring a GFP image, during the driven sliding regime. **(E)** Force versus bundle length for all the pooled 200 nm/s data. **(F)** Force versus GFP-PRC1 signal intensity (in arbitrary units) for all the pooled 200 nm/s data. Bars on (B), (C), (E), and (F) are the standard error of the mean value for the bin.

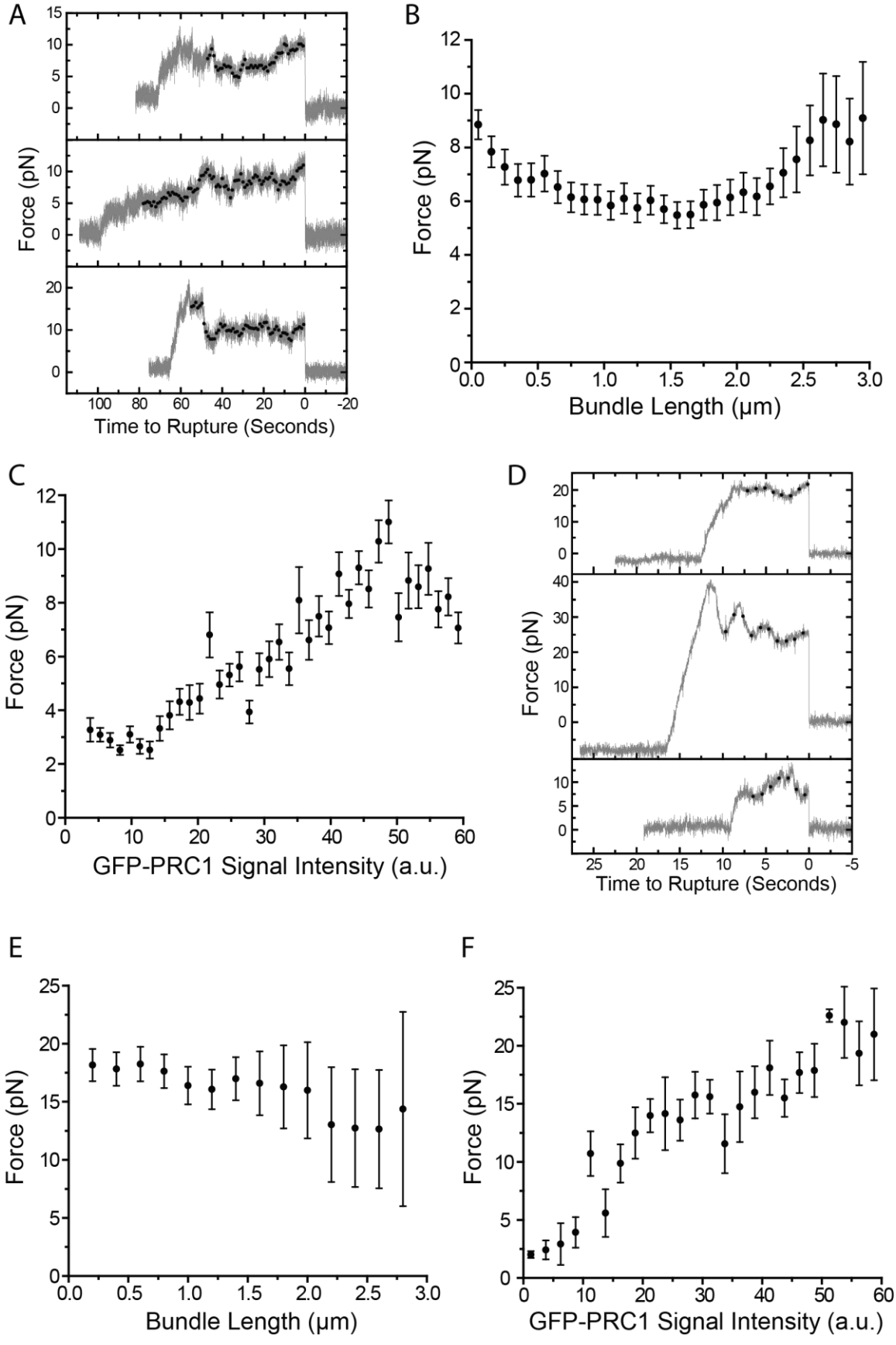
A
Force (pN)
Time to Rupture (Seconds)
B
Force (pN)
Bundle Length (μm)
C
Force (pN)
GFP-PRC1 Signal Intensity (a.u.)
D
Force (pN)
Time to Rupture (Seconds)
E
Force (pN)
Bundle Length (μm)
F
Force (pN)
GFP-PRC1 Signal Intensity (a.u.)

4.7 Stochastic simulations based on a combination of established models reproduce the lack of scaling between force and length observed experimentally

In existing models, the mechanics of microtubules interacting with associated proteins are explained from the diffusive interaction between the protein and the filament (Bormuth et al, 2009; Forth et al, 2014; Lansky et al, 2015). These models consider that proteins are bound to a microtubule, with one protein linked to one site on the microtubule lattice (typically a site is contained to one tubulin heterodimer). Proteins move along the axis of the microtubule, with their motion constrained to a single protofilament, and stepping between adjacent tubulin heterodimer subunits. The stepping behavior follows a Poisson distribution, with the count of steps towards the microtubule plus-end being $Z^{+} \sim \mathrm{Pois}(k^{+}\, t)$ and the count to the minus-end being $Z^{-} \sim \mathrm{Pois}(k^{-}\, t)$, with k^{+} and k^{-} being stepping rates, and t time. For the simulations done, the stepping rates for a given protein were defined as:

$$k_i^{\pm} = k^0\, e^{\frac{\pm F_i\, \Delta x}{k_b\, T}}\, (1-\theta) \qquad \text{(Equation 4)}$$

where the symbol "$\pm$" can either be "$+$" or "$-$", the subindex i specifies which protein's rate is being defined (for N proteins, $i \in [1, N]$), k^0 is the rate under no force and zero occupancy ($k^0 = D/\delta^2$, where D is the diffusivity of the protein bound to the microtubule), and Δx is the spacing between binding sites (typically $\Delta x = 8\ \mathrm{nm}$), F is the force applied on the binding link between the protein and the microtubule's binding site, k_b is Boltzmann constant, T is the temperature, and θ is the occupancy. Force and occupancy are the two variables that determine the

stepping rate's magnitude. The force is specified for a given protein, and it modulates the rate in an Arhenius-like term (as proposed on Bormuth et al, 2009). The occupancy is the same for all proteins bound to a microtubule, and it is defined as $\theta = N\,\Delta x/L$, where N is the number of proteins bound and L is the length interval for which the occupancy is defined (for the analyses done for this section the length interval equaled the bundle length). Its influence on the rate has two trivial extreme effects: under near-zero occupancy the stepping rate remains unaffected, and at full occupancy ($\theta = 1$), no binding sites are available for any stepping to occur, so the rate is zero. The linearity of the occupancy term is reported (Richards, 1977; Suárez et al, 2013), as it is expected out of a hopping motion in discrete sites of an infinite linear chain.

Equation 4 can be used to approximate the dependence of the frictional force measured by an optical trap on the number of GFP-PRC1 proteins and its evolution over time, for a microtubule moving at a constant velocity relative to a surface-bound microtubule, cross-linked by GFP-PRC1. Force applied by the trap (F_{TRAP}), is all transmitted to the surface-bound microtubule through the cross-linking proteins, so $F_{TRAP} = \sum_{i=1}^{N} F_i$. If the force on each cross-linker is approximated to the average of all cross-linkers ($F_i \sim \langle F_i \rangle = \sum_{i=1}^{N} F_i/N$), then the stepping rate can be re-written to:

$$k^{\pm} = k^0\, e^{\frac{\pm F_{TRAP}\,\Delta x}{k_b\,T\,N}}\,(1-\theta) \qquad \text{(Equation 5)}$$

The velocity of a protein relative to a microtubule to which is bound can be defined as $v = (Z^+ - Z^-)\,\Delta x/t$. Given that the counts of steps (Z^+ and Z^-), follow Poisson distributions, $\langle Z^{\pm} \rangle = k^{\pm}\,t$, the average velocity of the protein is $\langle v \rangle =$

$(k^+ - k^-)\,\Delta x$. For a GFP-PRC1 dimer cross-linking two microtubules, it can be assumed that the protein cannot distinguish between the filaments it binds, then on average it will step as many times on one microtubule filament as it will on the other. Then, if the microtubules are driven to move apart at a constant velocity (v_{STAGE}), $\langle v \rangle = v_{STAGE}/2$, and it follows that:

$$v_{STAGE} = 2\,\Delta x\,(k^+ - k^-) \qquad \text{(Equation 6)}$$

Applying the definitions of stepping rates from Equation 5 to Equation 6 yields:

$$v_{STAGE} = 4\,\Delta x\,k^0\,\sinh\left(\frac{F_{TRAP}\,\Delta x}{k_b\,T\,N}\right)(1-\theta) \qquad \text{(Equation 7)}$$

Consider the Taylor series, $\sinh(x) = \sum_{i=0}^{\infty} \frac{x^{2i+1}}{(2i+1)!}$. Keeping only the first term of the series and solving for F_{TRAP} yields:

$$F_{TRAP} = \frac{v_{STAGE}\,k_b\,T}{4\,\Delta x^2\,k^0_{diff}}\,N\,\frac{1}{1-\theta} \qquad \text{(Equation 8)}$$

Consider the infinite geometric series, $\frac{1}{1-\theta} = \sum_{i=0}^{\infty} \theta^i$. Keeping the first two terms and applying the definition of theta ($\theta = N\,\Delta x/L$, and during the sliding regime $L = L_0 - v_{STAGE}\,t$), yields:

$$F_{TRAP}(N(t), t) = \frac{v_{STAGE}\,K_bT}{4\,\Delta x^2\,k^0_{diff}}\,N(t)\left(1 + \frac{N(t)\,\Delta x}{L_0 - v_{STAGE}\,t}\right) \qquad \text{(Equation 9)}$$

Equation 9 has time-dependent variables, and the force measured in the trap can be expressed as a function of the number of proteins and time. Moreover, the number of proteins can be time-dependent, and it can follow the definition of Equation 2. Equation 9 can be segregated into two time dependent terms, $T_1 = N(t)$ and $T_2 = 1 + N(t)\,\Delta x/(L_0 - v_{STAGE}\,t)$, with the rest being constants during the time of sliding ($C = v_{STAGE}\,K_bT/(4\,\Delta x^2\,k^0_{diff})$). Then,

$\dot{F}_{TRAP}/C = \dot{T}_1 T_2 + T_1 \dot{T}_2$ (the accent denotes partial derivative over time). $\dot{T}_2$ is always positive, and tends to zero as the characteristic exchange time, $(k_b P + k_u)^{-1}$, gets smaller. $\dot{T}_1$ is always negative, and increases its modulus as $(k_b P + k_u)^{-1}$ gets smaller. Consequently, a reduction of $(k_b P + k_u)^{-1}$, that is an acceleration of the rates of exchange, would produce a change in the slope of the frictional force towards lower (or more negative) values.

A more detailed analysis of the dependence of the time series of the force measured by the trap on the characteristic exchange time was done using stochastic simulations. In the simulation, two infinite lines were defined having binding sites every 8 nm. One line remained static and the other was allowed to move all its sites simultaneously on the direction of the line. One position on the moving line was defined as the bead position. So, the moving line as it was defined represented the bright microtubule, presented on Figure 4.5 A as the top microtubule of the bundle, and the static line, the dim microtubule, the one in the bottom on Figure 4.5 A. The position of the trap's beam focal point was initially set to be the same as the position of the bead. Particularly, the initial position for both the bead and the beam was set to zero. During the simulations, this position was moved at a constant velocity (v_{STAGE}). A given number of cross-linkers were defined, for which there were two positions, one for one protein binding region ('head') on the top microtubule and another for the protein head on the bottom microtubule. The positions of the protein heads on each microtubule were restricted to the positions of the binding sites of the microtubules.

These definitions allowed the calculation of the distances (Figure 4.7 A): $\Delta XXL(i) = TOPXL(i) - BOTTOMXL(i)$ being the inter-head distance for the cross-linker i, where $TOPXL(i)$ is the position of the top head and $BOTTOMXL(i)$ is the position of the bottom head, and $\Delta XTRAP = BEAD - SS * \Delta T * VSTAGE$ being the distance between the bead and trap's beam focal point, defined as the product of the simulation step (SS), the time interval between steps (ΔT), and the stage velocity ($VSTAGE = v_{STAGE}$). The two distances were used to calculate forces: $FTOP(i) = XLSTIFNESS * \Delta XXL(i)$, where $FTOP(i)$ is force experienced by the top head of the cross-linker i and $XLSTIFNESS$ is the cross-linker stiffness (set to 0.1 pN/nm), $FBOTTOM(i) = -XLSTIFNESS * \Delta XXL(i)$, where $FBOTTOM(i)$is the force experienced by the bottom head of the cross-linker i, and $FTRAP = TRAPSTIFNESS * \Delta XTRAP$, where $FTRAP$ is the trap force exerted on the top microtubule and $TRAPSTIFNESS$ is the trap stiffness (set to 0.1 pN/nm). Equation 4 was used to calculate stepping rates of all heads bound to microtubules, and the stepping rates were used to calculate the stepping probabilities of a given head. For example, Figure 4.7 B shows two stepping probabilities for one of the heads of a given cross-linker: $PPLUS = KPLUS * \Delta T$ and $PMINUS = KMINUS * \Delta T$, where $KPLUS$ and $KMINUS$ are k_i^+ and k_i^- from Equation 4, and i is the given cross-linker.

$KPLUS$ and $KMINUS$ were calculated following the equations:

$$KPLUS = KZERO * e^{FTOP*\Delta X/KBT} * (1 - THETA) \quad \text{(Equation 10)}$$

$$KMINUS = KZERO * e^{-FTOP*\Delta X/KBT} * (1 - THETA) \quad \text{(Equation 11)}$$

Equations 10 and 11 are defined for a given cross-linker and for a protein head bound to a top microtubule. For a bottom head, the equations include $\mathrm{FBOTTOM}$ instead of FTOP. In the calculations, KZERO was set to 60 Hz, $\Delta\mathrm{X}$ was 8 nm, KBT was 4.1 pN*nm and $\mathrm{THETA} = \Delta\mathrm{X} * \mathrm{N}/(\mathrm{LENGHTZERO} - \mathrm{BEAD})$. N was calculated from Equation 2, rounding to the closer integer; the starting value of N was set to 30. For the simulations, $\mathrm{LENGHTZERO}$ was set to 3 μm.

The simulation was run in steps where time ($\mathrm{SS} * \Delta\mathrm{T}$) was increased by $\Delta\mathrm{T}$ on every step ($\Delta\mathrm{T}$ was set to 0.5 ms). On every step N , $\mathrm{LENGTH} = \mathrm{LENGHTZERO} - \mathrm{BEAD}$, and FTRAP were recorded, and the following sequence of instructions was run:

(1) N was calculated using Equation 2, for a KEXCH value set before starting the simulation such that $\mathrm{k_b P} + \mathrm{k_u} = \mathrm{KEXCH}$.

(2) FTOP was calculated for each of the N cross-linkers.

(3) PPLUS and PMINUS were calculated for the TOP heads of the N cross-linkers. Then, each PPLUS and PMINUS were compared to a random number Q, chosen from the interval $[0, 1)$. If $\mathrm{PPLUS} > \mathrm{Q}$, the top head of the cross-linker changed its position **adding** $\Delta\mathbf{X}$. If $\mathrm{PMINUS} < 1 - \mathrm{Q}$, then the position changed **subtracting** $\Delta\mathbf{X}$. Which inequality was checked first was picked at random every time, and if the first check was successful, the second one was not done.

(4) After checking for stepping of the TOP heads, a displacement (BD) was chosen such that adding BD to all $\mathrm{TOPXL(i)}$ and to BEAD would satisfy the equality: $\sum_{\mathrm{i}=1}^{\mathrm{N}} \mathrm{FTOP(i)} = \mathrm{FTRAP}$.

(5) PPLUS and PMINUS were calculated for the BOTTOM heads of the N cross-linkers. Then, when comparing to a random number (Q), if $\mathrm{PPLUS} > \mathrm{Q}$, the bottom head of the cross-linker changed its position **adding** $\Delta\mathbf{X}$, and if $\mathrm{PMINUS} < 1 - \mathrm{Q}$, then the position changed **subtracting** $\Delta\mathbf{X}$.

(6) A new displacement, BD, was calculated and added to all $\mathrm{TOPXL(i)}$ and to BEAD to satisfy the equality: $\sum_{\mathrm{i}=1}^{\mathrm{N}} \mathrm{FTOP(i)} = \mathrm{FTRAP}$.

(7) N, LENGTH, and FTRAP were saved.

The time series of protein count (N), bundle length (LENGTH), and force (FTRAP) were analyzed following the same procedure as the one applied on the experimental data presented on sections 4.5 and 4.6. Simulation data were produced for five characteristic exchange times $(1/\mathrm{KEXCH})$ values (in seconds): 1000, 150, 50, 10, and 1. 10 bundles were simulated per characteristic time. Figure 4.7 C shows the GFP signal intensity divided by initial versus the GFP signal length divided by initial, where the data produced at different characteristic exchange times followed distinct trends. A very slow exchange (very large $1/\mathrm{KEXCH}$), resulted in almost total conservation of the original GFP signal intensity, whereas a very fast exchange (small $1/\mathrm{KEXCH}$), resulted in almost prefect correlation between length and intensity of the GFP signal, suggesting that the bundles quickly adjust their cross-linker count by exchanging proteins with the solution. The data simulated at $1/\mathrm{KEXCH}$ values close to the ones estimated from the analyses of experimental data [with the estimations from section 4.6 being $(\mathrm{k_b P} + \mathrm{k_u})^{-1}$ = 130 ± 40 seconds and $(\mathrm{k_b P} + \mathrm{k_u})^{-1}$ = 52 ± 8

seconds] produced traces positioned in the graph between the extreme cases, with qualitatively similar trends to that of the experimental data from Figure 4.5 H.

Figure 4.7 D shows traces of force versus length for the characteristic times simulated. The two extreme cases show opposite correlations with length, with a negative correlation for a slow exchange and a positive correlation for a fast exchange. Intermediary values of $1/\mathrm{KEXCH}$ produced traces where no evident scaling or correlation between force and length (specifically for $1/\mathrm{KEXCH} = 50$ seconds). Fitting a line, using an unweighted least-squares approach, to the scatter plots of Figure 4.7 D yielded slopes (B for $\mathrm{Y} = \mathrm{A} + \mathrm{B}\,\mathrm{X}$) that decreased in value as the exchange was slower (Figure 4.7 E). A value close to zero was observed for a characteristic exchange time of 50 seconds. A regression done on the trace shown on Figure 4.6 B yielded a slope of 0.4 ± 0.2 pN/μm.

Figure 4.7 Stochastic simulations of bundles during driven sliding. (A) Schematic of bundle of two microtubules represented as dented stripes, with the dents representing binding sites. One microtubule, the top one, is bound to a bead and it is allowed to move along its main axis. The bottom microtubule is stuck in its position. Cross-linking proteins (XL) bind their heads to one and another microtubule. Parameters mentioned in the main text are included in the schematic. **(B)** Detail of a cross-linker bound between two microtubules. Parameters mentioned in the text are included. **(C)** GFP Signal Intensity Divided by Initial versus GFP Signal Length Divided by Initial for simulated data produced from five values of characteristic exchange times $(1/\mathrm{KEXCH} = \{1, 10, 50, 150, 1000\})$, which are labeled on the left side of the panel. **(D)** Force versus Length for simulated data, from five $1/\mathrm{KEXCH}$. **(E)** Slopes from least-squares linear fits done on each data set from panel D.

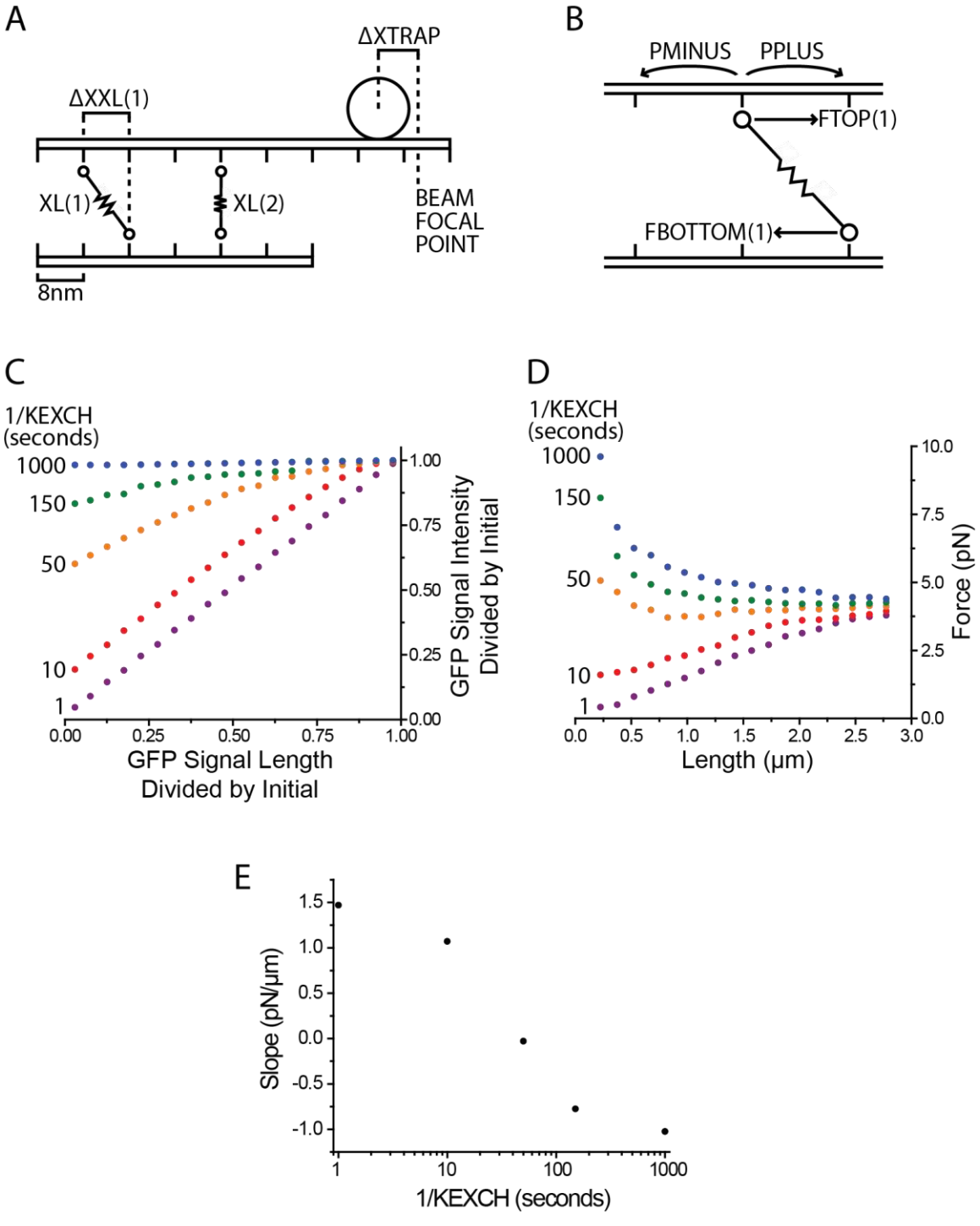
A
ΔXTRAP
ΔXXL(1)
XL(1)
XL(2)
BEAM
FOCAL
POINT
8nm
B
PMINUS
PPLUS
FTOP(1)
FBOTTOM(1)
C
1/KEXCH
(seconds)
1000
150
50
10
1
0.00
0.25
0.50
0.75
1.00
GFP Signal Length
Divided by Initial
GFP Signal Intensity
Divided by Initial
D
1/KEXCH
(seconds)
Force (pN)
Length (μm)
E
Slope (pN/μm)
1/KEXCH (seconds)

4.8 Raising salt and GFP-PRC1 concentrations leads to a shorter characteristic exchange time and a lower frictional force slope during driven sliding

From Equation 9 and from the results of the simulations it is expected that a change in the characteristic exchange time of GFP-PRC1 bound to microtubule bundles would affect the frictional force trace during driven sliding of a bundle. Particularly, the expectation is that reduction of the exchange time would make the slope of the force tend towards negative values. To reduce the exchange time, $(k_b P + k_u)^{-1}$, experimental conditions were modified, looking to increase both terms of the sum, $k_b P$ and k_u. GFP-PRC1's binding lifetime is reduced with increasing salt concentration (Subramanian et al, 2010), and increasing protein concentration, P, increases the rate of binding events. Therefore, both salt and GFP-PRC1 concentrations were increased, which also sought to keep GFP-PRC1 bundle density at a similar level to that of the lower salt and protein concentration condition.

Microtubule bundle assembly was done as in experiments from prior sections, but following the incubation of the microscope chamber with bright microtubules, the solution was exchanged to a solution of higher salt and GFP-PRC1 concentration. After initial testing a condition, hereafter referred as High Salt, was chosen, having 100 mM added KCl (on top of the buffer BRB80), and 0.5 nM GFP-PRC1. All prior data presented was collected with 80 mM added KCl and 0.05 nM GFP-PRC1 (hereafter this condition is referred as Low Salt). Bundles in High Salt were visually similar to those in Low Salt concentrations

(Figure 4.8 A). GFP signal significant in regions where a bright microtubule overlapped with a dim microtubule. Trapped beads were capable of binding the bright microtubule of the bundle and sustaining the bond for an extended time.

Bundles were manipulated to invert their orientation and then restore their original orientation. Similar to bundles in Low Salt, bundles with inverted orientation in High Salt did not show a significant recovery of GFP signal over a period of 10 minutes (data not shown). After returning the manipulated bundles to their original orientation, there was a recovery of the GFP signal on the bundle that was recorded for 10 minutes, but it seemed to plateau after ~2 minutes. Figure 4.8 B shows a montage of a selected bundle after restoring its orientation. The quantification of the GFP signal density divided by the initial (before manipulation), was done for 9 bundles (Figure 4.8 C). Data were fit to a mono-exponential function ($\mathrm{Y(t) = A - Be^{-t/C}}$), yielding a characteristic exchange time of 72 ± 4 seconds, a lower value compared to the characteristic exchange time in Low Salt (240 ± 10 seconds).

Frictional force and GFP signal evolution were measured in High Salt in a manner similar to that of the Low Salt condition, driving the microtubules to slide relative to each other at 50 nm/s. Bundles that could be pulled successfully showed a steady decrease in the GFP signal length, until bundle rupture (Figure 4.8 D and E). Data from 16 bundles were analyzed as it was done for Low Salt data, pooling all data points from the sliding regime of the events analyzed. The GFP signal intensity data was binned and plotted against the bundle length (Figure 4.8 F; Low Salt data included for comparison). Least-squares linear fit

were done on the two data sets plotted, yielding a slope of 28 ± 3 pN/μm for High Salt data (intercept 27 ± 3 pN), and a slope of 14 ± 2 pN/μm for Low Salt (intercept 36 ± 1 pN). The binned force data was plotted against the bundle length (Figure 4.8 G). A linear fit on the data yielded a slope of 3.3 ± 0.3 pN/μm (intercept 6.7 ± 0.3 pN). Fit on the low salt data yielded −1.2 ± 0.2 pN/μm (intercept 7.5 ± 0.2 pN), for the data range 0-2 μm. For the data range 0-3 μm (presented in Figure 4.6 B), the slope was 0.4 ± 0.2 pN/μm (intercept 6.3.5 ± 0.4 pN). Given that $\mathrm{L} = \mathrm{L}_0 - \mathrm{v}_{\mathrm{STAGE}}\mathrm{t}$, an increase in the slope in Figure 4.8 F from Low Salt to High Salt implies that the slope of $\mathrm{N}(\mathrm{t})$, with N being the GFP signal intensity and t time, decreased with increasing salt and GFP-PRC1 concentrations. Equally, the increase in the slope of force versus length implies that the slope of $\mathrm{F}(\mathrm{t})$ decreased, given the same change in conditions.

Figure 4.8 Raising salt and GFP-PRC1 concentrations lead to a faster recovery on re-assembly, a lower GFP signal accumulation and a lower frictional force slope during driven sliding. (A) Images and composite of a bundle in High Salt before manipulating. (From *top* to *bottom*: X-rhodamine channel, GFP channel, transillumination channel, and composite). **(B)** Montage of the composite image of the bundle shown in the previous panel, after stripping and re-assembling. The times marked on the left are after starting the acquisition of the time lapse. **(C)** Quantification of GFP-PRC1 density for 9 averaged bundles, dividing the density values of ach bundle by the initial density recorded before manipulation. The red line is a fit to the function $\mathrm{Y(t)} = \mathrm{A} - \mathrm{Be}^{-\mathrm{t/C}}$. **(D)** Images and composite of a bundle in High Salt before pulling it at 50 nm/seconds. (From *top* to *bottom*: X-rhodamine, GFP, transillumination, and composite). **(E)** Montage of the GFP channel while moving the stage (the stage moves to the left). Frame acquisition began just before starting stage motion, and on the left of the panel the frame number is marked. **(F)** GFP signal intensity (in arbitrary units) versus bundle length for all the pooled High Salt data (in red), and its comparison to Low Salt data (in black). **(G)** Force versus bundle length for all the pooled High Salt data (in red). Data in black corresponds to Low Salt, adapted from Figure 4.6 B to a smaller data range. Horizontal bars in (A), (B), (D), and (E) are 5 μm.

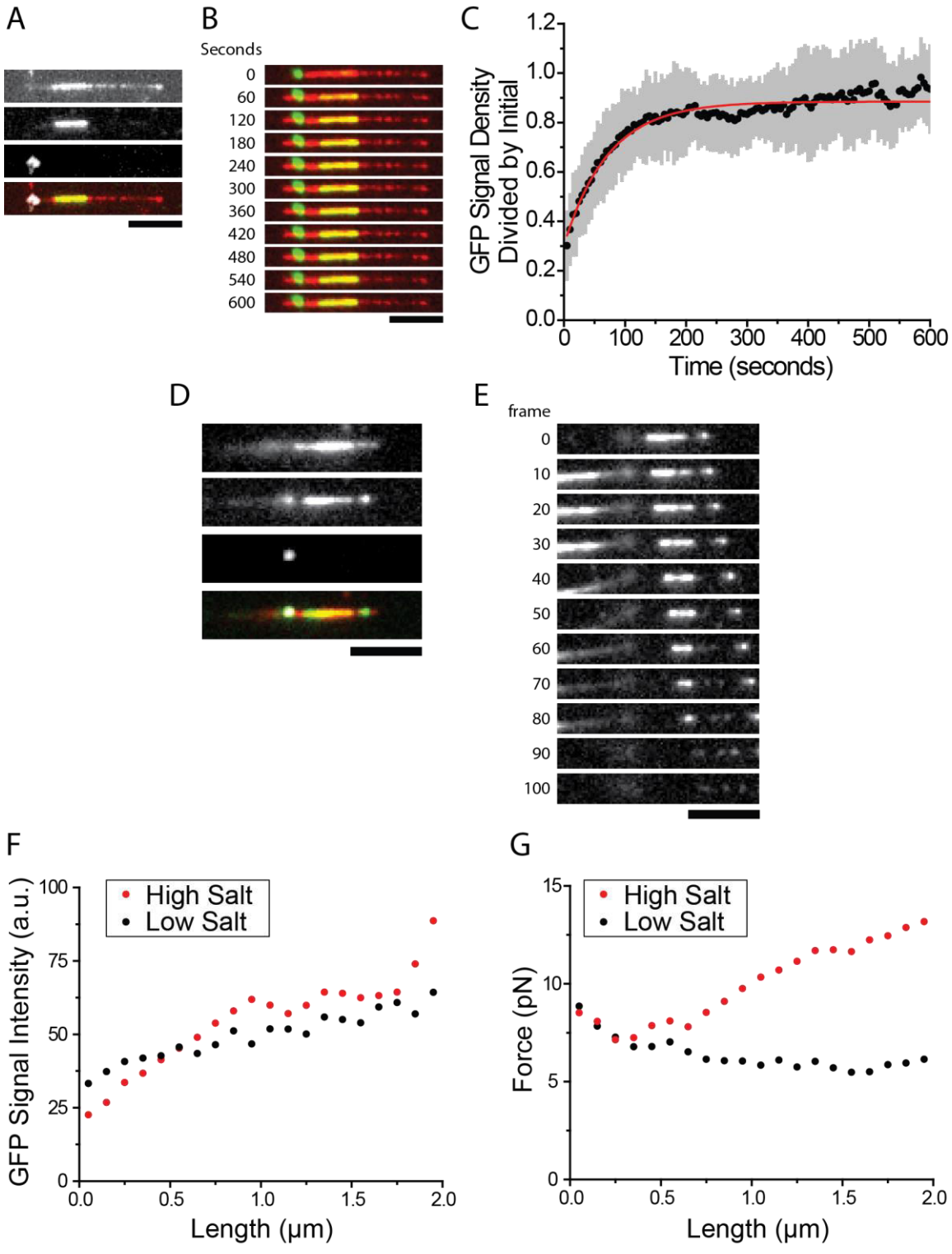
A
B
Seconds
0
60
120
180
240
300
360
420
480
540
600
C
GFP Signal Density Divided by Initial
1.2
1.0
0.8
0.6
0.4
0.2
0.0
0
100
200
300
400
500
600
Time (seconds)
D
E
frame
0
10
20
30
40
50
60
70
80
90
100
F
GFP Signal Intensity (a.u.)
100
75
50
25
0
High Salt
Low Salt
0.0
0.5
1.0
1.5
2.0
Length (μm)
G
Force (pN)
15
10
5
0
High Salt
Low Salt
0.0
0.5
1.0
1.5
2.0
Length (μm)

4.9 Conclusion

This chapter presents a study of the mechanics of PRC1 cross-linking two microtubules, focusing primarily on the relative sliding of filaments at constant velocity. From frictional force measurements and TIRF imaging data a theoretical model was proposed, constructed from the combination of two existing mechanical descriptions that alone are insufficient to explain the experimental data. The model was further tested by changing experimental conditions (salt and GFP-PRC1 concentrations), observing changes on the recovery on re-assembly, and GFP-PRC1 signal and frictional force during driven sliding. The changes observed were consistent with the expectations of the model. Consequently, the work here presented establishes a framework to produce hypotheses linking the cross-linker binding dynamics and mechanics of microtubule networks.

Two microtubule bundles could be assembled having GFP-PRC1 decorating the overlap region of the two filaments almost exclusively. Of 19 bundles (combining the two conditions with varying concentrations), all bundles showed a clear preference for enriching signal on the original orientation they were found, but not on the opposite. This suggests that PRC1 assembles bundles on a specific orientation with very high selectivity. A simple binding model could explain the kinetics of recovery observed, and it could be adapted for the analysis of the GFP signal evolution during driven sliding. The expected characteristic time determined from the recovery kinetics (280 seconds) was larger than that determined from the sliding data (50-130 seconds). It is possible

that during the pulling the exertion of forces on the microtubules reduced the interaction time of the protein, by forcing or promoting the detachment of the protein.

The frictional force recorded with an optical trap setup remained near-constant when the bundles were sliding at constant velocity. Force showed scaling with GFP-PRC1 signal intensity, and it had viscous behavior. A model that was able to reproduce those results incorporated friction emerging from diffusion of a randomly stepping protein (which brings scaling of force with protein number and velocity), and occupancy effects (which increased force as protein accumulation increased). Moreover, this hybrid model hypothesizes that the mechanical response of the bundles can be affected by the exchange kinetics of the cross-linking protein. And the experiments done changing the experimental conditions were in qualitative agreement with the expectation of the model: a shorter characteristic exchange time on recovery was correlated with a more pronounced loss of GFP signal during the pulling and a lower slope of the frictional force recorded.

5. Future directions

5.1 Expanding the reconstitution to a functional augmin complex

The data from Chapter 3 on the augmin holo-complex and sub-complexes established a basis to understand their interaction with microtubules. Co-sedimentation assays suggested similar microtubule affinities for the complexes assayed. The similarity on the affinities from co-sedimentation was also reflected on the observation that the majority of binding events seen at the single molecule level had lifetimes on the order of sub-seconds (0.5-0.8 seconds). The Hice1•GFP-hDgt6-NTD dimer had the distinction of lacking a heavier tail on the distribution of interaction times present on the holo-complex and other sub-complex assayed. Additionally, an octameric construct lacking the microtubule binding region of Hice1 showed a qualitatively large difference in decoration of microtubules with respect to a octameric construct with full-length Hice1. All these data suggest that augmin interacts with microtubules through Hice1 only, with no strong contribution of other subunits.

While the interaction of augmin with microtubules is better understood based on the studies done, the complexes purified lack the capability of nucleating microtubules in a reconstitution assay in vitro. To be able to nucleate de novo microtubules, augmin would have to interact with the gamma-tubulin ring complex (γ-TuRC). Therefore, the full characterization of the microtubule binding properties of a functional augmin complex would require incorporating γ-TuRC into the assays. Fortunately, a recently published work (Song et al, 2018), describes a method to purify γ-TuRC and assay its microtubule binding properties in vitro. The authors of the paper show that γ-TuRC can be recruited

to the entire extension of the lattice of microtubules decorated with the augmin holo-complex. However, no assays on the affinity of the augmin-γ-TuRC grand-complex for microtubules were done, or any measurements on interaction times or diffusivity.

By adapting the single molecule assays to include γ-TuRC, it would be possible to determine if the grand-complex establishes a diffusive interaction with microtubules, with a fast exchange of the grand-complex between the microtubule lattice and the solution, as it was observed for the holo-complex. This assay would further our insights on the function of augmin and establish a solid understanding on how it interacts with microtubules.

5.2 Understanding the distribution of interaction times

All the complexes assayed, but the dimeric construct Hice1•GFP-hDgt6-NTD, had a heavy tail in the distribution of interaction times that cannot be explained by a model where only Hice1 interacts with the microtubule lattice in a simple two-state model (bound↔unbound). A simple two-state interaction would have a transition from bound to unbound following a first order reaction yielding a mono-exponential lifetime of the bound state. Since the data could be fit to a bi-exponential decay, a possible explanation of the data is that the samples were not homogeneous (they had at least two populations of protein complexes). Alternatively, the population could be homogeneous but having an interaction with microtubules that is more complex than a simple bound↔unbound two-state model.

To test the possibility of a heterogeneous population, it would be necessary to use a technique that could segregate populations based on their interaction times. Microtubule affinity chromatography has been used for the identification of associated proteins (Miller et al, 1991). Assuming that the retention time in the column scales with the lifetime of interaction of the associated proteins, it would be possible to resolve samples having proteins with different lifetimes. The elution would be done with a gradient of rising salt concentration that would be collected in aliquots, and the aliquots containing the complex (determined by SDS-PAGE), would be assayed in single molecule fluorescence microscopy. If the population is heterogeneous and the chromatography can resolve the population, each aliquot should have the majority of interaction events with a clear mono-dispersed mono-exponential distribution of interaction times.

If the population does not show evidence of heterogeneity, a more detailed data acquisition would shed light on the nature of the interaction. Data quality can be increased by raising the event count to 10^4-10^5, using fully automated spot-detection and track-assembly software. Additionally, the range of event lifetimes recorded can be extended. Faster frame rate of acquisition can be achieved with a reduction of spatial resolution and using CMOS-SPAD cameras, with a potential acquisition time of μs (Rocca et al, 2016). Data from longer acquisitions could be stitched together to extend the maximum interaction time assayed to the hundreds of seconds.

A more detailed dataset would allow the selection of the best fitting models. While a bi-exponential model fits the data collected adequately, there is an example of a microtubule associated protein with a power-law-like distribution ($Y(t) = At^{-B}e^{-Ct}$, where A, B, and C are constants; Roostalu et al, 2011). There are a wide variety of mechanisms that yield power-law and log-normal distributions (Mitzenmacher, 2003). Particularly, two-state models wth more complex dynamics on each state can yield power-law distributions, with heavy tails like seen for the augmin data (Verberk et al, 2002; Needleman et al, 2009).

5.3 Contribution of other variables on bundle mechanics

The model derived from the data presented on Chapter 4 proposed that the frictional force emerging from sustaining relative sliding of the filaments in a microtubule bundle cross-linked by PRC1 scaled with the number and the density of PRC1 proteins bound to the microtubule. Moreover, the time evolution of the force trace was related to the exchange kinetics of the bundle. There were still a number of issues not addressed, which could be resolved with further data collection, and could help determine sources of variability in the data already collected. First, two velocities were studied for which a viscous behavior was observed. To determine the details of the viscous behavior of sliding bundles it would be necessary to collect more data with velocities up to 1 micron per second, which is the maximum speed observed for cytoplasmic dynein. Second, the model could incorporate a force modulation of the characteristic exchange time, which could be particularly useful for the interpretation of data collected at

multiple velocities. The model could also incorporate a complex binding model for PRC1, as PRC1 also displays an interaction time distribution that is more complex than a mono-exponential (Bieling et al, 2010). Third, the contribution of polarity of the bundle could be determined by labeling the polarity of the surface bound microtubule. Given that the majority of the microtubules manipulated showed evidence of being in an antiparallel configuration, the determination of the polarity of one microtubule of the bundle would inform on the polarity of the other microtubule. Fourth, by changing the polymerization conditions, microtubules of different protofilament number could be polymerized, and then bundles could be assembled pairing combinations to determine if the protofilament number of a bundle has an influence on its mechanics.

5.4 Inclusion of additional components towards the reconstitution of the spindle midzone

During anaphase the spindle midzone coordinates processes of the dividing cells, such as the placement of the cleavage furrow. Full functionality of the midzone requires the recruitment of multiple proteins, with PRC1 being one of them. Another protein recruited to the midzone is the kinesin-4 Kif4a, which interacts with PRC1 (Bieling et al, 2010a; Subramanian et al, 2013). While Kif4a is reported to stop the growth of microtubules when recruited by PRC1 to microtubule bundles, the mechanical contribution of Kif4a to the bundles is not known. Another component of the midzone is centralspindlin, which is a 2:2 heterotetramer of MKLP1, a kinesin-6 and CYN4, a GTPase-activating protein,

also reported to interact with PRC1 (Lee et al, 2015). Moreover, the kinase Plk1 also gets recruited to the midzone during anaphase, and was reported to regulate PRC1's function via phosphorylation of threonine 602 (Hu et al, 2012). The inclusion of these proteins on the assays done on bundle mechanics would allow dissecting their contribution.

5.5 Establishing the properties of PRC1 that determine bundle mechanics

While Chapter 4 of this Thesis presented a description of the mechanics of PRC1 cross-linking microtubule bundles, these were not linked to the properties of PRC1. Given that the structure of the homo-dimer is known (except for the C-terminal region; Subramanian et al, 2013), and also the microtubule binding regions and post-translational modification sites have been characterized (Subramanian et al, 2010), the analysis of the bundle mechanics of mutants of PRC1 would allow establishing which the properties of PRC1 contribute to the mechanics.

Alanine-mutants of basic amino acids on the spectrin domain of PRC1 have a lower affinity (Subramanian et al, 2010). The four residues mutated (R377A, K387A, K390A, and R450A), led to up to a four-fold decrease in affinity relative to wild type PRC1. The impact of the mutations is expected to mimic the effect of increasing the salt concentration in the solution, as it was presented on section 4.8. Therefore, bundles assembled with PRC1 mutants are expected to have a shorter characteristic exchange time and a frictional force time-series with

a slope tending towards negative values. Another set of mutations to test would involve disruptions of the coiled structure of the homodimer, by including insertions of glycine-serine repeats. These repeats are expected to modify the microtubule binding properties of PRC1 in non-trivial ways, such that the analysis of the mechanics of bundles with these mutants could shed light on the contribution of PRC1's structural rigidity to the mechanics. Finally, mutants mimicking phosphorylations (such as that on threonine 602 by Plk1), or with an alanine mutation in combination with active Plk1 could contribute to any studies on Plk1's contribution to PRC1's cross-linking mechanics.

5.6 Model expectations on dividing cells

The characterization of PRC1 mutants in vitro would allow correlating observations on cell-based experiments with the results of in vitro experiments. PRC1 knockdowns would be combined with transient transfections of mutant constructs to assess rescue during cell division. Cells would then be analyzed by immunofluorescence and/or live imaging. The spindle phenotype in anaphase, and the distribution of PRC1 would be the most important variables to consider in order to contrast with the in vitro results. Particularly, in a case where a mutant shows a shorter characteristic exchange time, PRC1's accumulation in the midzone on the onset of anaphase B is expected to be lower relative to wild type. Concurrently, the spindle length change on anaphase B is expected to be larger, suggesting a weaker mechanical link.

References

Arai, T., Ihara, Y., Arai, K., and Kaziro, Y. (1975). Purification of tubulin from bovine brain and its interaction with guanine nucleotides. J Biochem *77*,647-658.

Asbury, C. L. (2017). Anaphase A: Disassembling Microtubules Move Chromosomes toward Spindle Poles. Biology *6*, 15.

Asbury, C. L., Tien, J. F., and Davis, T. N. (2011). Kinetochores' gripping feat: Conformational wave or biased diffusion? Trends Cell Biol *21*, 38-46.

Bieling, P., Telley, I. A., and Surrey, T. (2010a). A minimal midzone protein module controls formation and length of antiparallel microtubule overlaps. Cell *142*, 420-432.

Bieling, P., Telley, I. A., Hentrich, C., Piehler, J., and Surrey, T. (2010b). Fluorescence microscopy assays on chemically functionalized surfaces for quantitative imaging of microtubule, motor, and +TIP dynamics. Methods Cell Biol *95*, 555-580.

Borisy, G. G. and Taylor, E. W. (1967a). The mechanism of action of colchicine. Binding of colchincine-3H to cellular protein. J Cell Biol *34*, 525-533.

Borisy, G. G.,and Taylor, E. W. (1967b). The mechanism of action of colchicine. Colchicine binding to sea urchin eggs and the mitotic apparatus. J Cell Biol *34*, 535-548.

Bormuth, V., Varga, V., Howard, J., and Schäffer, E. (2009). Protein friction limits diffusive and directed movements of kinesin motors on microtubules. Science *325*, 870-873.

Braun, M., Lansky, Z., Fink, G., Ruhnow, F., Diez, S., and Janson, M. E. (2011). Adaptive braking by Ase1 prevents overlapping microtubules from sliding completely apart. Nat Cell Biol *13*, 1259-1264.

Brouhard, G. and Sept, D. (2012). Microtubules: sizing up the GTP cap. Curr Biol *22*, 802-803.

Brouhard, G. J., Stear, J. H., Noetzel, T. L., Al-Bassam, J., Kinoshita, K., Harrison, S. C., Howard, J., and Hyman, A. A. (2008). XMAP215 is a processive microtubule polymerase. Cell *132*, 79-88.

Brust-Mascher, I., Civelekoglu-Scholey, G., Kwon, M., Mogilner, A., and Scholey, J. M. (2004). Model for anaphase B: Role of three mitotic motors in a switch from poleward flux to spindle elongation. Proc Natl Acad Sci *101*, 15938–15943.

Burbank, K. S., Mitchison, T. J., and Fisher, D. S. (2007). Slide-and-cluster models for spindle assembly. Curr Biol *17*, 1373–1383.

Carazo-Salas, R. E., Guarguaglini, G., Gruss, O. J., Segref, A., Karsenti, E., and Mattaj, I. W. (1999). Generation of GTP-bound Ran by RCC1 is required for chromatin-induced mitotic spindle formation. Nature *400*, 178-181.

Cimini, D., Cameron, L. A., and Salmon, E. D. (2004). Anaphase spindle mechanics prevent mis-segregation of merotelically oriented chromosomes. Curr Biol *14*, 2149–2155.

Chaaban, S. and Brouhard, G. J. (2017). A microtubule bestiary: structural diversity in tubulin polymers. Mol Biol Cell *28*, 2924-2931.

Dujardin, D. L. and Vallee, R. B. (2002). Dynein at the cortex. Curr Opin Cell Biol *14*, 44-49.

Dumont, J. and Desai, A. (2012). Acentrosomal spindle assembly and chromosome segregation during oocyte meiosis. Trends Cell Biol *22*, 241–249.

Dumont, S. and Mitchison, T. J. (2009). Force and length in the mitotic spindle. Curr Biol *19*, R749-R761.

Evans, L., Mitchison, T., and Kirschner, M. (1985). Influence of the centrosome on the structure of nucleated microtubules. J Cell Biol *100*, 1185-1191.

Fink, G., Schuchardt, I., Colombelli, J., Stelzer, E., and Steinberg, G. (2006). Dynein-mediated pulling forces drive rapid mitotic spindle elongation in ustilago maydis. EMBO J *25*, 4897–4908.

Fol, H. (1873). Die erste Entwickelung des Geryonideneis. Jenaische Zeitschr f Naturw, 471-492.

Folta-Stogniew, E. and Williams, K. R. (1999). Determination of molecular masses of proteins in solution: Implementation of an HPLC size exclusion chromatography and laser light scattering service in a core laboratory. J Biomol Tech *10*, 51-63.

Forth, S., Hsia, K. C., Shimamoto, Y., and Kapoor, T. M. (2014). Asymmetric friction of nonmotor MAPs can lead to their directional motion in active microtubule networks. Cell *157*, 420-432.

Ganem, N. J., Upton, K., and Compton, D. A. (2005). Efficient mitosis in human cells lacking poleward microtubule flux. Curr Biol *15*, 1827-1832.

Gonzalez, C. (2003). Cell division: the place and time of cytokinesis. Curr Biol *13*, 363-365.

Goodwin, S. S. and Vale, R. D. (2010). Patronin regulates the microtubule network by protecting microtubule minus ends. Cell *143*, 263-274.

Goshima, G., Mayer, M., Zhang, N., Stuurman, N., and Vale, R. D. (2008). Augmin: a protein complex required for centrosome-independent microtubule generation within the spindle. J Cell Biol *181*, 421-429.

Goshima, G.,Wollman, R., Goodwin, S. S., Zhang, N., Scholey, J. M., Vale, R. D., and Stuurman, N. (2007). Genes required for mitotic spindle assembly in Drosophila S2 cells. Science *316*, 417-421.

Gourret, J. P. (1995). Modelling the mitotic apparatus. From the discovery of the bipolar spindle to modern concepts. Acta Biotheor *43*, 127-42.

Grishchuk, E. L., Molodtsov, M. I., Ataullakhanov, F. I., and McIntosh, J. R. (2005). Force production by disassembling microtubules. Nature *438*, 384–388.

Gruss, O. J., Carazo-Salas, R. E., Schatz, C. A., Guarguaglini, G., Kast, J., Wilm, M., Le Bot, N., Vernos, I., Karsenti, E., and Mattaj, I. W. (2001). Ran induces spindle assembly by reversing the inhibitory effect of importin a on TPX2 activity. Cell *104*, 83-93.

Gruss, O. J. and Vernos, I. (2004). The mechanism of spindle assembly: Functions of Ran and its target TPX2. J Cell Biol *166*, 949-955.

Harris, P. (1965). Some observations concerning metakinesis in sea urchin eggs. J Cell Biol *25*, 73-77.

Hayward, D., Metz, J., Pellacani, C., and Wakefield, J. G. (2014). Synergy between multiple microtubule-generating pathways confers robustness to centrosome-driven mitotic spindle formation. Dev Cell *28*, 81–93.

Heald, R., Tournebize, R., Blank, T., Sandaltzopoulos, R., Becker, P., Hyman, A., and Karsenti, E. (1996). Self-organization of microtubules into bipolar spindles around artificial chromosomes in Xenopus egg extracts. Nature *382*, 420-425.

Helenius, J., Brouhard, G., Kalaidzidis, Y., Diez, S., and Howard, J. (2006). The depolymerizing kinesin MCAK uses lattice diffusion to rapidly target microtubule ends. Nature *441*, 115-119.

Hentrich, C. and Surrey, T. (2010). Microtubule organization by the antagonistic mitotic motors kinesin-5 and kinesin-14. J Cell Biol *189*, 465-480.

Honnappa, S., Gouveia, S. M., Weisbrich, A., Damberger, F. F., Bhavesh, N. S., Jawhari, H., Grigoriev, I., van Rijssel, F. J., Buey, R. M., Lawera, A., et al. (2009). An EB1-binding motif acts as a microtubule tip localization signal. Cell *138*, 366-376.

Hu, C.K., Ozlü, N., Coughlin, M., Steen, J. J., and Mitchison, T. J. (2012). Plk1 negatively regulates PRC1 to prevent premature midzone formation before cytokinesis. Mol Biol Cell *23*, 2702-2711.

Hunter, A. W., Caplow, M., Coy, D. L., Hancock, W. O., Diez, S., Wordeman, L., and Howard, J. (2003). The kinesin-related protein MCAK is a microtubule depolymerase that forms an ATP-hydrolyzing complex at microtubule ends. Mol Cell *11*, 445-457.

Hsia, K. C., Wilson-Kubalek, E. M., Dottore, A., Hao, Q., Tsai, K. L., Forth, S., Shimamoto, Y., Milligan, R. A., and Kapoor, T. M. (2014). Reconstitution of the augmin complex provides insights into its architecture and function. Nat Cell Biol *16*, 852-863.

Hyman, A., Drechsel, D., Kellogg, D., Salser, S., Sawin, K., Steffen, P., Wordeman, L., and Mitchison, T. (1991). Preparation of modified tubulins. Methods Enzymol *196*, 478-485.

Hyman, A. A., Salser, S., Drechsel, D. N., Unwin, N., and Mitchison, T. J. (1992). Role of GTP hydrolysis in microtubule dynamics: information from a slowly hydrolyzable analogue, GMPCPP. Mol Biol Cell *3*, 1155-1167.

Janke, C. (2014). The tubulin code: molecular components, readout mechanisms, and functions. J Cell Biol *206*, 461-472.

Kamasaki, T., O'Toole, E., Kita, S., Osumi, M., Usukura, J., McIntosh, J. R., and Goshima G. (2013). Augmin-dependent microtubule nucleation at microtubule walls in the spindle. J Cell Biol *202*, 25-33.

Kapitein, L. C., Kwok, B. H., Weinger, J. S., Schmidt, C. F., Kapoor, T. M., and Peterman, E. J. (2008). Microtubule cross-linking triggers the directional motility of kinesin-5. J Cell Biol *182*, 421-428.

Kapoor, T. M., Mayer, T. U., Coughlin, M. L., and Mitchison, T. J. (2000). Probing spindle assembly mechanisms with monastrol, a small molecule inhibitor of the mitotic kinesin, Eg5. JCell Biol *150*, 975-988.

Karsenti, E. and Vernos, I. (2001). The mitotic spindle: a self-made machine. Science *294*, 543–547.

Kashina, A. S., Baskin, R. J., Cole, D. G., Wedaman, K. P., Saxton, W. M., and Scholey, J. M. (1996). A bipolar kinesin. Nature *379*, 270–272.

Kelly, A. E. and Funabiki, H. (2009). Correcting aberrant kinetochore microtubule attachments: an Aurora B-centric view. Curr Opin Cell Biol *21*, 51–58.

Khodjakov, A., La Terra, S., and Chang, F. (2004). Laser microsurgery in fission yeast; role of the mitotic spindle midzone in anaphase B. Curr Biol *14*, 1330–1340.

Kwok, B. H., Kapitein, L. C., Kim, J. H., Peterman, E. J., Schmidt, C. F., and Kapoor, T. M. (2006). Allosteric inhibition of kinesin-5 modulates its processive directional motility. Nat Chem Biol *2*, 480-485.

LaFountain, J. R., Jr., Oldenbourg, R., Cole, R. W., and Rieder, C. L. (2001). Microtubule flux mediates poleward motion of acentric chromosome fragments during meiosis in insect spermatocytes. Mol Biol Cell *12*, 4054-4065.

Lansky, Z., Braun, M., Lüdecke, A., Schlierf, M., ten Wolde, P. R., Janson, M. E., and Diez, S. (2015). Diffusible crosslinkers generate directed forces in microtubule networks. Cell *160*, 1159-1168.

Lawo, S., Bashkurov, M., Mullin, M., Ferreria, M. G., Kittler, R., Habermann, B., Tagliaferro, A., Poser, I., Hutchins, J. R., Hegemann, B., Pinchev, D., Buchholz, F., Peters, J. M., Hyman, A. A., Gingras, A. C., and Pelletier, L. (2009). HAUS, the 8-subunit human Augmin complex, regulates centrosome and spindle integrity. Curr Biol *19*, 816–826.

Lee, K. Y., Esmaeili, B., Zealley, B., and Mishima, M. (2015). Direct interaction between centralspindlin and PRC1 reinforces mechanical resilience of the central spindle. Nat Commun *6*, 7290.

Liu, J., Wang, Z., Jiang, K., Zhang, L., Zhao, L., Hua, S., Yan, F., Yang, Y., Wang, D., Fu, C., Ding, X., Guo, Z., and Yao, X. (2009). PRC1 cooperates with CLASP1 to organize central spindle plasticity in mitosis. J Biol Chem *284*, 23059-23071.

Lu, H., Ali, M. Y., Bookwalter, C. S., Warshaw, D. M., and Trybus, K. M. (2009). Diffusive movement of processive kinesin-1 on microtubules. Traffic *10*,1429-1438.

Lüders, J. and Stearns, T. (2007). Microtubule-organizing centres: a re-evaluation. Nat Rev Mol Cell Biol *8*, 161–167.

Ludueña, R. F.(2013). A hypothesis on the origin and evolution of tubulin. Int Rev Cell Mol Biol *302*, 41-185.

Maddox, P. S., Bloom, K. S., and Salmon, E. D. (2000). The polarity and dynamics of microtubule assembly in the budding yeast Saccharomyces cerevisiae. Nat Cell Biol *2*, 36-41.

Mandelkow, E. M., Mandelkow, E., and Milligan, R. A. (1991). Microtubule dynamics and microtubule caps: a time-resolved cryo-electron microscopy study. J Cell Biol *114*, 977-991.

Maurer, S. P., Fourniol, F. J., Bohner, G., Moores, C. A., and Surrey, T. (2012). EBs recognize a nucleotide-dependent structural cap at growing microtubule ends. Cell *149*, 371-382.

McIntosh, J. R., Cande, W. Z., and Snyder, J. A. (1975). Structure and physiology of the mammalian mitotic spindle. Soc Gen Physiol *30*, 31-76.

McIntosh, J. R. and Hays, T. (2016). A Brief History of Research on Mitotic Mechanisms. Biology *5*, 55.

McNally, F. J. and Vale, R. D. (1993). Identification of katanin, an ATPase that severs and disassembles stable microtubules. Cell *75*, 419-429.

Miller, M. P., Asbury, C. L., and Biggins, S. (2016). A TOG Protein Confers Tension Sensitivity to Kinetochore-Microtubule Attachments. Cell *165*, 1428-1439.

Miller, K. G., Field, C. M., Alberts, B. M., and Kellogg, D. R. (1991). Use of actin filament and microtubule affinity chromatography to identify proteins that bind to the cytoskeleton. Methods Enzymol *196*, 303-319

Mitzenmacher, M. (2003). A Brief History of Generative Models for Power Law and Lognormal Distributions. Internet Math *1*, 226-251.

Mitchison, T. J. (1993). Localization of an exchangeable GTP binding site at the plus end of microtubules. Science *261*, 1044-1047.

Mitchison, T. and Kirschner, M. (1984). Dynamic instability of microtubule growth. Nature. *312*, 237-242.

Mollinari, C., Kleman, J. P., Jiang, W., Schoehn, G., Hunter, T., and Margolis, R. L. (2002). PRC1 is a microtubule binding and bundling protein essential to maintain the mitotic spindle midzone. J Cell Biol *157*, 1175-1186.

Moritz, M., Braunfeld, M. B., Guénebaut, V., Heuser, J., and Agard, D. A. (2000). Structure of the gamma-tubulin ring complex: a template for microtubule nucleation. Nat Cell Biol *2*, 365-370.

Needleman, D. J., Groen, A., Ohi, R., Maresca, T., Mirny, L., and Mitchison, T. (2009). Fast microtubule dynamics in meiotic spindles measured by single molecule imaging: evidence that the spindle environment does not stabilize microtubules. Mol Biol Cell *21*, 323-333.

Nurse, P. (1990). Universal control mechanism regulating onset of M-phase. Nature *344*, 503-508.

Pfarr, C. M., Coue, M., Grissom, P. M., Hays, T. S., Porter, M. E., and McIntosh, J. R. (1990). Cytoplasmic dynein is localized to kinetochores during mitosis. Nature *345*, 263-265.

Petry, S., Groen, A. C., Ishihara, K., Mitchison, T. J., and Vale, R. D. (2013). Branching microtubule nucleation in Xenopus egg extracts mediated by augmin and TPX2. Cell *152*, 768–777.

Petry, S., Pugieux, C., Nédélec, F. J., and Vale, R. D. (2011). Augmin promotes meiotic spindle formation and bipolarity in Xenopus egg extracts. Proc Natl Acad Sci USA *108*, 14473–14478.

Reber, S. and Hyman, A. A. (2015). Emergent Properties of the Metaphase Spindle. Cold Spring Harb Perspect Biol *7*, a015784.

Rice, S., Lin, A. W., Safer, D., Hart, C. L., Naber, N., Carragher, B. O., Cain, S. M., Pechatnikova, E., Wilson-Kubalek, E. M., Whittaker, M., Pate, E., Cooke, R., Taylor, E. W., Milligan, R. A., and Vale, R. D. (1999). A structural change in the kinesin motor protein that drives motility. Nature *402*, 778-784.

Richards, P. M. (1977). Theory of one-dimensional hopping conductivity and diffusion, Phys Rev B *16*, 1393-1409.

Rocca, F. M., Nedbal, J., Tyndall, D., Krstajić, N., Li, D. D., Ameer-Beg, S. M., and Henderson, R. K. (2016). Real-time fluorescence lifetime actuation for cell sorting using a CMOS SPAD silicon photomultiplier. Opt Lett *41*, 673-676.

Roostalu, J., Hentrich, C., Bieling, P., Telley, I. A., Schiebel, E., and Surrey, T. (2011). Directional switching of the kinesin Cin8 through motor coupling. Science *332*, 94-99.

Sanchez, T., Welch, D., Nicastro, D., and Dogic, Z. (2011). Cilia-like beating of active microtubule bundles. Science *333*, 456-459.

Saxton, W. M., and McIntosh, J. R. (1987). Interzone microtubule behavior in late anaphase and telophase spindles. J Cell Biol *105*, 875–886.

Scholey, J. M., Civelekoglu-Scholey, G., and Brust-Mascher, I. (2016). Anaphase B. Biology *5*, 51.

Seetapun, D., Castle, B. T., McIntyre, A. J., Tran, P. T., and Odde, D. J. (2012). Estimating the microtubule GTP cap size in vivo. Curr Biol *22*, 1681-1687.

Shimamoto, Y., Forth, S., and Kapoor, T. M. (2015). Measuring Pushing and Braking Forces Generated by Ensembles of Kinesin-5 Crosslinking Two Microtubules. Dev Cell 34, 669-681.

Simeonov, D. R., Kenny, K., Seo, L., Moyer, A., Allen, J., and Paluh, J. L. (2009). Distinct Kinesin-14 mitotic mechanisms in spindle bipolarity. Cell Cycle *8*, 3571-3583.

Slautterback, D. B. (1963). Cytoplasmic microtubules. J Cell Biol *18*, 367-388.

Smith, M. B., Karatekin, E., Gohlke, A., Mizuno, H., Watanabe, N., and Vavylonis, D. (2011). Interactive, computer-assisted tracking of speckle trajectories in fluorescence microscopy: application to actin polymerization and membrane fusion. Biophys J *101*, 1794-1804.

Song, J. G., King, M. R., Zhang, R., Kadzik, R. S., Thawani, A., and Petry, S. (2018). Mechanism of how augmin directly targets the gamma-tubulin ring complex to microtubules. J Cell Biol *217*, 2417-2428.

Strasburger, E. (1875). Etudes sur la formation et la division des cellules. Edition revue et corrigé, traduite de l'allemand par J.J. Kicks Paris 1876.

Strasburger, E. (1884). Die Controversen der indirecten Kerntheilung. Archiv für mikroskopische Anatomie *23*, 246-304.

Suárez, G., Hoyuelos, M., and Martin, H. O. (2013). Evolution equation for tagged-particle density and correlations in single-file diffusion. Phys Rev E Stat Nonlin Soft Matter Phys *88*, 022131.

Subramanian, R., Ti, S. C., Tan, L., Darst, S. A., and Kapoor, T. M. (2013). Marking and measuring single microtubules by PRC1 and kinesin-4. Cell *154*, 377-390.

Subramanian, R., Wilson-Kubalek, E. M., Arthur, C. P., Bick, M. J., Campbell, E. A., Darst, S. A., Milligan, R. A., and Kapoor, T. M. (2010). Insights into antiparallel microtubule crosslinking by PRC1, a conserved nonmotor microtubule binding protein. Cell *142*, 433-443.

Sumino, Y., Nagai, K. H., Shitaka, Y., Tanaka, D., Yoshikawa, K., Chaté, H., and Oiwa, K. (2012). Large-scale vortex lattice emerging from collectively moving microtubules. Nature *483*, 448-452.

Tan, S., Kern, R. C., and Selleck, W. (2005). The pST44 polycistronic expression system for producing protein complexes in Escherichia coli. Protein Expr Purif *40*, 385–395.

Tanenbaum, M. E., and Medema, R. H. (2010). Mechanisms of centrosome separation and bipolar spindle assembly. Dev Cell *19*, 797-806.

Trowitzsch, S., Bieniossek, C., Nie, Y., Garzoni, F., and Berger, I. (2010). New baculovirus expression tools for recombinant protein complex production. J Struct Biol *172*, 45–54.

Uehara, R., Nozawa, R. S., Tomioka, A., Petry, S., Vale, R. D., Obuse, C., and Goshima, G. (2009). The augmin complex plays a critical role in spindle microtubule generation for mitotic progression and cytokinesis in human cells. Proc Natl Acad Sci USA *106*, 6998–7003.

Uteng, M., Hentrich, C., Miura, K., Bieling, P., and Surrey, T. (2008). Poleward transport of Eg5 by dynein-dynactin in Xenopus laevis egg extract spindles. J Cell Biol *182*, 715-726.

Valentine, M. T., Fordyce, P. M., Krzysiak, T. C., Gilbert, S. P., and Block, S. M. (2006). Individual dimers of the mitotic kinesin motor Eg5 step processively and support substantial loads in vitro. Nat Cell Biol *8*, 470-476.

Varga, V., Helenius, J., Tanaka, K., Hyman, A. A., Tanaka, T. U., and Howard, J. (2006). Yeast kinesin-8 depolymerizes microtubules in a length-dependent manner. Nat Cell Biol *8*, 957-962.

Verberk, R., Antoine, M. O., and Orrit, M. (2002). Simple model for the power-law blinking of single semiconductor nanocrystals. Phys Rev B *66*, 233202.

Wadsworth, P. and Khodjakov, A. (2004). E pluribus unum: towards a universal mechanism for spindle assembly. Trends Cell Biol *14*, 413–419.

Williams, R. C. Jr. and Lee, J. C. (1982). Preparation of tubulin from brain. Methods Enzymol *85*, B376-385.

Winey, M. and Bloom, K. (2012). Mitotic spindle form and function. Genetics *190*, 1197-1224.

Wu G., Lin Y. T., Wei R., Chen Y., Shan Z., and Lee W. H. (2008). Hice1, a novel microtubule-associated protein required for maintenance of spindle integrity and chromosomal stability in human cells. Mol Cell Biol *28*, 3652–3662.

Yanagida, M. (2014). The role of model organisms in the history of mitosis research. Cold Spring Harb Perspect Biol *6*, a015768.

Zanic, M.,Widlund, P. O.,Hyman, A. A., and Howard, J. (2013). Synergy between XMAP215 and EB1 increases microtubule growth rates to physiological levels. Nat Cell Biol *15*, 688-693.

Zhu, C., Bossy-Wetzel, E., and Jiang, W. (2005). Recruitment of MKLP1 to the spindle midzone/midbody by INCENP is essential for midbody formation and completion of cytokinesis in human cells. Biochem J *389*, 373-381.

Zhu, C., Lau, E., Schwarzenbacher, R., Bossy-Wetzel, E., and Jiang, W. (2006). Spatiotemporal control of spindle midzone formation by PRC1 in human cells. Proc Natl Acad Sci *103*, 6196-6201.